

UNIVERSITY OF SÃO PAULO  
GEOSCIENCES INSTITUTE

**Geometry and stratigraphy of the Limeira Tholeiitic intrusion, Paraná  
Magmatic Province (SP-Brazil)**

**LUCAS MARTINS LINO AGUIAR DOS SANTOS**

Master Dissertation submitted to the Geosciences  
Institute of the University of São Paulo to obtain a Master  
of Science degree.

Concentration Area: Mineralogy and Petrography

Advisor: Prof. Dr. Silvio Roberto Farias Vlach

SÃO PAULO

2018

Autorizo a reprodução e divulgação total ou parcial deste trabalho, por qualquer meio convencional ou eletrônico, para fins de estudo e pesquisa, desde que citada a fonte.

Serviço de Biblioteca e Documentação do IGc/USP

Ficha catalográfica gerada automaticamente com dados fornecidos pelo(a) autor(a)  
via programa desenvolvido pela Seção Técnica de Informática do ICMC/USP

Bibliotecários responsáveis pela estrutura de catalogação da publicação:  
Sonia Regina Yole Guerra - CRB-8/4208 | Anderson de Santana - CRB-8/6658

Martins Lino Aguiar dos Santos, Lucas  
Geometry and stratigraphy of the Limeira  
tholeiitic intrusion, Paraná Magmatic Province (SP-  
Brasil) / Lucas Martins Lino Aguiar dos Santos;  
orientador Silvio Roberto Farias Vlach. -- São  
Paulo, 2018.  
77 p.

Dissertação (Mestrado - Programa de Pós-Graduação  
em Mineralogia e Petrologia) -- Instituto de  
Geociências, Universidade de São Paulo, 2018.

1. Limeira Intrusion. 2. 2D magnetometric  
modeling. 3. Crystal Size Distribution (CSD). 4.  
Emplacement Model. 5. Paraná Magmatic Province. I.  
Roberto Farias Vlach, Silvio , orient. II. Título.

UNIVERSIDADE DE SÃO PAULO  
INSTITUTO DE GEOCIÊNCIAS

**GEOMETRY AND STRATIGRAPHY OF THE LIMEIRA THOLEIITIC  
INTRUSION, PARANÁ MAGMATIC PROVINCE (SP-BRAZIL)**

**LUCAS MARTINS LINO AGUIAR DOS SANTOS**

Orientador: Prof. Dr. Silvio Roberto Farias Vlach

Dissertação de Mestrado

**Nº 813**

COMISSÃO JULGADORA

Dr. Silvio Roberto Farias Vlach

Dr<sup>a</sup>. Liza Angélica Polo

Dr. Antônio José Ranalli Nardy

SÃO PAULO  
2018

## ACKNOWLEDGMENTS

“If I have seen further it is by standing  
on the shoulders of Giants.” Sir Isaac Newton

I would like to thank those who participated or contributed, directly or indirectly, with this research.

I am indebted to my advisor, Prof. Dr. Silvio RF Vlach (Silvião), for guiding me in the last five years over the universe of igneous rocks and their processes. Thank you very much for your uncommon patience, the enormous encouragement, scientific discussions, conversations, and especially our friendship. Certainly, this research would not be the same without his comments and suggestions.

I would like to thank Dr. Francisco A Negri (Chico), who accompanied me on the first reconnaissance work of the main outcrops in the Limeira Intrusion, at the beginning of my undergraduate scientific work. Thanks to the NAP GeoAnalítica staff (José Paulo, José Vinícius, Marcos and Leandro) for their support during sample preparation and analysis steps. Profs. Dra. Adriana Alves, Dr. Carlos José Archanjo, and MSc. Pedro G. Angelini for their availability and assistance, during my learning process of the CSD technique. MSc. Maria Isabel Arroyave did great in performing plagioclase isotopic analysis at MITERAC (USA), thank you so much.

Drs. Benjamin Bley, Valdecir Janasi, Gergely Sazbó, Renato de Moraes, Miguel Basei, Patricio Muñoz, Rogério Azzone, and Marcelo Rocha, from the IGc academic staff, give significant help on petrographic and textural analysis. Dr. Cavallaro, Daniel Cunha and Samuel (Samuca) who helped on geophysical fieldwork and data processing. Discussion with Y. Marangoni and M. Ernesto help to improve the geophysical analysis and interpretations. CPRM, Geological Survey of Brazil allowed using and publishing airborne geophysical data of the Limeira Intrusion and neighboring.

The author thanks FAPESP Thematic Project 2012/06082-6 (Coord. Dr. e. Ruberti) for financial support, and the Coordenação de Aperfeiçoamento de Pessoal de Nível Superior (CAPES) Brazil-Finance Code 001, for an MSc. scholarship.

I am grateful to Vinicius Lach, to help me since the beginning of this research. Thanks, Gustavo Prado, Rafael Casati, Daniel Valle (Banana), Eduardo j. Lopes (Mindy), Francesco Barale (Chicó) and Marcos Muro, those years were easier by your incentive and presence.

I am grateful to Francy. Thank you for your encouragement, companionship, friendship, and your dedication to our plans, which so far have come out as planned and on time. I am also grateful to Judith, our giant dog, not only in size.

Finally, I thank my family, especially my grandmother, whom I owe my interest to the rocks universe!

*“Dans les champs de l'observation le hasard  
Ne favorise que les esprits prepares” Louis Pasteur*

## ABSTRACT

Lino, L.M., 2018, Geometry and stratigraphy of Limeira intrusion (SP-Brazil) [Master's Thesis], São Paulo, Instituto de Geociências, Universidade de São Paulo, 85p.

The Limeira Intrusion is an occurrence related to the Mesozoic continental flood basalts of Paraná Magmatic Province, cropping out at the eastern São Paulo state. It is made up of basic-intermediate rocks with a great diversity of structures, textures, and modal compositions, related to the specific evolutionary process in a magma chamber. 2D forward modeling of magnetometric data, based on available aerial and newly obtained ground data integrated with *in situ* rock magnetic susceptibility measurements, were used to establish its geometry. The results, even considering intrinsic drawbacks of magnetometric theoretical models, are compatible with the geologic-based presumed intrusion geometry. In addition, the stratigraphic analysis of compositional and textural variations, coupled with the structural and geometric features, allowed the interpretation of its emplacement mechanism and thermal evolution. Quantitative textural analysis through crystal size distribution (CSD) of plagioclase crystals, the spatial distribution pattern of structures, microtextures, granulation, and rock-types, evidenced the internal heterogeneities of this occurrence. An approximately 110 m top-to-floor exposure section reveals that its internal heterogeneity was caused by non-instantaneous successive emplacement of three different magma injections. The textural analysis also reveals fine-grained crystals formed under different cooling paths, present in medium- to coarse-grained rocks within the intrusion, next to sharp contacts between different rock compositions. The contacts between different rocks are characterized by hybridization textures and by significant amounts of plumose granophyre-type and plumose plagioclase. The time lapse between consecutive pulses is responsible for a stepwise cooling-path, preservation of hybridization textures, and the development of almost rigid surfaces providing crystals alignment during magma flow. High-resolution Sr-isotopy data demonstrates a complex assembly history, possibly involving filter pressing of residual liquids, and pre-existent crystals before magma installation in coarse-grained rocks. It is also possible to recognize fewer amounts of country-rocks assimilation, which decreases towards the intrusion's core and can be associated with magma migration due to filter pressing processes. In the feeder zone, the evolution of emplacement was marked by an almost continuous decrease in wall-rock assimilation by the consecutive magma batches.

**Keywords:** Limeira intrusion; 2D magnetometric modeling; crystal size distribution (CSD); emplacement model; Paraná Magmatic Province.



## RESUMO

Lino, L.M., 2018, Geometria e estratigrafia da intrusão de Limeira (SP-Brasil) [Dissertação de Mestrado], São Paulo, Instituto de Geociências, Universidade de São Paulo, 85p.

A intrusão de Limeira é uma ocorrência associada aos basaltos continentais Mesozoicos da Província Magmática do Paraná, aflorando na região leste do estado de São Paulo. Esta intrusão é composta por rochas básico-intermediárias que ocorrem com grande diversidade de estruturas, texturas e composições modais, relacionados aos mecanismos evolutivos específicos desta câmara. A modelagem magnetométrica bidimensional, baseado em aerolevantamentos disponíveis e dados recentes obtidos em campo e integrados às medidas de suscetibilidade magnética em rocha, foram utilizados para estabelecer sua geometria. Os resultados, mesmo considerando as desvantagens intrínsecas teóricas do método, são compatíveis com o modelo geológico presumido para esta intrusão. Adicionalmente, a análise das variações estratigráficas de composição e texturas, associados aos parâmetros estruturais e geológicos, permitiram a interpretação dos mecanismos de colocação e evolução térmica desta intrusão. Análises texturais quantitativas através da análise de distribuição de tamanho de cristais (DTC), a distribuição espacial de padrões estruturais, microtexturas, granulação e litotipos, evidenciam a heterogeneidade interna desta ocorrência. A seção de aproximadamente 110 metros de topo-a-base revela que sua heterogeneidade interna foi causada pela injeção sucessiva de pelo menos três pulsos magmáticos. Através da análise textural foram reconhecidos cristais de plagioclásio de granulação muito fina a fina presentes em rochas de granulação média a grossa, formados em diferentes razões de resfriamento e próximo ao contato abrupto entre rochas de diferentes composições. Estes contatos caracterizam zonas onde são reconhecidas texturas híbridas e são marcados pela presença e abundância de intercrescimentos granofíricos do tipo plumoso e plagioclásios plumosos. O espaço de tempo entre pulsos magmáticos consecutivos é responsável pela evolução térmica em etapas nesta intrusão, preservando as texturas de hibridização, e desenvolvendo superfícies com rigidez suficiente para promover o alinhamento de cristais de plagioclásio por fluxo magmático. Análises isotópicas demonstram um processo de colocação complexo para este corpo, possivelmente envolvendo a filtragem por pressão dos líquidos residuais da cristalização dos pulsos iniciais, além da existência de ante-cristais formados antes da instalação das rochas de granulação grossa. Também é possível reconhecer o processo de assimilação de uma pequena parcela das rochas encaixantes, principalmente pelas rochas das bordas, que decai para o centro da intrusão e é marcado pela migração dos líquidos residuais. Na zona de alimentação, a evolução da colocação é marcada pela diminuição do processo de assimilação pelos pulsos seguintes.

**Palavras-chave:** Intrusão de Limeira; Modelo magnetométrico bidimensional; distribuição de tamanho de cristais (DTC); modelo de colocação; Província Magmática do Paraná



## LIST OF FIGURES

- Figure 1:** Image from Google Earth (accessed in May 2017) of the studied area. White arrows indicate the localization of Cavinatto and Basalto 4 quarries, spaced about 800 meters. Dotted lines represent measurement stations, and SP-330 is the Anhanguera Highway. .... 4
- Figure 2:** Illustrative flowchart depicting the main magnetometric data acquisition and processing steps followed in this work. See text for more details. .... 4
- Figure 3:** a) Schematic drawings depicting the main types of granophyre intergrowth between K-feldspar and quartz, according to Smith (1974). b) Granophyre-types intergrowths occurring as mesostasis, interstitial to plagioclase crystals; note the predominance of radial-fringe type and some cuneiform-type, highlighted in red (Central Zone, Sample TF-36). c) Transmitted light image under crossed polarizers of a typical analyzed sample from the Limeira Intrusion (Bottom Intermediate zone, Sample IC-01). Plagioclase (in black) distribution monochromatic image obtained after digitizing the optical image showing in c; touching crystals were slightly spaced, about 1 pixel of distance, before quantitative distribution analysis. .... 8
- Figure 4:** Schematic diagrams depicting a typical linear CSD pattern and the expected dispersions due to crystallizing and mechanical related processes. a) CSD model of steady-state crystallization. b) Increasing nucleation density and crystallinity under constant residence time. Note the formation of a convex-upwards hump, associated with the processes of “coarsening” at the crystallization final stages. c) Increasing residence time considering the same final nucleation density. The same effect might occur coupled with a decrease in final-nucleation density. d) CSD line patterns after increasing nucleation rate due to an increase on the cooling rate, or magma mixing involving two crystal populations generated under different cooling rates. Adapted Higgins (2006). .... 9
- Figure 5:** Geological Map of central-eastern São Paulo state (Brazil), showing Paraná Basin stratigraphic Units, the pre-Cambrian basement, and location of the study area. Rocks of the Tubarão Supergroup (Itararé Subgroup) constitute most of the country rocks for the intrusions related to PMP magmatism. Simplified from Perrota & Salvador (2005). .... 16
- Figure 6:** Schematic (N110E) geological cross section through Limeira intrusion, showing the distribution of the main rock-types, and the localization of the quarries. The figure illustrates the geometry of the intrusion based on the interpretation of field observations. .... 19
- Figure 7:** Total anomalous magnetic field (nT) maps for the Limeira Intrusion based on our ground survey (i) and the available aerial data (ii). The locations of the Cavinatto and Basalto 4 quarries and the AB suggested geologic cross section (Figure 6) are indicated. Note the dipolar anomaly centered over the quarries in both maps and the difference range between the anomalous field intensities. .... 20
- Figure 8:** Analytical Signal Amplitude (ASA, nT/m) maps for the Limeira Intrusion, based on MAF data of ground survey (i) and the available aerial data (ii). Note that the ground data highlights two main regions with high ASA values, while aerial data (more defocused) presents an additional high ASA to southern, related the raw data acquisition contrasted features (white dots). The black dotted line in (i) is our best-estimated intrusion limits based on both maps. .... 21
- Figure 9:** Reduced to Pole (RTP, in nT) maps for the Limeira intrusion, based on MAF to ground survey (i) and available aerial data (ii). Note the high anomaly over the quarries. The AB, CD and EF profiles correspond to total anomaly sections, extracted for the two-dimensional modeling. White dots represent the localization of data acquisition. .... 21
- Figure 10:** Schematic two-dimensional magnetic model of Limeira intrusion, based on the presumed geologic model, total magnetic anomalies (at AB, CD and EF profiles) and magnetic average susceptibility measurements. See text for discussion. .... 23
- Figure 11:** Simplified geological map of the central-east portion of São Paulo state in southeastern Brazil, depicting the main geological units and the location of the Limeira Intrusion (Modified from Perrota & Salvador, 2005). .... 27

- Figure 12:** Geological and structural features of the Limeira Intrusion at the Cavinatto quarry. a) Overlying cross-bedding sandstone at the northern limit the intrusion. b) Laminar plan-parallel stratification in overlying rhythmic siltstone. c) Emplacement-related faults cutting across rhythmic siltstone at the northern upper contact (dotted line) and stereographic projections of the main mapped structures. d) Basic feeder-dike emplaced in subvertical fault, affecting sandstone and siltstone host-rocks. e) Siltstone xenoliths showing domino-fault displacement close to the upper contact, somewhat irregular but almost horizontal. .... 30
- Figure 13:** Thin section of rhythmic siltite hornfels, present in the northwest contact of Limeira intrusion. a) General view exhibiting layers of different granulation. It is possible to observe the presence of a fine-grained sand, and distinctive types of venulations filled by quartz and/or chlorite with the possible hydrothermal origin, perpendicular to sedimentary stratification. The detail depicts quartz grains that contain fluid inclusions related to one of these veins. b) The detail in an argillic layer, where it is possible to observe tabular features, probably resulting in andalusite micro-crystals substitution. .... 31
- Figure 14:** QAP modal diagram for the classification of igneous rocks (Strekeisen, 1976), showing the modal diversity within the Limeira Intrusion. Fields: (1): gabbro/diorite, (2) quartz gabbro/diorite, (3) quartz monzogabbro/monzodiorite, (4): granodiorite. Letters a, b, c,d, and e identify typical trends of the tholeiitic, calc-alkaline tonalitic/trondhjemite, calc-alkaline granodioritic, monzonitic and alkaline plutonic rock series, respectively, as defined by Lameyre & Bowden (1982). Note that basic-intermediate rocks of the Limeira Intrusion conform to the average trend of calc-alkaline granodioritic series. The marked increase in quartz and alkali-feldspar contents are compatible with variations in the stratigraphic level, as well as the distribution of the recognized petrographic facies. .... 32
- Figure 15:** Schematic stratigraphic columns, illustrating the mapped textural, structural, and compositional variations within the Limeira Intrusion. Depth zero corresponds to the horizontal contact with sandstones at the upper contact. The main structural and textural features, the modal content of the main and accessory minerals and of granophyre types are highlighted in the first, second and third columns, respectively. Numbers in the second column identify the location of the rock slabs/outcrops whose digital images are shown in the right. (1) Amygdule- and ocelli-bearing diabase, close to the contact with the intrusion chilled border. (2) “Jaguar-skin”-type quartz-monzodiorite from Upper Intermediate Zone. (3) Grid-type granodiorite from the uppermost region of the Central Zone. (4) Layered series detail showing Cross-bedded modal layering marked by angular unconformities from the Bottom Intermediate Zone. (5) “Jaguar-skin”-type quartz-monzodiorite from Lower Intermediate Zone, intruded by an aplitic dike. .... 37
- Figure 16:** Histograms showing the plagioclase long-axis dimensions distributions and the corresponding cumulative density functions (CDF) for selected samples from the Limeira Intrusion. Grain size frequencies for samples collected in the UBZ (Sample IC-08) and CZ (Sample TF-36) homogeneous zones with close to log-normal distributions (a and b). Figures c and d are from the Hybrid zones 1 e 2 (samples IC-07a and IC-04c, respectively). Note the bimodal distribution and inflections on the CDF curves, best developed in the Hybrid zone 1, pointing out to two plagioclase crystal size families. .... 39
- Figure 17:** Plagioclase crystal morphologies within the Limeira Intrusion, as defined by their intermediate- to long-axis and short- to intermediate-axis relative ratios, according to Zingg (1935). See text for discussion. .... 40
- Figure 18:** CSDs patterns for the analyzed samples from the main zones of the Limeira Intrusion, grouped accordantly with similar features and stratigraphic position. Note that the legend for each sample includes the distance in meters from the nearest contact. a) Lower (quartz diorites) and Upper (gabbros and microgabbros) Border zones showing both grain size and residence time increasing inwards. b) Lower Intermediate, Central and Upper Intermediate Zones (quartz-monzodiorites and granodiorites) CSD plots. Note grain size increasing towards the Central Zone, coupled with a minor residence time increase. c) Hybrid Zone 1, from the upper contact of the Upper Intermediate Zone, showing inflections in CSD curves for crystal sizes less than 1mm. d) Hybrid zone 2, from the lower contact of the Upper Intermediate Zone, showing minor relatively inflections patterns and accentuated convex-humps resulting from relatively smaller crystals in sample IC-04. .... 42
- Figure 19:** Plot of plagioclase characteristic length variations as a function of the CSD lines intercept (final nucleation density,  $n_0$ ) for the results of this study. Calculated closure limit for the average plagioclase aspect ratios (short-: medium-: long-axis = 1:1,6:2,8) considering 100 vol.% crystals (heavy dotted line),

50 vol.% and 150 vol.% (lower and upper light-dotted lines, respectively), following Higgins (2002). Note data distribution along the closure limit and their dependence of the intrusion stratigraphy (central vs. borders zones). The hybrid zones data describe a contrasted path, indicating a relatively lower plagioclase nucleation density. See text for discussion. .... 45

**Figure 20:** Plagioclase characteristic length variation as a function of modal abundance, parameters take as representative of growth-rate and growth-time, respectively (Higgins, 2002). The arrow indicates the approximated trend of textural coarsening within Limeira intrusion; shaded areas depict the dispersion of the Hybrid Zones in relation to the main expected trend. See text for discussion. .... 46

**Figure 21:** R-values versus the matrix abundance (= 100% - plagioclase% vol.) for the CSD results obtained in this study. The Random Sphere Distribution Line (RSDL), as calculated by Jerram et al. (1996), limits clustered from ordered crystal arrangements. Note an almost progressive increase in R-value, coupled to decrease in matrix proportion, from the center to border regions within Limeira intrusion. The shade highlights an observed dispersion, caused by rocks present on Hybrid Zones. See text for discussion. 47

**Figure 22:** Plagioclase crystal clustering (R-Value, a) and alignment factor (AF, b) parameters variations as a function of depth within the Limeira Intrusion. Hybrid zones represented by shaded areas are critical zones defined by the contacts among the main rock-types. Note the correspondence with low R-values and high Alignment Factor values with the critical zones. c) The corresponding rose diagram to each sample, almost N-S oriented generally. .... 49

**Figure 23:** ICSD-type diagrams correlating plagioclase crystal size with ( $^{87}\text{Sr}/^{86}\text{Sr}$ ); isotopic initial ratios. a) Sample IC-07a, from the Hybrid-zone 1. Note the kink in the CSD curve coinciding with an abrupt change in isotopic ratios highlighted by the dotted line. b) ICSD plot for TF-36 sample, present in the central region of Limeira intrusion, and c) LIM-02 sample, present at the intrusion's feeder zone. Boxes were drawn with  $\pm 2\sigma$  of uncertainty on isotopic ratios. Initial ratios calculated for a 132 Ma age. The Upper horizontal gray bar represents a whole-rock isotopic initial ratio, from Oliveira & Dantas (2008), and the lower horizontal light-red bar represents the average baseline common for all samples. .... 50

**Figure 24:** Diagrams illustrating the main variation patterns of plagioclase CSD parameters and depth within the Limeira Intrusion. The two model curves in each plot show the expected behavior in steady-state crystallizing systems. a) Intercept vs. slope plot: relatively homogeneous samples from several stratigraphic positions within the intrusion are represented in blue; samples from the hybrid zones and from the lowermost intrusion level in black. b) Depth (\*distance from the nearest contact) vs. crystal mean length plot. Both diagrams indicate significant departures from single models based on a steady-state magmatic evolution. Constant C=2. .... 54

**Figure 25:** Charts illustrating the proposed emplacement model for the Limeira Intrusion. a) First magma pulse emplacement through the feeder dike along a sub-vertical discontinuity. Continuous flow and intrusion along the siltstone-sandstone horizontal contact actionng as a "less-stress" structural plane, which results in faulting and upward moving of the sandstone layers over the flow. b) The first magma pulse increases the local rheological contrast, providing the emplacement of subsequent magma batches within the first intrusion, at the region with more ductile behavior. c) The installation of the latter magma pulse, resulting of mid-accretion and final estimated geometry of Limeira intrusion, results of the same acting emplacement mechanism. d) Expected CSD patterns within the constitute intrusion and hybrid zones, velocity profiles, deduced from R-value distributions, and simple shear components at the contacts between magmatic pulses. .... 56

## LIST OF TABLES

<b>Table 1:</b> Reference values of inclination and declination for induced and remnant magnetization vectors and the computed total magnetization vector.....	6
<b>Table 2:</b> Magnetic susceptibility ( $\times 10^{-3}$ SI) and average modal composition of opaque phases (mainly Ti-magnetite/magnetite and ilmenite) within the measured samples representative of the main rock types exposed in the Limeira Intrusion.....	18
<b>Table 3:</b> Modal composition of the Limeira intrusion representative samples and estimated errors. ....	33
<b>Table 4:</b> Results of the analyzed area, number of crystals, volumetric proportions, and aspect ratio (calculated using CSDslice 5). *Volumetric proportion obtained by point counting. ....	41
<b>Table 5:</b> Crystal Size Distribution coefficients obtained on each regression lines. Values of $n_0$ correspond to final nucleation density (Y-axis intercepts), $C_i$ is the characteristic length ( $-1/\text{slope}$ ), slope corresponds to the inclination of lines. $R^2$ is the coefficient of correlation of regression, and L (max) is the maximum crystal length for each sample. ....	44
<b>Table 6:</b> Spatial Distribution Patterns values for each analyzed sample and its stratigraphic position.....	48
<b>Table 7:</b> Isotopic $^{87}\text{Sr}/^{86}\text{Sr}_i$ ratio, uncertainty, and core distance for plagioclase crystals. ....	51
<b>Table 8:</b> Values of residence time, cooling rate, and the distances from Limeira intrusion's borders.....	53
<b>Table 9:</b> Residence time and plagioclase volumetric proportion from hybrid zones. ....	55

## SUMMARY

ABSTRACT .....	vii
RESUMO .....	ix
LIST OF FIGURES .....	xi
LIST OF TABLES .....	xiv
SUMMARY .....	xv
CHAPTER I.....	1
I.1. INTRODUCTION .....	1
I.2. OBJECTIVES.....	1
I.3. PRESENTATION AND STRUCTURE OF THE DISSERTATION .....	2
CHAPTER II .....	3
II.1. MATERIALS AND METHODS.....	3
II.1.1. Geophysical data acquisition and treatments .....	3
II.1.2. Sampling and field work .....	6
II.1.3. Modal measurements.....	6
II.1.4. Textural analysis rationale, data acquisition, and treatment .....	7
II.1.4.1. Principles of CSD theory .....	8
II.1.4.2. Spatial distribution patterns (SDP).....	10
II.1.4.3. Shape preferred orientation (SPO) of crystals .....	10
II.1.5. Sr isotope ratios in plagioclase and ICSD plots .....	12
CHAPTER III.....	13
2D MAGNETOMETRIC MODELING OF A BASIC-INTERMEDIATE INTRUSION GEOMETRY: GEOPHYSICAL AND GEOLOGICAL APPROACHES APPLIED TO THE LIMEIRA INTRUSION, PARANÁ MAGMATIC PROVINCE (SP, BRAZIL).....	13
III.1. INTRODUCTION .....	14
III.2. GEOLOGICAL FRAMEWORK.....	15
III.2.1. Limeira Intrusion .....	16
III.2. RESULTS AND DISCUSSION .....	17
III.2.1. The geologic suggested model .....	17
III.2.2. Geophysical analysis .....	19
III.2.2.1. Magnetic anomaly maps.....	19
III.2.2.2. Magnetometric forward modeling.....	22

III.3.	CONCLUDING REMARKS .....	23
	CHAPTER IV .....	25
	QUANTITATIVE TEXTURAL ANALYSIS AND Sr-ISOTOPY IN PLAGIOCLASE APPLYING TO REVEAL EMPLACEMENT MECHANISM AND THERMAL EVOLUTION OF LIMEIRA INTRUSION, PARANÁ MAGMATIC PROVINCE, BRASIL .....	25
IV.1.	INTRODUCTION.....	26
IV.2.	GEOLOGICAL SETTING.....	27
IV.2.1.	Paraná Magmatic Province .....	27
IV.1.2.	Limeira Intrusion.....	28
IV.3.	GEOLOGY AND STRATIGRAPHY .....	29
IV.3.1.	Host rocks and structural aspects .....	29
IV.3.2.	Petrographic facies .....	31
IV.3.3.	Internal stratigraphy .....	34
IV.4.	QUANTITATIVE TEXTURAL ANALYSIS .....	38
IV.4.1.	Statistical analysis of crystal-size populations.....	38
IV.4.2.	Stratigraphic variations of plagioclase crystal-shape and modal abundance....	39
IV.4.3.	Crystal size distribution .....	41
IV.4.4.	Internal variability of crystal sizes and CSD closure limit .....	44
IV.4.5.	Spatial distribution patterns of crystals .....	46
IV.4.6.	Emplacement mechanisms and influence of magma flow to rock fabric .....	48
IV.4.7.	Sr isotope constraints and ICSD plots.....	50
IV.4.8.	Residence time and thermal evolution .....	52
IV.5.	DISCUSSION .....	55
IV.5.1.	Structural and compositional aspects .....	56
IV.5.2.	The influence of magma emplacement dynamics on CSD and SDP .....	57
IV.5.3.	ICSD analysis and evolution of crystal populations .....	58
IV.5.4.	Effects of time-span between magmatic pulses and thermal evolution .....	58
IV.6.	CONCLUSION .....	60
	CHAPTER V.....	61
V.1.	SYNTHESIS AND CONCLUSIONS .....	61
	REFERENCES.....	63

APPENDIX A .....	69
APPENDIX B.....	73
APPENDIX C.....	75



## CHAPTER I

“If I have ever made any valuable discoveries, it has been owing more to patient attention, than any other talent.” Sir Isaac Newton

### I.1. INTRODUCTION

The Limeira intrusion (SP-Brazil) is a basic-intermediate occurrence associated to the Paraná Magmatic Province (PMP), which crops out into two quarries (Cavinatto and Basalto 4) and provides a well top-to-bottom exposition of the intrusion-forming rock-types. These exposures allows to examine atypical features, rarely seen in other analogous intrusions, such as (1) the preservation of structural relationship with host-rocks at the uppermost contact, (2) expanded compositional variation, including since basaltic to rhyolitic rocks, as well as a significant late hydrothermal input, and (3) a significant variety of magmatic structures and textures. In this sense, [Lino \(2015\)](#) and [Lino \*et al.\* \(2018\)](#) draw attention to its compositional, structural and textural variability inwards, pointing in evidence a more complex emplacement- and magmatic-evolutionary model, rather than a single magma batch that evolved under the process of fractional crystallization, as it had been previously considered. Previous geological studies give some support for a lopolithic-like intrusion form (*e.g.*, [Lino, 2015](#)), and coupled with the distribution of rock-types, structures, textures, and chemical compositions, these data are suggestive of a multiple stage emplacement.

### I.2. OBJECTIVES

Evolutionary magmatic models of intrusive occurrences are strictly dependent on their final volumes, geometry variations during the emplacement process, magmatic accretionary rates, initial compositions, volatile content, and magma initial temperature. Even representing important information to the modeling of the magmatic process, the geometry (volume) and emplacement mechanisms of igneous intrusions are still a subject of interest. Due to its small size and volume, as well as the singular mode of exposure, the Limeira intrusion becomes a preferential object of study when dealing with geometry and emplacement models, among the regional igneous intrusions from the Paraná Magmatic Province. The main objectives of this research were to determine the main geometric features of Limeira intrusion through geophysical modeling, as well as to establish its internal stratigraphy and petrographic facies distribution in detail, providing a better background for the analysis of emplacement mechanisms and the magmatic evolution of this magma chamber. The achievement of these

objectives was sectioned into two steps to simplify the approach, resulting in the principal sections of this dissertation, presented as scientific papers. Specifically, the main research aims were:

- Characterization of Limeira intrusion geometry, based on geophysical magnetometric modeling;
- Detailed characterization of the basic-intermediate rocks petrographic properties to properly classify the occurring rock-types, as well as to define the internal stratigraphy of the intrusion;
- Characterization of the main structural patterns and quantification of the main micro-textural variation within this magma chamber;
- Quantification of the grain-size distribution (CSD) and spatial distribution patterns (SDP) of plagioclase crystals;
- The proposition of compatible models for emplacement, magmatic and thermal evolution of the intrusion.

### **I.3. PRESENTATION AND STRUCTURE OF THE DISSERTATION**

The present dissertation results of a multidisciplinary approach applied to model the geometric features as well as the emplacement mechanisms of Limeira intrusion. In this sense, it is presented a geophysical 2-D modeling based on ground- and aerial-magnetometric measurements, combined with quantitative textural analysis and geological aspects that put in relief the main internal heterogeneities of the intrusion. This dissertation is constituted of five chapters, among them, two are presented in the form of scientific papers. The current Chapter (I) introduces the main topic and presents the aims of this work. Chapter II details the scientific approach and the methods carried out to achieve the research objectives. The Chapters III and IV present scientific manuscripts. The first, published in the Brazilian Journal of Geology, deals with magnetometric analysis, 2-D modeling and their results, while the second deals with micro-textural analysis, stratigraphy, and inferences on the emplacement and thermal evolution models, and is in final reviewing process to be submitted to an international journal. These chapters describe in some detail the intrusion regional setting and previous work, in this sense they will not be repeated in this introduction. The last Chapter (V) summarizes, integrates and discusses the obtained results.

## CHAPTER II

“No great discovery was ever made  
without a bold guess” Sir Isaac Newton

### II.1. MATERIALS AND METHODS

In this research, the scientific approach followed classical methods applied for the investigation of intrusive igneous rocks, based mainly on previous geological and petrographic results presented by Lino (2015). In short, geophysical surveys were carried out in the Cavinatto quarry and surrounds, considering the occurrence area of Limeira intrusion, as delimited by Seixas *et al.* (2015). Both magnetometric and some gravimetric data were obtained. At this step, rock-type classification followed those proposed by Faria (2008) and Lino (2015).

After concluding the geophysical modeling, classical detailed geological and petrographical facies (Ulbrich *et al.*, 2001) mapping were conducted, followed by petrographic compositional and textural descriptions, quantitative textural analysis, and *in situ* plagioclase isotopic measurements. Whole-rock and mineral chemical analysis, including *in situ* plagioclase trace elements, were also obtained and considered during the research. They will be presented elsewhere (Lino & Vlach, in preparation), and are not considered in this dissertation. The laboratory work was performed mainly at the GeoAnalitica core facility, from the IGc-USP. The Sr-isotope and trace elements analysis were carried out at the MITERAC (USA), conducted by MSc. Maria Isabel G. Arroyave.

A somewhat more detailed description of the applied methods is given in chronological sequence, as follows:

#### II.1.1. Geophysical data acquisition and treatments

Total magnetic field (TMF) measurements were performed with two Proton Precession Overhauser Magnetometers (Gem System, models GSM-19), with coupled high-precision GPS systems, in 516 field stations listed in the **Appendix A**. One of them was used for diurnal variation measurements on a fixed station far from potential anthropogenic influence, while the other was used as the rover station. The average distance between two successive measurement stations was about 30 m (**Figure 1**).

Magnetic susceptibility (MS) data were obtained for 57 rock samples. The measurements were made on regular surfaces or slices of fresh hand samples with portable equipment from GF Instruments. On the average, ten measurements were taken on each sample. In the studied rocks, the MS values are directly correlated with the magnetite/Ti-magnetite modal content.

Data processing and treatment procedures are summarized in **Figure 2** (see also Cavallaro, 2013 and Milsom, 2003). The TMF values, registered on the base and rover stations, were imported into the Geosoft's Oasis Montaj® software and corrected for the diurnal magnetic variations and the International Geomagnetic Reference Field, IGRF (<http://www.ngdc.noaa.gov/seg/geomag/jsp/IGRF.jsp>, accessed in May 2017)



**Figure 1:** Image from Google Earth (accessed in May 2017) of the studied area. White arrows indicate the localization of Cavinatto and Basalto 4 quarries, spaced about 800 meters. Dotted lines represent measurement stations, and SP-330 is the Anhanguera Highway.

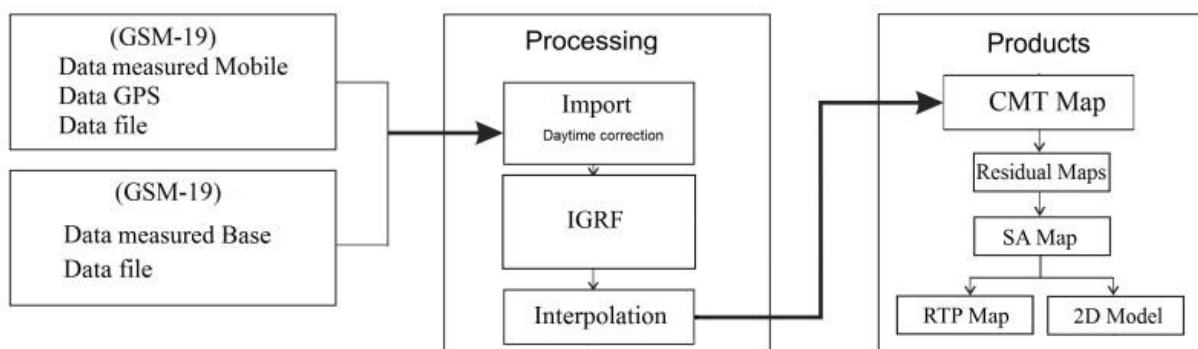


**Figure 2:** Illustrative flowchart depicting the main magnetometric data acquisition and processing steps followed in this work. See text for more details.

The final processing steps included data interpolation by the minimum curvature (MC) method (Briggs, 1974), analytical signal amplitude (ASA) filtering and the reduction to pole (RTP) systematics. The RTP systematics followed suggestions set out by Phillips (2007), considering the frequency domain, to highlight the main features and generate geophysical

maps. The available aeromagnetometric data (CPRM, Rio-São Paulo Project 1039, carried out 150 m high) was similarly treated in order to provide a comparison and better interpretation.

The ASA filter may be used to detect the main edges and geometric features of geological occurrences with significant magnetic contrast (*e.g.*, Nabighian, 1972). With this procedure, the horizontal and vertical gradients of the detected anomalous potential field normally form a maximum and minimum pair of analytical signals; the former depicts the edges, while the latter highlights the center of the involved occurrences (Nabighian, 1984).

In the case of 3D analysis, the ASA filter - which represents a horizontal plane – depends on the inclination and declination directions of the target’s magnetization and the geomagnetic field; therefore the filter can be applied for edge estimation under some specific conditions (Li, 2006). In this way, the ASA maximum is located over the causative body’s edge only when it occurs at shallow depths and can migrate with increasing depths to the center of the targets. According to the author, ASA filter works well for edge-detection, considering a prismatic model, when the ratio between the body top depth and its width is less than 0.1.

Based on synthetics models, Ferreira *et al.* (2013) have shown that the ASA filter effectively depicts up the edges of geological occurrences with a constant thickness. The authors have also demonstrated different methods for edge detection, based mainly on directional derivatives. The ASA filter is defined by the following equation 1, where M is total magnetic anomalous field, and x, y, and z represents three-dimensional directions in the space.

$$ASA = \left[ \left( \frac{\delta M}{\delta x} \right)^2 + \left( \frac{\delta M}{\delta y} \right)^2 + \left( \frac{\delta M}{\delta z} \right)^2 \right]^{1/2} \quad (1)$$

The RTP systematics (Baranov, 1957) was applied to recalculate data intensity as well as to transpose the magnetic anomalous field (MAF) onto the geomagnetic pole reference, where the induced magnetization is in the vertical position. If the total magnetization direction is known (Kearey & Brooks, 2002), it turns the induction polarization independent of the direction of the geomagnetic field (Telford *et al.*, 1976), by transforming the dipolar anomaly into a monopolar one (*e.g.*, Baranov, 1957; Nabighian, 1972, 1984). In the frequency domain, the RTP systematics is defined by the following equation 2, where  $I$  is the magnetic inclination;  $D$  is magnetic declination, and  $I_a$  is a correction parameter for the amplitude.

$$L(\theta) = \frac{1}{[\sin(I_a) + i \cos(I) \cos(D - \theta)]^2}, \text{ if } (|I_a| < |I|), \text{ then } I_a = I \quad (2)$$

The remnant magnetization affects the interpretation of magnetic anomalies and generates misinterpretation concerning targets shape and size (e.g., [Cordani & Shukowski, 2009](#)). The South Atlantic Anomaly ([Hartmann & Pacca, 2009](#)), characterized by low magnetic intensities in southern America, results in a natural remnant magnetization more important than the induced one. Thus, the theoretical response may be not compatible with the observed anomaly. The available paleomagnetic data ([Ernesto \*et al.\*, 1999](#)) was used to correct, through conventional vectorial sum, the inclination and declination directions of the total magnetization. The reference values used as well as the resulting total magnetization vector are summarized in **Table 1**, where the remnant ( $J_r$ ) and induced ( $J_i$ ) magnetizations can be expressed as the Königsberger ratio ( $Q = J_r/J_i$ ).

**Table 1:** Reference values of inclination and declination for induced and remnant magnetization vectors and the computed total magnetization vector.

<b>Magnetization direction</b>	<b>Inclination (°)</b>	<b>Declination (°Az)</b>
<b>Induced</b>	-35.89	-21.08
<b>Remnant (Ernesto <i>et al.</i> 1999)</b>	-34.30	354.70
<b>Total magnetization vector</b>	-35.30	-13.10

2-D forward magnetic modeling was conducted from total anomaly profiles, exported from Geosoft, using the GRAVMAG software ([Pedley \*et al.\*, 1997](#)). This software allows constructing polygons with different forms and magnetic susceptibilities using measured data profiles to create a theoretical anomaly, which could be successively refined to a best possible solution. In this sense, a previous good geological framework is necessary to build any magnetic coherent models ([Pedley \*et al.\*, 1997](#)).

### **II.1.2. Sampling and field work**

After a previous detailed geologic and petrographic characterization, we conducted a systematic sampling of the main rock varieties within the Cavinatto quarry, considering modal compositions, structures, textures, as well as the stratigraphic level. About 80 oriented samples, precisely located with the aid of portable GPS and barometer, were collected for this work, among them, 30 were considered for detailed petrographic analysis. The localization of each sample within Cavinatto quarry are listed in the **Appendix B**. The orientation of riptile structures and rock-contacts were measured using a conventional compass.

### **II.1.3. Modal measurements**

Conventional modal measurements were carried out over polished thin sections, by point counting ([Chayes, 1965](#)), considering square grids with 2,000 points spaced by 0.2 mm

for the fine-grained varieties, and 2,500 points spaced by 0.3 to 0.4 mm for medium- and coarse-grained ones, respectively, over an area close to total thin-section. The associated standard deviations were estimated from 4-5 coining blocks, constituted by 500 points each.

Due to the occurrence of contrasting granophyre-types (intergrowths of K-feldspar and quartz) within and among samples, and considering that they can qualitatively record different cooling-rates during the late magmatic stage (Barker, 1970; Smith, 1974), we also attempted to quantify their diversity. Four main granophyre-types, occurring as isolated mesostasis between plagioclase and clinopyroxene crystals (i.e. **Figure 3a**), are present in our samples and can be classified as: (1) plumose-, (2) radial-fringe, (3) vermicular-, and (4) cuneiform-types (**Figure 3b**), indicating an increase in residence time, respectively. In each sample, 500 points on average were counted, spaced by 0.1 mm over the granophyre areas. The relative modal abundance of quartz and alkali-feldspar were measured for the cuneiform granophyre-type intergrowth in four selected samples over optical microscopic images of ideal sections, resulting in an average of 47% ( $\pm 2\%$ ) of quartz, and 53% ( $\pm 2\%$ ) of alkali-feldspar.

#### **II.1.4. Textural analysis rationale, data acquisition, and treatment**

Plagioclase CSD analysis was conducted for 17 selected samples, from the edge to the core of the intrusion. Crystals were drawn with the aid of Inkscape software, which allows obtaining vectorized images (**Figure 3c, d**). Samples with granulation up to 4.0 mm were photographed under a 5-fold magnification petrographic microscope, under both plane polarized and cross-polarizer lights. Additionally, photomosaic and high-resolution scanned images were also produced. Therefore, in order to generate reproducible CSD, at least ~200 crystals are sufficient and were counted for coarse-grained samples and at least ~300 crystals for fine-grained ones (Mock & Jerram, 2005; Gualda, 2006). Volumetric proportion of plagioclase crystals were determined using CSD results and then compared to modal obtained data, which resulted in maximum errors of  $\pm 0.5\%$  (one sigma). For most samples, there was no distinguishable fabric, except for the sample LIM-02, which was considered during stereological corrections.

The treatment of ready-made images was made using the Image-J software (Abramoff *et al.*, 2004), to analyze crystals' shape and size distribution. It results in each location of the crystal's centroid, the area of each crystal, orientation angle of the major axis in relation to the horizontal, and size of the major and minor axes of the adjustment ellipse - with equal area. Analyzed particles had sizes larger than 10 pixels, and the results were exported in CSD format. The stereological correction processes were performed using the CSD slice spreadsheet, to

estimate the best plagioclase crystals 3-D shape (Morgan & Jerram, 2006), and CSD-Corrections v 1.55 software was used to calculate CSD lines. In the next section, we briefly describe some important aspects of the CSD theory and the methods for the determination of crystals spatial distribution patterns and alignment.

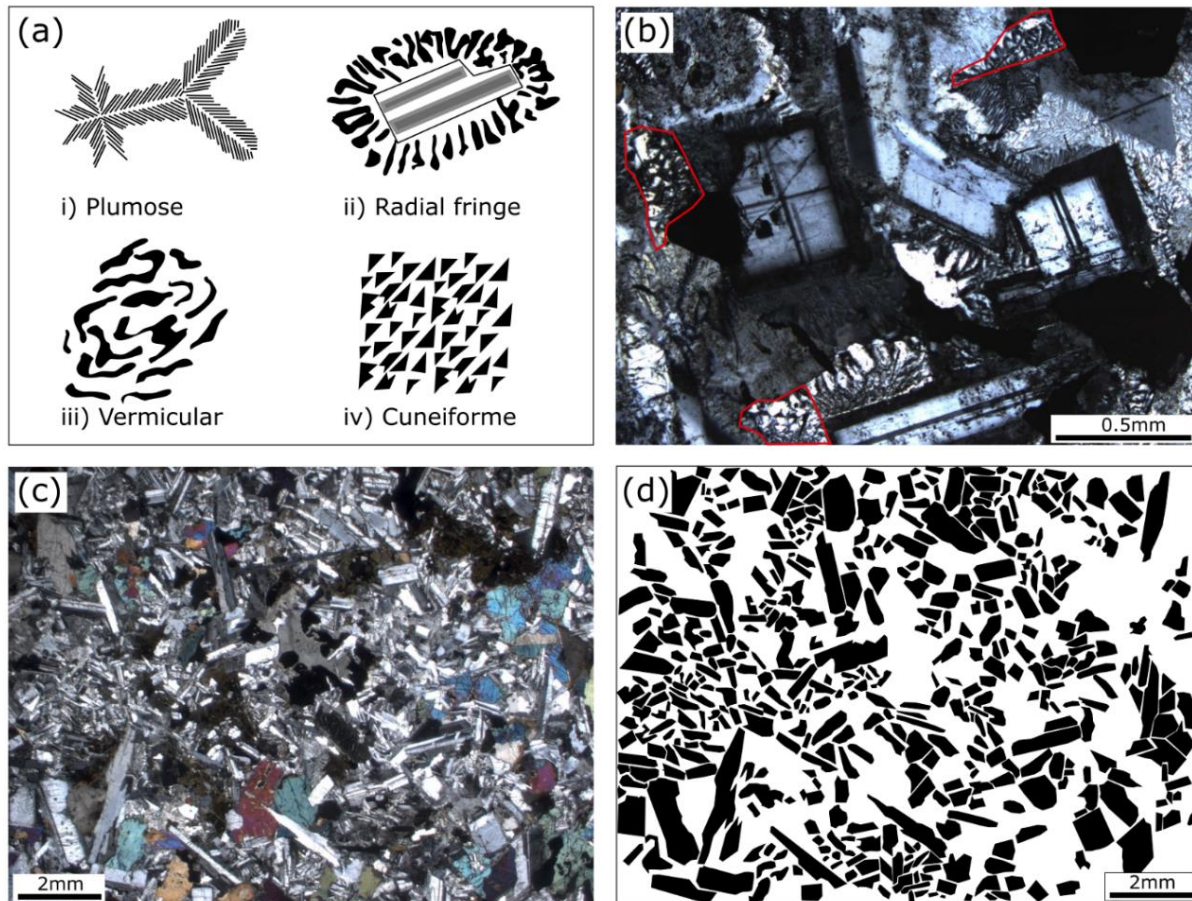


**Figure 3:** a) Schematic drawings depicting the main types of granophyre intergrowth between K-feldspar and quartz, according to Smith (1974). b) Granophyre-types intergrowths occurring as mesostasis, interstitial to plagioclase crystals; note the predominance of radial-fringe type and some cuneiform-type, highlighted in red (Central Zone, Sample TF-36). c) Transmitted light image under crossed polarizers of a typical analyzed sample from the Limeira Intrusion (Bottom Intermediate zone, Sample IC-01). Plagioclase (in black) distribution monochromatic image obtained after digitizing the optical image showing in c; touching crystals were slightly spaced, about 1 pixel of distance, before quantitative distribution analysis.

#### II.1.4.1. Principles of CSD theory

Marsh (1988) and Cashman & Marsh (1988) introduced and validated the Crystal Size Distribution (CSD) theory for a steady-state magmatic system based on previous work by Randolph & Larsen (1971), which demonstrate the constant relation between crystal growth-rate and crystallization time in industrial crystal production processes. In short, there is a linear correlation between the natural logarithm of the crystal population density at a given crystal size (L) of a mineral phase and the correspondent size, as described by the following equation 3 (Marsh, 1988).

$$\ln(n) = \ln(n_0) - \left(\frac{1}{G\tau}\right)L \quad (3)$$

where  $n$  is the population density of crystals in a given size  $L$ ,  $n_0$  is the final nucleation density (at  $L = 0$ ),  $G$  is the effective growth rate ( $= dL/dt$ ), and  $\tau$  the effective residence time or crystallization interval. The parameter  $G\tau$  is intrinsic to the system, and corresponds to  $\bar{L}$ , the mean (or characteristic) length of crystals, considering since zero to infinite  $L$  values in a straight CSD distribution pattern. The nucleation rate of crystals ( $J$ ) depends on the final nucleation density and the growth rate; it increases exponentially over time and is given by  $J = (\ln(n_0))G$ . The CSD line slope  $S = -1/G\tau (= -1/\bar{L})$  is inversely proportional to growth rate and residence time of crystals.

The CSD model allows predicting dispersions from any of these parameters operating during magma crystallization (Marsh, 1998; Zieg & Marsh, 2002). Typical examples are illustrated in **Figure 4**, which highlights the effects over the standard model caused by increasing nucleation density and residence time. The evolving paths of real magmatic chambers are more complex as compared with the predicted by the steady-state CDS theory, and the log-linear crystal size patterns are affected by changes in cooling- and growth-rates, as well as crystal fractionation or mixing (Marsh, 1988; Burkhart *et al.*, 1980; Marsh, 1998). For instance, CSD line inflections, as represented in **Figure 4d**, could indicate system reheating through the emplacement of a new magma batch, leading to more than one cooling stage, or magma mixing (Marsh, 1988; Cashman & Marsh, 1988; Jerram *et al.* 2003).

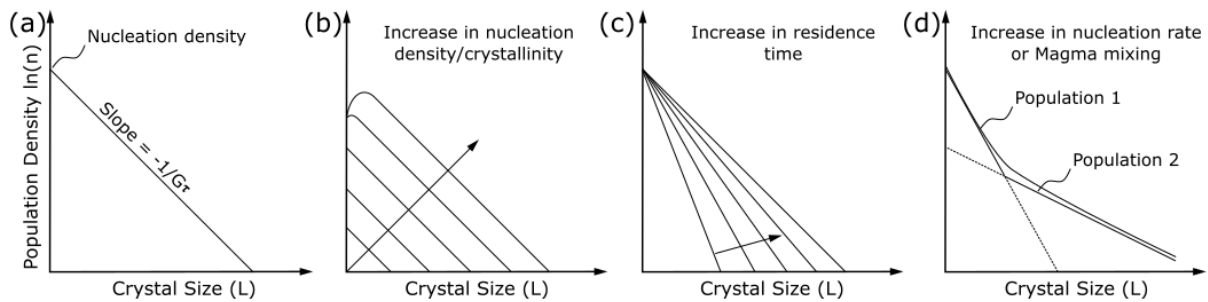


**Figure 4:** Schematic diagrams depicting a typical linear CSD pattern and the expected dispersions due to crystallizing and mechanical related processes. a) CSD model of steady-state crystallization. b) Increasing nucleation density and crystallinity under constant residence time. Note the formation of a convex-upwards hump, associated with the processes of “coarsening” at the crystallization final stages. c) Increasing residence time considering the same final nucleation density. The same effect might occur coupled with a decrease in final-nucleation density. d) CSD line patterns after increasing nucleation rate due to an increase on the cooling rate, or magma mixing involving two crystal populations generated under different cooling rates. Adapted Higgins (2006).

#### II.1.4.2. Spatial distribution patterns (SDP)

As CSD's are related to the crystallization parameters of a magmatic system, the spatial distribution patterns (SDP) and the shape preferred orientation (SPO) of crystals reflect physical mechanisms acting during magma emplacement and crystallization (*e.g.*, Jerram & Cheadle, 2000). Jerram *et al.* (1996) developed a technique for determining the SDP parameter through the cluster analysis, considering the relationship between crystal's centroid positions based on the R-values, given by:

$$R = \frac{r_A}{r_E} = \frac{\frac{1}{N}\sum r}{\frac{1}{\sqrt{N_A}}} \quad (4)$$

where  $r_A$  and  $r_E$  are the ratios between the average nearest-neighbors in the sample and that expected for a random distribution with a same population density respectively; N is the number of crystal centroids, r the distance to the nearest neighbor, and  $N_A$  the number of crystals per unit area in the random pattern. Accordantly, R-values =1, < 1 and > 1 indicates random, clustered and ordered point distributions, respectively. By calculating R-values from 2-D sections of 3-D random distributions of spheres with variable porosities, the authors were able to define a Random Sphere Distribution Line (RSDL), which allows identify real clustered and ordered crystal distribution patterns in real rock frameworks.

Cluster analysis can also be applied to quantify the packing process during the crystallization of igneous rocks, and regions characterized by touching- and non-touching frameworks can be delimited in R-value vs. melt vol.% (or porosity vol.%) plots (Jerram *et al.*, 2003). As shown by Boorman *et al.* (2004), typical vectors for cluster variations trends expected from deformational compaction, overgrowth, and mechanical compaction processes can also be drawn in such plots.

#### II.1.4.3. Shape preferred orientation (SPO) of crystals

Crystal orientation in igneous rocks results from magmatic plastic deformation in a laminar flux when the magma underwent a simple-, hyperbolic-, or a pure-shear flow (Turcotte *et al.*, 1987; Fialko & Rubin, 1999; Higgs, 2006). The orientation ability depends on crystal shape and size, where no-equant crystals shapes register more efficiently shear directions (Iezzi & Ventura 2002). The calculation of a mean orientation angle is a widespread routine used to estimate the preferred alignment direction of crystals (Capaccioni *et al.*, 1997); however, this procedure does not yield information about data dispersion. The length of the orientation vector, obtained through the following equation 5, adds significance of mean angle orientation and can

be tested in statistical tables (Swan & Sandilands, 1995). Resultant vectors greater than 0.244, for a 95% significance and  $n > 50$ , can indicate a preferred orientation (Davis, 1986). As demonstrated by Mock *et al.* (2003), the vector-length can validate the results of the mean orientation angles when its values are greater than the threshold.

$$\bar{R} = \frac{1}{n} \sqrt{(\sum \sin \theta_i)^2 + (\sum \cos \theta_i)^2} \quad (5)$$

In the case of a more complex stratigraphic distribution, the crystals might present a slight dispersion in orientation. The variation of the vector-length is not linear, making difficult the direct comparison of orientation results. In order to compare the alignment results through a linear function, the former component can also be determined using the cosine-tensor direction (T), associated to its first eigenvector (Launeau & Cruden, 1998). The direction of the cosine-tensor can be calculated by equation 6, where  $n$  is the number of crystals and  $\theta$  is the orientation angle.

$$T = \frac{1}{n} \begin{vmatrix} \sum \sin(\theta_i)^2 & \sum \sin(\theta_i) \cos(\theta_i) \\ \sum \sin(\theta_i) \cos(\theta_i) & \sum \cos(\theta_i)^2 \end{vmatrix} \quad (6)$$

Through this approach, the orientation dispersion is calculated from eigenvectors  $e_1$  and  $e_2$ , in which a random distribution results in  $e_1=e_2=0.5$ , and a perfect alignment results in  $e_1=1$  and  $e_2=0$ . From eigenvectors is possible to derivate the axes of orientation of the ellipse ratio as  $r = \sqrt{e_1/e_2}$ , varying from one in massive rocks, to zero in perfectly foliated rocks. It is also possible to calculate the Alignment Factor (AF), as  $AF=2(e_1 - 0.5)$ , with results ranging from 0 to 1 (alternatively ranging from 0 to 100) for massive to completely foliated rocks.

### II.1.5. Sr isotope ratios in plagioclase and ICSD plots

Sr isotope analysis of plagioclase was performed by a Multi-Collector Inductively Coupled Plasma Mass Spectrometry, with Laser Ablation sampling (LA-MC-ICP-MS) at the Mid West Isotope and Trace Element Research Analytical Center (MITERAC), from the University of Notre Dame - the USA. In situ analysis was carried out over thick (*ca.* 60  $\mu\text{m}$ ) polished sections from three samples, representative of three main stratigraphic levels. Measurements were made using a 150 $\mu\text{m}$  diameter laser beam and time to ablation of 60 seconds. Analytical conditions for measurements were conducted with the following set up, Irradiance: 1.49 GW/cm<sup>3</sup>, Fluence: 4.46 J/cm<sup>3</sup>, and Repetition rate: 5Hz.

The analytical strategy and interference corrections over the Sr and Rb isotopes followed [Ramos \*et al.\* \(2004\)](#) and [Paton \*et al.\* \(2007\)](#). The isobaric interference of <sup>87</sup>Rb over <sup>87</sup>Sr was corrected using <sup>85</sup>Rb corrected signal intensities. A modern-day coral (MR) from the Indian Ocean (<sup>87</sup>Sr/<sup>86</sup>Sr = 0.70910 $\pm$ 0.00003, ID-TIMS measurements, *cf.* [Bizarro \*et al.\*, 2003](#)) was used as the main reference; the average <sup>87</sup>Sr/<sup>86</sup>Sr on MR obtained during our analysis was 0.70915 $\pm$ 0.00007 (2 $\sigma$ , N=30).

Initial <sup>87</sup>Sr/<sup>86</sup>Sr isotope ratios were computed considering 132 Ma. as the average age of the intrusion and then integrated with the obtained CSD data following the procedures described by [Morgan \*et al.\* \(2007\)](#) to drawn ICSD-type plots. The location of each analytical spot was calculated as a distance fraction from crystal core to rims and then normalized to the measured crystal-sizes. After stereological corrections, the deviations on spot positions were estimated as  $\pm$  50% of the beam diameter.

## CHAPTER III

### 2D MAGNETOMETRIC MODELING OF A BASIC-INTERMEDIATE INTRUSION GEOMETRY: GEOPHYSICAL AND GEOLOGICAL APPROACHES APPLIED TO THE LIMEIRA INTRUSION, PARANÁ MAGMATIC PROVINCE (SP, BRAZIL)

*Lino, L.M.; Cavallaro, F.A.; Vlach, S.R.F.; Coelho, D.C.*

Article published by the Brazilian Journal of Geology

(DOI: 10.1590/2317-4889201820180099)

#### ABSTRACT

The Limeira Intrusion is an occurrence related to the Mesozoic continental flood basalts of Paraná Magmatic Province, cropping out at the eastern São Paulo state. It is made up of basic-intermediate rocks with a great diversity of structures, textures, and modal compositions, related to specific evolutionary process in a magma chamber. Previous geological and stratigraphic evidence suggests it has a lopolithic-like geometry rather than a conventional sill-like, assumed for most regional similar occurrences. 2D forward modeling of magnetometric data, based on available aerial and newly obtained ground data integrated with in situ rock magnetic susceptibility measurements, were used to test such hypothesis. The results, even considering intrinsic drawbacks of magnetometric theoretical models, are compatible with the geologic-based presumed intrusion geometry. The determination of intrusive bodies geometry is quite significant to explain their different emplacement mechanisms. In the case of Limeira intrusion, the results suggest that the emplacement mechanism may occur, apparently, by inner-accretion of fresh magmatic pulses in its central region. Importantly, the magmatic evolution of lopolith-like basic-intermediate intrusions may open the way for extensive differentiation processes, with strong implications to petrology and metallogenesis.

**Keywords:** Limeira Intrusion, Intrusion geometry, 2D magnetometric modeling, Lopolith, Paraná Magmatic Province

### III.1. INTRODUCTION

The formation and geometry of igneous intrusions in the crust are still a subject of debate in the literature due to the diverse forms of occurrence and to a great amount of tectonic environments in which they occur. However, recently the formation and growth of igneous intrusions have been associated to the amalgamation of several tabular-like intrusions (Menand, 2011). The simplicity, larger distribution and relatively small volumes as compared with batholiths, turn tabular intrusions an object of preferential study when dealing with igneous bodies' emplacement and thermal evolution.

Geophysical modeling is an important tool, which allows defining the geometry of several geologic occurrences. The magnetometric method, despite being a relatively more complex potential one, is a very efficient technique in the detection of geological occurrences with high magnetic susceptibility contrast in relation to their environments (e.g., Kearey & Brooks, 2002).

The magnetization intensity of a rock strongly depends on the modal volume and magnetic characteristics of its minerals. For instance, magnetic anomalies produced by a 200 m<sup>3</sup> body can be the same as those produced by a 2 km<sup>3</sup> body, depending on its overall magnetic mineral content, while gravity anomalies are just related to density. This difference may lead to misinterpretation when dealing with magnetic anomalies; however, there are ways to circumvent this problem, based on well-designed previous geological models and the knowledge of the targets magnetic properties.

The continental crust presents internal stratification associated with variations of the constituting rocks physical properties, as so far indicated by geophysical data and theoretical models based on indirect observations. As well known, the crust is constituted, at least, by two main layers, a deep one composed of mafic rocks (lower crust), and a shallow one of granitic composition (upper crust) (e.g., Rudnick & Fountain, 1995). This type of stratification could not be explained by considering only the emplacement of vertical intrusions. In fact, available seismic data reveal the occurrence of intrusive complexes made up of tabular intrusions at the base of the continental crust, which could be likely mechanisms for the formation of different crustal layers (Franke, 1992).

The present work aims to provide geological and geophysical information about the geometry of Limeira Intrusion, a tabular-like occurrence related to the Mesozoic Paraná Magmatic Province (PMP), in southern Brazil. Although the province has been extensively studied concerning its stratigraphy, petrography, elemental and isotope geochemistry, and geochronology (e.g., Bellieni *et al.*, 1984a; Ernesto & Pacca, 1988; Piccirillo & Melfi, 1988;

Peate, 1997; Gallagher and Hawkesworth, 1994; Nardy *et al.*, 2003, and references therein), which allowed to draw several petrogenetic and tectonic models (e.g., Peate *et al.*, 1992; Turner & Hawkesworth, 1995; Peate & Hawkesworth, 1996; Peate, 1997), there is still few detailed geological and stratigraphic research emphasizing the physical and geometric aspects of individual intrusions or lava flows.

Previous semi-detail geophysical studies by Seixas *et al.* (2015) showed that the Limeira Intrusion has a more limited lateral spreading than previously considered. In addition, previous geological studies give some support for a lopolithic-like intrusion form (e.g., Lino, 2015). Herein we present results obtained through a more detailed ground magnetometric survey, coupled with geological and rock magnetic susceptibility data.

### III.2. GEOLOGICAL FRAMEWORK

The Paraná Magmatic Province (PMP), southern Brazil, represents the most important Mesozoic continental flood basalt expression, constituting the Serra Geral Formation, one of the uppermost formations of the Paraná Basin (Bryan & Ernst 2008; Milani 2004). Over 562.000 km<sup>3</sup> of lavas (Frank *et al.* 2009) were erupted in a time span between *ca.* 133 and 119 Ma (Brückmann *et al.* 2014).

The majority of lavas are tholeiitic basalts, associated with minor andesites, riodacites and rhyolites, these later representing only *ca.* 3% of the lava flows and occurring mainly in the southern Paraná Basin area (Comin-Chiaramonti *et al.* 1988; Nardy *et al.* 2002). These lava flows comprise low-Ti geochemical types, which crop out in the base, while high-Ti varieties appear at the intermediate and the uppermost levels of lava sequences (Peate *et al.* 1992).

The origin of the PMP is certainly related to the opening of the South Atlantic Ocean, through the process of lithospheric mantle melting under the influence of the Tristan da Cunha Plume (Peate *et al.* 1990; Hawkesworth *et al.* 1992; Turner & Hawkesworth 1995; Peate *et al.* 1999; Marques *et al.* 1999) or, alternatively, to heat accumulation under the Pangea Supercontinent (Hartmann 2014).

In the eastern area of the São Paulo State, the high-Ti PMP magmatism is characterized by tabular-shaped intrusions, such as dikes, sills, and laccoliths (Zalán *et al.* 1986). Most dikes intrude basement rocks and form expressive dike swarms (Peate *et al.* 1992) while the emplacement of sub-horizontal tabular intrusions occurs mainly in sedimentary host discontinuities; estimated total thickness of such intrusions vary in general between 2 to 200 m but may reach up to 1,000 m (Marques & Ernesto 2004).

### III.2.1. Limeira Intrusion

The Limeira intrusion is one among several PMP intrusions that crop out in the São Paulo State central-eastern area (**Figure 5**). It intrudes Permo-Carboniferous sedimentary rocks, mainly sandstones and rhythmic siltstones, of the Itararé Subgroup (Faria 2008, Lino 2015). The best fresh-rock expositions are found in the so-called *Cavinatto*, owner's family name, and *Basalto 4* quarries. Soares (1985) was the first to recognize a huge intrusion at this region, named as the Limeira-Cosmópolis Sill. According to them, it would correspond to a tabular shaped intrusion, with almost 60 km of horizontal extension and 280 m of thickness, as suggested from surface evidence and available drill holes.

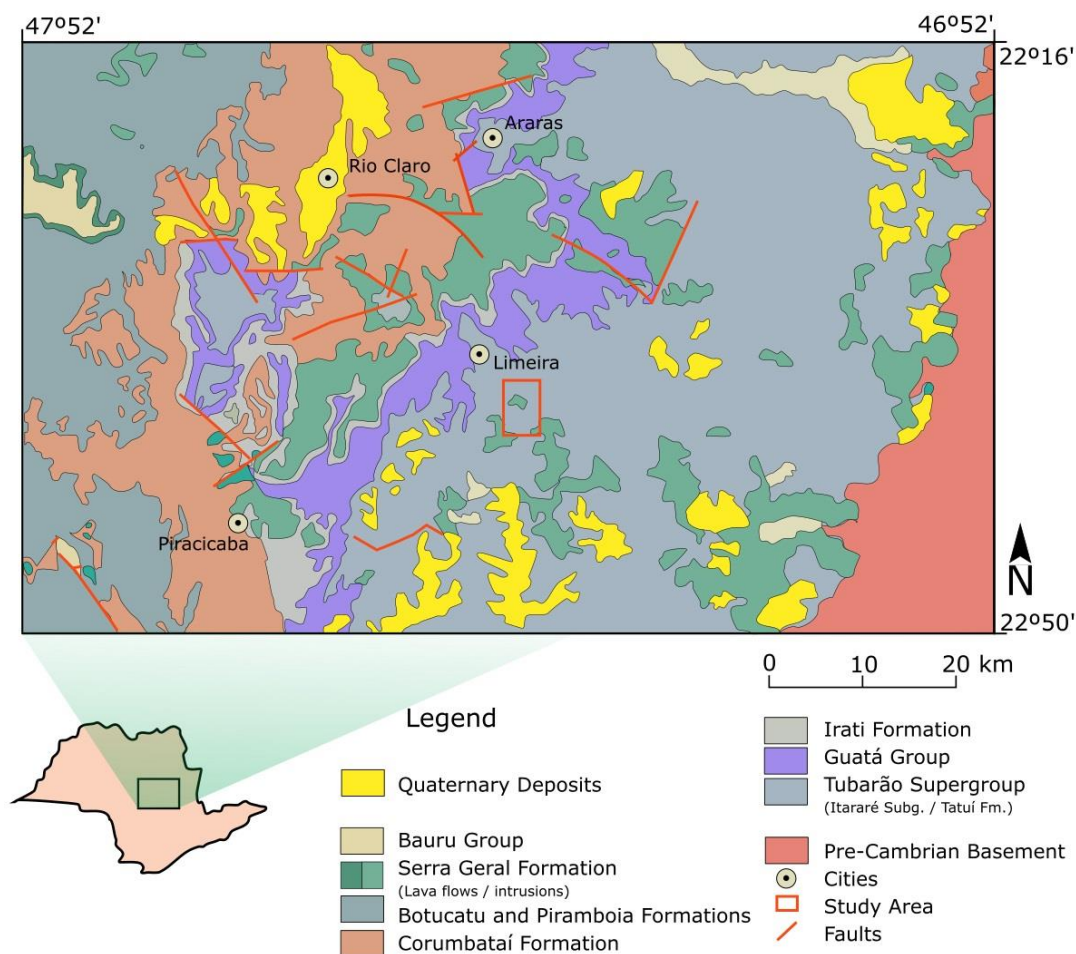


**Figure 5:** Geological Map of central-eastern São Paulo state (Brazil), showing Paraná Basin stratigraphic Units, the pre-Cambrian basement, and location of the study area. Rocks of the Tubarão Supergroup (Itararé Subgroup) constitute most of the country rocks for the intrusions related to PMP magmatism. Simplified from Perrota & Salvador (2005).

Several recent works, emphasizing petrological, geochemical, stratigraphical and geophysical aspects, were conducted by Faria (2008), Oliveira & Dantas (2008), Lino (2015) and Seixas *et al.* (2015) among others, and highlighted some features relatively uncommon to other intrusion analogs. One of us, SRFV, had pointed out the occurrence of typical stratiform-

like rocks at the medium- to deep-outcrops at the Cavinatto quarry, given by modal and textural centimetric- to decimetric-thick igneous layering.

The Limeira rock types include since aphanitic basalts and diabases, at the intrusion borders, coarse-grained monzodioritic to very coarse-grained quartz-monzodioritic rocks, inwards. Rhyolites/rhyodacites occur as late dikes, with mm- to cm-sized thickness, cutting across monzodiorites and diabases and as cm-sized ocelli in the upper diabases.

The main rocks are composed of plagioclase ( $An_{65-30}$ ), clinopyroxene (augite and pigeonite), Fe-Ti oxides (ilmenite, magnetite), and some sulfides. Apatite is the main accessory mineral. Well-developed granophyric intergrowths, composed by alkali-feldspar and quartz, are typical in the coarse-grained rocks mesostasis, amounting up to 23 % vol. Hydrothermal processes are evidenced by apophyllite-bearing late veins, interstitial low-temperature minerals precipitation, and substitution reactions affecting the primary mineral phases (Faria 2008; Lino 2015).

Both Faria (2008) and Oliveira & Dantas (2008) noted the intrusion's bottom edge exposed at the Basalto 4 quarry site and proposed that it becomes thinner to the southeast. Based on ground magnetometric survey and analytical signal amplitude profiles, Seixas *et al.* (2015) suggest that there are two independent intrusions in the Limeira area rather than a single sill: the first corresponds to the Limeira Intrusion itself, while the second (exposed at the Sertãozinho quarry) is another intrusion located in the southern area of Limeira city.

## III.2. RESULTS AND DISCUSSION

### III.2.1. The geologic suggested model

The Cavinatto quarry presents the best exposition of the Limeira Intrusion, currently exposing a vertical section with *ca.* 110 m deep in its southern and *ca.* 90m in the northern sides. The intrusion has a sub-horizontal roof, which becomes stepped towards the NW area. The exposed basic-intermediate rocks show a great diversity of structures, textures, and modal compositions. The most typical types may be grouped in aphanitic basalts, diabases, monzodiorites, and quartz-monzodiorites. Petrographic and geochemical details of the main rock types, as well as chemical compositions of the rock-forming minerals details, can be found in Faria (2008) and Lino (2015). A brief general characterization is presented in the following.

The aphanitic varieties (1.0-1.3 m thick) probably accompany all intrusion contours. They are made of massive thin chilled margins in contact with thermally metamorphosed sedimentary rocks, and aphanitic basic rocks, which may show some hydrothermal alteration due to interaction with the H<sub>2</sub>O-bearing host rocks. As granulation increases progressively

inwards, the rock became a diabase, with a phaneritic texture and structures that change from amygdaloidal to massive inwards. The later crops out from *ca.* 1.3 m to *ca.* 20 m deep.

Clinopyroxene monzodiorites occur from *ca.* 20 m to 60 m deep; their contacts with the overlying diabases are usually sharp. They are very heterogeneous coarse-grained rocks, sometimes with a “jaguar-skin” aspect given by the irregular distribution of the mafic and felsic minerals. Felsic pods do contain typical granophyric intergrowths. Granulation increases downwards while the mafic content decreases.

Clinopyroxene quartz-monzodiorites occur from *ca.* 60 m to 90 m deep; they are heterogeneous coarse- to very coarse-grained rocks with a cm-sized thin prismatic crystal of pyroxene, and well developed - sometimes platy - magnetite crystals, which imprints a grid-like texture over a similar “jaguar-skin” aspect. Their contacts with the monzodiorites appear to be gradational.

To the deepest levels exposed within the quarry, rock granulation decreases and compositions become again monzodioritic. These rocks are the ones characterized by rhythmic relatively mafic- and felsic-rich layers with subhorizontal dips. Importantly, they occur only on the eastern and southern quarry walls.

The average SM values obtained for these rocks are presented in **Table 3**. The basic-intermediate rocks present an average value about  $44.5 \times 10^{-3}$  (SI), while the sedimentary host rocks show, as expected, a much lower one, about  $0.219 \times 10^{-3}$  (SI). Among the formers, the aphanitic basalts, the monzodiorites, and the quartz-monzodiorites present also very contrasted averages values (from 80 to  $\sim 45$  and  $25 \times 10^{-3}$  SI, respectively), in accordance with their Ti-magnetite/magnetite modal contents.

**Table 2:** Magnetic susceptibility ( $\times 10^{-3}$  SI) and average modal composition of opaque phases (mainly Ti-magnetite/magnetite and ilmenite) within the measured samples representative of the main rock types exposed in the Limeira Intrusion.

Rock type	Chilled Margin	Diabase	Monzodiorite (uppermost)	Monzodiorite (lowermost)	Quartz-Monzodiorite	Host Rocks
Average Susceptibility (SI $\times 10^{-3}$ )	80	65	50	38	25	0.219
%Modal of opaque phases	20	15	7.5	8	6	$\sim 0$

The following field observations suggest a lopolith- rather than sill- or laccolith-like intrusion geometry as presented in **Figure 6** (see also [Lino, 2015](#)):

1. part of northern contact with the enclosing siltstones is sub-vertical down to, at least 30-40 m deep, as revealed by prospecting drill holes in country rocks;
2. structural emplacement evidence observed along the intrusion suggest it thins towards the northwest, east, and southeast;
3. the exposed layered sequences did not present the expected lateral distribution. They appear to constitute more or less concentric, localized, layers.

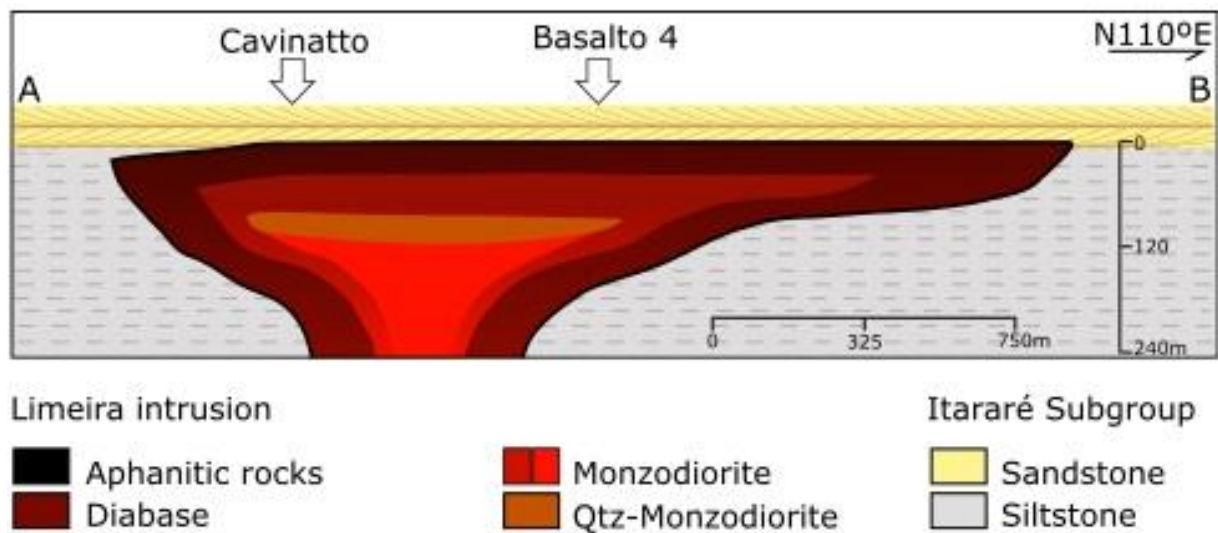


**Figure 6:** Schematic (N110E) geological cross section through Limeira intrusion, showing the distribution of the main rock-types, and the localization of the quarries. The figure illustrates the geometry of the intrusion based on the interpretation of field observations.

### III.2.2. Geophysical analysis

Geophysical results are presented as magnetic anomaly maps for ground and aerial surveys, and the final 2D forward modeling, as follows.

#### III.2.2.1. Magnetic anomaly maps

The total magnetic anomaly maps are presented in **Figure 7**. They show similar positive and negative anomalies, as expected for targets located at this magnetic latitude - with predominant induced magnetization - pointing to a dipole over the Cavinatto and Basalto 4 quarries, which defines the probable horizontal occurrence of the intrusion. The main observed differences between the ground- and aerial-based maps are the dipole layout, reflecting contrasted data acquisition systematics, and the anomalies intensities, which result from distinct vertical distances between the measurements and the target in each case.

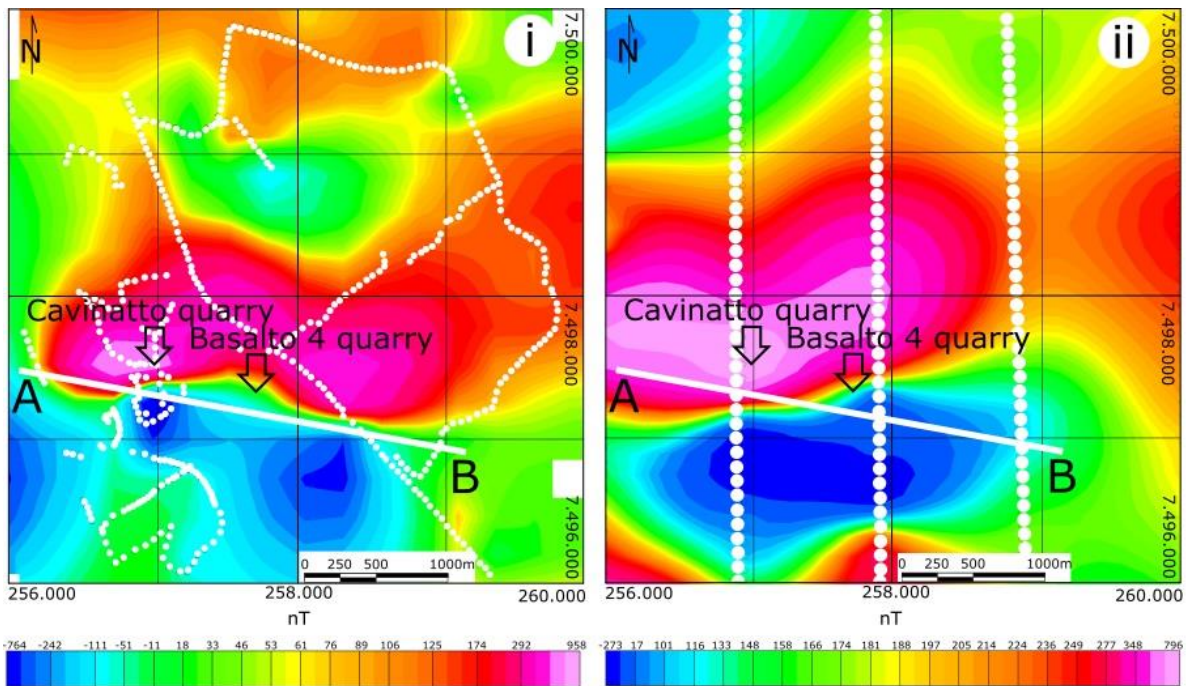


**Figure 7:** Total anomalous magnetic field (nT) maps for the Limeira Intrusion based on our ground survey (i) and the available aerial data (ii). The locations of the Cavinatto and Basalto 4 quarries and the AB suggested geologic cross section (Figure 6) are indicated. Note the dipolar anomaly centered over the quarries in both maps and the difference range between the anomalous field intensities.

The derived analytical signal amplitude (ASA) maps are depicted in **Figure 8**. Of note, its application is valid in our case, with a favorable ratio between top depth (~20 m, based on field observations) and the expected width of Limeira intrusion (>1,000 m, based on quarries location). So the use of both ground- and aerial-based maps, with different data distribution, allows to better delimit the possible limits of the intrusion. The terrestrial data presents better resolution and maximum ASA values twice as high as the aerial data due to the target proximity; on the other hand, the aerial data is cleaner from possible anthropic interferences. Their combination allows suggesting the intrusion limits quite well on the basis of the maximum signal, as depicted in **Figure 8**.

The RTP obtained maps (**Figure 9**) depict anomaly geometric features and their peak distributions, which are again similar in the ground- and aerial-based maps. In fact, they give the same response: two main high anomalies, aligned with the Cavinatto - Basalto 4 quarries tie line and a relative low anomaly between them. These lower values reflect, most probably, the lack of data over the area in both surveys.

In both cases, the positive anomaly is restricted to the most probable intrusion location. High anomaly variation gradients are observed close to the northern intrusion limits while relatively low gradients appear towards the southern limits. At first principles, the former

suggests a high dipping contact while the latter suggests a gradual lateral variation of the intrusion thickness.

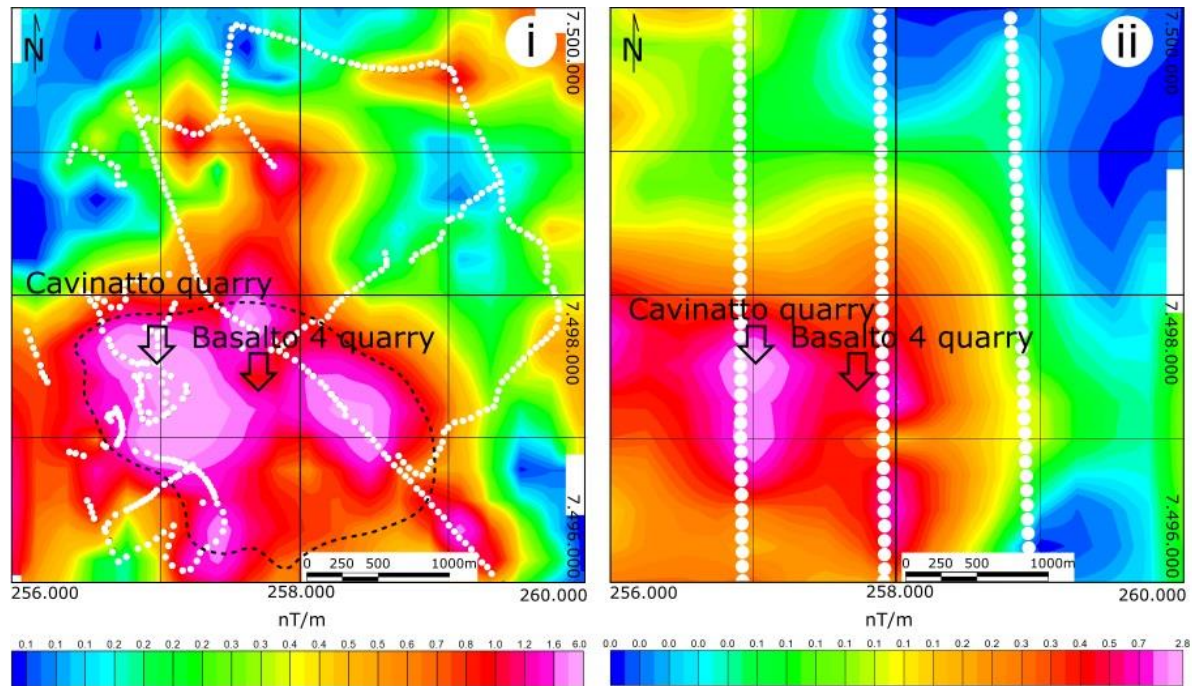


**Figure 8:** Analytical Signal Amplitude (ASA, nT/m) maps for the Limeira Intrusion, based on MAF data of ground survey (i) and the available aerial data (ii). Note that the ground data highlights two main regions with high ASA values, while aerial data (more defocused) presents an additional high ASA to southern, related the raw data acquisition contrasted features (white dots). The black dotted line in (i) is our best-estimated intrusion limits based on both maps.

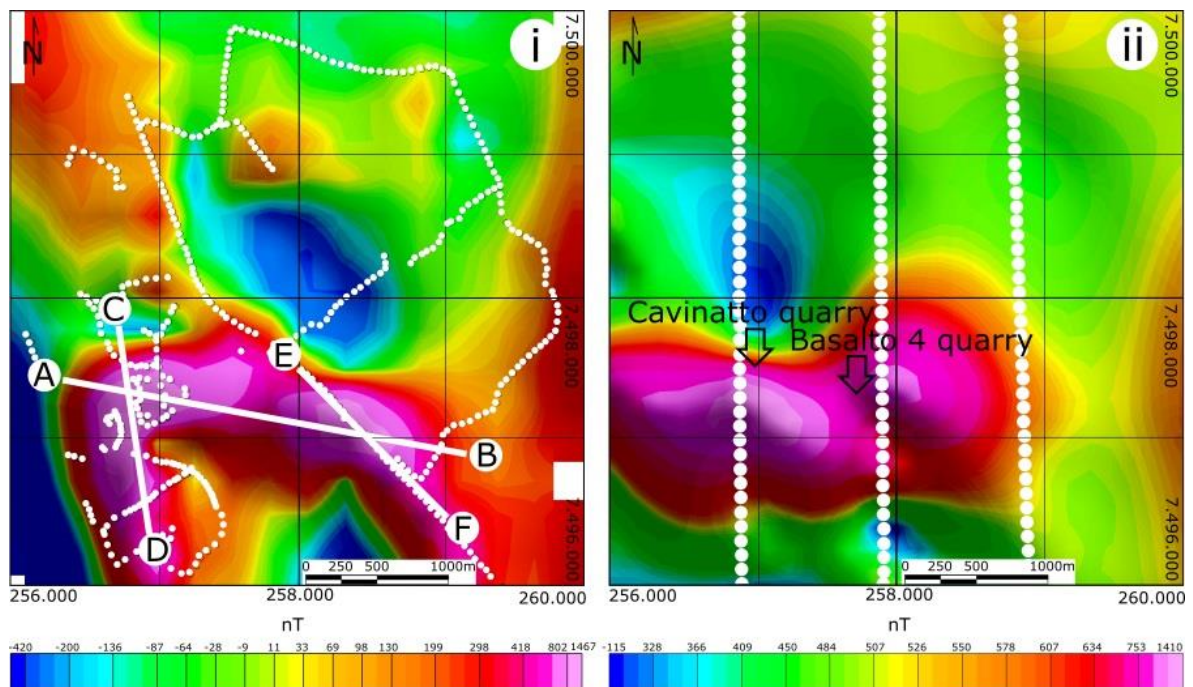


**Figure 9:** Reduced to Pole (RTP, in nT) maps for the Limeira intrusion, based on MAF to ground survey (i) and available aerial data (ii). Note the high anomaly over the quarries. The AB, CD and EF profiles correspond to total anomaly sections, extracted for the two-dimensional modeling. White dots represent the localization of data acquisition.

### ***III.2.2.2. Magnetometric forward modeling***

The RTP values derived from the ground survey were used to estimate the 2D intrusion geometry along the three main profiles shown in **Figure 9**. For simplicity and easiness of data treatment, this model considers an average value for the magnetic susceptibility [ $44.5 (10^{-3} \text{ SI})$ ], which appears to not affect substantially the overall model. The AB profile runs along the unique geological section available, while the CD and EF profiles run along the regions with most ground magnetometric measurements.

The presented geophysical model considers that the top depth approaches 20 m thickness, as estimated from measurements in some locations next to Cavinatto quarry. Results are depicted in **Figure 10**, which presents, among the 2D theoretical possible models, the total anomaly model that best fits with our geological data, along these profiles. In fact, as drawn in Figure 8, calculated and observed total magnetic anomalies match very well; minor discrepancies, especially in the central zone of the A-B profile, are probably related to the lack of ground measurement stations, leading to less accurate interpolation. The differences between the observed and calculated anomalies, at the beginning and end of the CD and EF profiles, most probably, result from border effects.

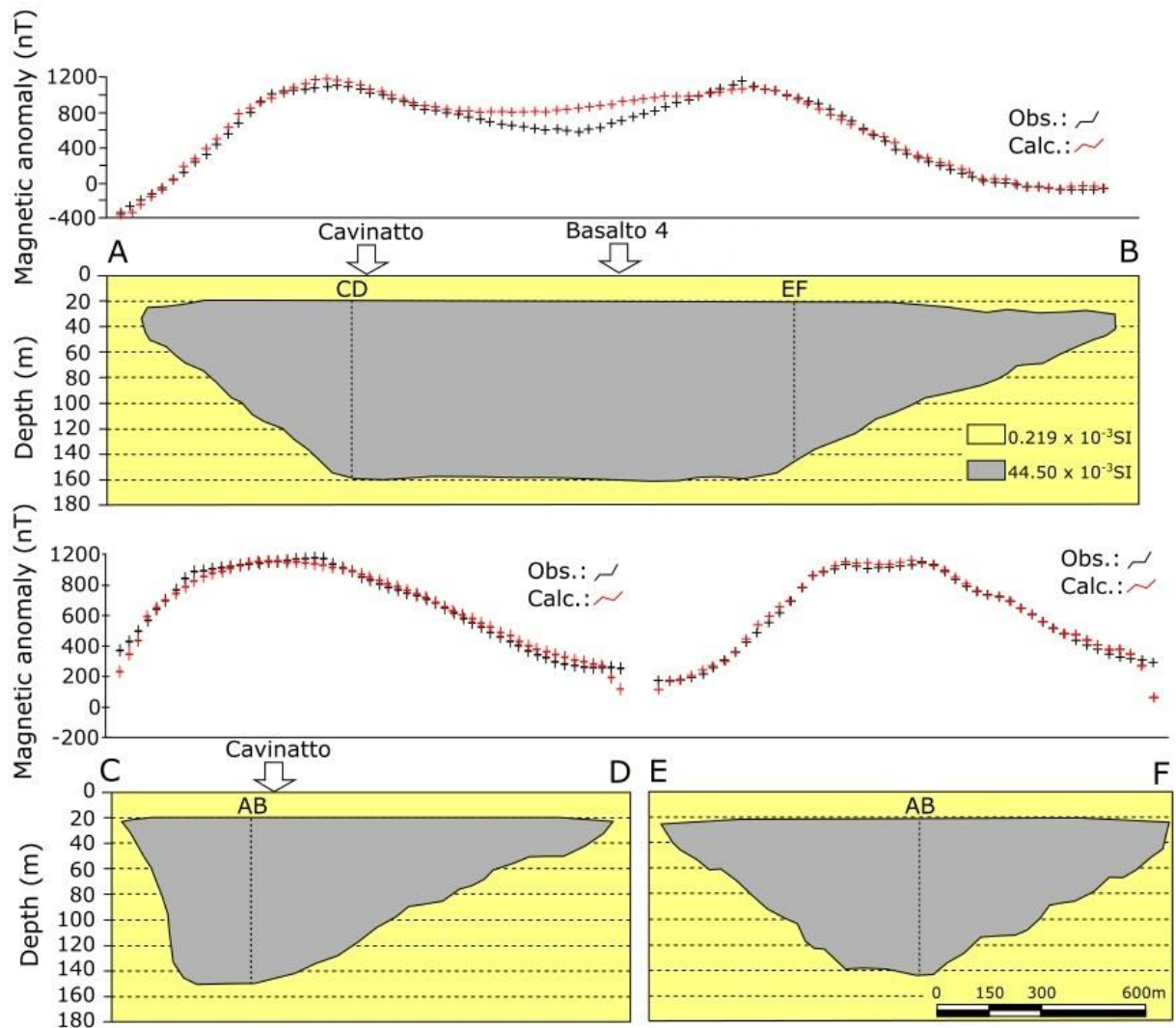


**Figure 10:** Schematic two-dimensional magnetic model of Limeira intrusion, based on the presumed geologic model, total magnetic anomalies (at AB, CD and EF profiles) and magnetic average susceptibility measurements. See text for discussion.

### III.3. CONCLUDING REMARKS

The integration of ground and aerial magnetic data, geological information and magnetic susceptibility measurements in rocks allowed set out an improved interpretation of the lateral distribution and the 2D geometry of the Limeira Intrusion. Our results suggest that the intrusion has an elliptical shape, occupying a top area of about 2.5 to 3.0 km<sup>2</sup> and its thickest zone corresponds to the quarries north portions. The modeled two-dimensional magnetometric profiles support a lopolithic-like intrusion geometry very well, as previously suggested from geologic evidence.

The model has some intrinsic limitations, however, and the main drawback comes from field station distribution, which affects interpolation processes, as some relatively large areas were not sampled due to exposure problems in relation to the location of the AB profile. On the

other hand, the removal of the sedimentary cover, allowing direct rock exposure, increases magnetic anomalies, while the removal of rocky material - as in the extreme case of the Cavinatto quarry - decreases the total volume of ferromagnetic minerals and, thus, the magnetic signal intensity. These later effects cannot be properly quantified and corrected up to now and may lead to some misinterpretation.

The analysis of the two-dimensional profiles allows inferring some emplacement mechanisms for the Limeira intrusion. The profiles AB and EF suggest that the intrusion evolved, most probably, through progressively emplacement of fresh magmatic pulses in the central zone of the magmatic chamber, causing its growth by the mechanism of inner-accretion (*e.g.*, [Menand, 2011](#)). The north region coincides with the thicker zone of the intrusion and supports the hypothesis that this may be the recharge area of the intrusion.

The geometry and volume of the Limeira Intrusion opened ways for the development of several specific magmatic (*e.g.*, magmatic recharge and differentiation) and post-magmatic (*e.g.*, hydrothermal alteration) processes, turning it an interesting target for detailed petrological and metallogenetic studies.

**CHAPTER IV**  
**QUANTITATIVE TEXTURAL ANALYSIS AND Sr-ISOTOPY IN PLAGIOCLASE**  
**APPLYING TO REVEAL EMPLACEMENT MECHANISM AND THERMAL**  
**EVOLUTION OF LIMEIRA INTRUSION, PARANÁ MAGMATIC PROVINCE,**  
**BRASIL**

*Lino, L.M.; Vlach, S.R.F.*

**ABSTRACT**

The stratigraphic analysis of compositional and textural variations, coupled with the structural and geometric features of an intrusive body related to Paraná Magmatic Province, allowed the interpretation of its emplacement mechanism and thermal evolution. Quantitative textural analysis through crystal size distribution (CSD) of plagioclase crystals, the spatial distribution pattern of structures, microtextures, granulation, and rock-types, evidenced the internal heterogeneities of this occurrence. In this paper, an approximately 110 m exposure section top-to-floor of Limeira intrusion (Brazil – SP) reveals that its internal heterogeneity was caused by non-instantaneous successive emplacement of three different magma injections. The textural analysis also reveals fine-grained crystals formed under different cooling paths, present in medium- to coarse-grained rocks within the intrusion, next to sharp contacts between different rock compositions. These contacts are characterized by hybridization textures and are marked by large amounts of plumose granophyre-type and plumose plagioclase. The time lapse between consecutive pulses is responsible for a stepwise cooling-path, characterized by very contrasting effective residence-times at each layer, preservation of hybridization textures, and the development of almost rigid surfaces providing crystals alignment and clustering during magma flow. The isotopic and textural data demonstrates a complex assembly history, in which the obtained split-size between mixed plagioclase populations at the Hybrid-Zones coincides with the onset of Sr-isotope ratio increase, possibly involving filter pressing of residual liquids. We also recognize pre-existent ante-crystals before magma installation only in coarse-grained rocks, probably formed in a different magma chamber. The recognition of successive magma injections separated by a long period is a very important issue. It supports the models of tabular intrusion emplacement, formed by the amalgamation of sheet-like magma batches, and can be the response for the distribution of different compositions and textures within Limeira intrusion.

**Keywords:** crystal size distribution (CSD); spatial distribution patterns (SDP); emplacement model; Limeira intrusion; Paraná Magmatic Province.

## IV.1. INTRODUCTION

The formation and growth of igneous bodies exert considerable influence on the geometry and the processes of the earth's crust creation. For a long time, it was believed that igneous intrusions, especially of granitic composition, were formed by instantaneous events, through the inflation of a single or a few magma pulses. Recently, a great diversity of models have been created to explain the assembly, framework, and thermal evolution of several igneous bodies (Annen & Sparks, 2002; Michaud & Jaupart, 2006; Matzel *et al.*, 2006; Menand, 2008; Annen, 2011; Kavanagh *et al.*, 2017). Based on laboratory models, geophysical, geochronological, and geological evidence is currently known that small to large intrusions might be formed by the amalgamation of several magma pulses, probably with sheet-like geometries such as sills (Hawkes & Hawkes, 1933; Cruden, 1998; Coleman *et al.*, 2004; Glazner *et al.*, 2004; Horsman *et al.*, 2005; Miller *et al.*, 2011).

Quantitative textural analysis (i.e. Crystal Size Distribution - CSD) in igneous rocks aims to quantify crystals grain-size distribution, as well as its geometric arrangement, and helps to recover the evolutionary magmatic paths, principally to describe and quantify the acting mechanisms during its emplacement. As demonstrated by Zieg & Marsh (2002), in a steady-state system, the development of textures is marked by a progressive and predicted increase in grain-size within an intrusive tabular-like body. However, the spatial arrangement of crystals is not the result of simple crystallization. Crystal clustering and shape preferred orientation might result of more complex mechanisms, as replenishments events, resulting in internal magma flows, and recycling of early crystal clusters (i.e. Mock *et al.*, 2003; Jerram *et al.*, 2003; Zieg & Marsh, 2012). Furthermore, *in situ* isotopic ratios provide a well constrain of magmatic processes and evolution; and coupled with CSD analysis can result in time-lines of isotopic-ratio evolution (Morgan *et al.*, 2007).

In this work, we present a detailed, and stratigraphically constrained, quantitative textural analysis of plagioclase crystals, the spatial distribution patterns (SDP) of these crystals, *in situ*  $^{87}\text{Sr}/^{86}\text{Sr}$  isotopic analysis, and a CSD-based thermal evolution model. We present geological and textural aspects relatively uncommon in similar recent studies, aiming to demonstrate the importance of the cooling path and the time interval between consecutive pulses of magma, acting directly on the style of formation, growth, and geometry of magma chambers. Based on quantitative methods we present an emplacement model, which has important implications for the magmatic evolution and heat dynamics, especially for basic-intermediate tabular intrusions.

## IV.2. GEOLOGICAL SETTING

The Limeira intrusion is a basic-intermediate occurrence related to Mesozoic flood-basalts of Paraná Magmatic Province (PMP). It is one among several tabular-shaped bodies emplaced on permocarboniferous sedimentary rocks of Itararé Subgroup, Tubarão Supergroup (**Figure 11**), which crops out in the northeast portion of São Paulo state, southeastern Brazil. These rocks are part of the Paraná Basin, a large intracratonic sedimentary basin located in the south-central region of South-American continent, covering an area about 1,500,000 Km<sup>2</sup>. Its evolutionary late-stage processes are related to a distensive environment, responsible to the generation of the PMP flood basalts and the opening of Atlantic Ocean (Turner *et al.*, 1994; Marques & Ernesto, 2004; Ernesto *et al.* 2002, Milani, *et al.* 1992; Milani, 2004).

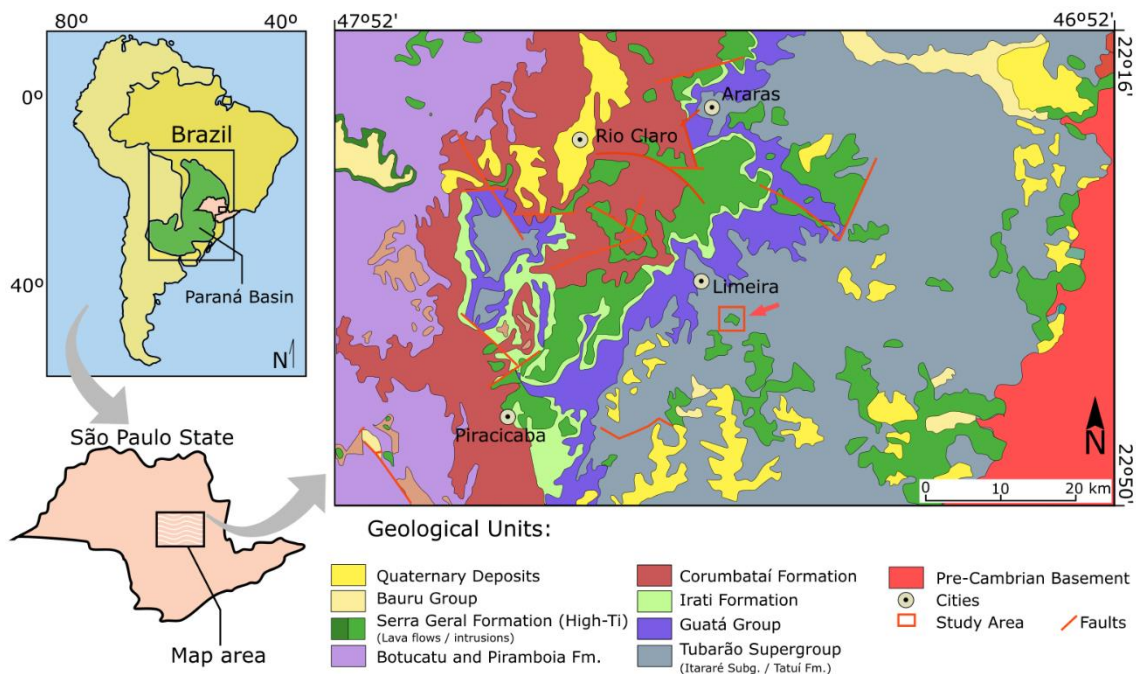


**Figure 11:** Simplified geological map of the central-east portion of São Paulo state in southeastern Brazil, depicting the main geological units and the location of the Limeira Intrusion (Modified from Perrota & Salvador, 2005).

### IV.2.1. Paraná Magmatic Province

The PMP is one of the major continental basaltic manifestations of the world, formed by lava flows (ca. 450,000 km<sup>3</sup>) and intrusive occurrences (ca. 112,000 km<sup>3</sup>), which yielded ca. 600,000 km<sup>3</sup> of total volume. This province covers about 75% of the surface of the Paraná Basin, in an area of approximately 917,000 km<sup>2</sup> (Frank *et al.*, 2009; Piccirillo *et al.*, 1988a). Classical and more recent precise Ar<sup>40</sup>/Ar<sup>39</sup> data argue that the vast majority of lava-flows were formed in a short time interval, varying from 1 to 3 Ma – between 134-131 Ma (Ernesto *et al.*, 1999; Thiede & Vasconcelos, 2010).

The origin of such a vast magmatic province has long been related to lithospheric mantle melting, under the influence of the Tristan da Cunha Plume (Peate *et al.*, 1990,1999; Hawkesworth *et al.* 1992; Tuner & Hawkesworth, 1995; Marques *et al.* 1999; Ernesto *et al.* 2002), or alternatively to the heat accumulation that occurred under the Pangea Supercontinent (Hartmann, 2014). Lava flows are mostly of the *pahoehoe* type (Waichel *et al.*, 2006), and tholeiitic basalts are dominate, corresponding up to 90% in volume. Silicic rocks are majority rhyodacites and rhyolites that crop out in the upper flow piles, mainly at the central and southern province areas. The tholeiitic magmatism has long been subdivided into two main groups: low-Ti ( $\leq 2$  wt.% Ti) lava flows crop out at the base of the pile in the southern province areas, while high-Ti ( $> 2$  wt.% Ti) varieties made up the intermediate and top lava flows, towards the north (e.g., Peate *et al.*,1990).

The main intrusive bodies related to PMP constitute expressive dike-swarms, mainly along the South America and African coasts, while sills and laccoliths, as part of the high-Ti magmatism, are more frequent at eastern area of São Paulo state (Zalán *et al.*, 1986). The estimated thickness of such intrusions can range between 2 and 200m in general and can reach up to 1,000m in localities near to the depocenter of Paraná Basin (Marques & Ernesto, 2004). Most dike swarms intrude rocks from the crystalline basement, while tabular-like concordant intrusions emplaced at major discontinuities of the sedimentary pile (Peate *et al.*, 1992).

#### **IV.1.2. Limeira Intrusion**

The Limeira intrusion was emplaced within sandstones and rhythmic siltstones of the Itararé Subgroup (Permo-Carboniferous) and exhibits a great variety of rocks-types. Fresh rocks are exposed at Cavinatto and Basalto 4 quarries, where the first site exhibits the most complete rock exposure, given by a complete section from its upper contact until a depth of 110 meters (Lino *et al.*, 2018). These exposures allows to examine atypical features rarely seen in other analogous intrusions in other analogous intrusions, such as (1) the preservation of structural relationship with host-rocks at the uppermost contact, (2) expanded compositional variation, including since basaltic to rhyolitic rocks, as well as a significant late hydrothermal input, and (3) a significant variety of magmatic structures and textures.

Given these characteristics, it becomes an excellent target for the study of emplacement mechanisms and related magmatic processes in tabular-like intrusions. The intrusion was formerly being considered as a classical sill example (e.g., Soares, 1985; Faria, 2008). However, recent detailed geological, petrographic and ground-/aerial-magnetometric data indicate that it conforms better a lopolith-like intrusion, probably formed by a number of individualized

magma pulses (Lino *et al.*, 2018). These authors also draw attention to its compositional, structural and textural variability inwards, pointing in evidence a more complex magmatic evolutionary model. Geochemical and the Sr- and Nd-isotope data (Oliveira & Dantas, 2008; Faria, 2008) had suggested that the intrusion evolved through fractional crystallization from a basaltic primitive magma within a closed system, with some possible contamination from the sedimentary host rocks.

### IV.3. GEOLOGY AND STRATIGRAPHY

#### IV.3.1. Host rocks and structural aspects

A virtually complete section of the Limeira intrusion crops out at the Cavinatto and Basalto 4 quarries, providing well exposures of different levels of the intrusive body. At the uppermost contact with the host rocks, fractures and ductile faults formed during the placement stage may be mapped to disclose information about its three-dimensional shape and its assembly process. The Limeira intrusion is emplaced within sandstones and rhythmic sediments of the Itararé Subgroup, which represent glaciogenic deposits. The sandstones presents cross-bedding stratification of metric dimensions (**Figure 12a**), with interbedded layers of minor clay minerals, occurring above the rhythmic siltstones and resulting in almost horizontal and flat contact. Rhythmic siltstones are constituted of millimetric layers of fine-grained sands and silt, which occurs in shades of grey (**Figure 12b**), and its sub-horizontal stratification is parallel to the contact with sandstones.

The upper contact of the intrusion is almost concordant with sandstones, relatively flat, horizontal and follows the former sedimentary contacts between sandstones and siltstones. Conjugate fractures and faults systems suggest that solely the siltstones have been significantly deformed during the intrusion emplacement. The NW-contact of the intrusion has an average direction of  $293.3^{\circ}/50.2^{\circ}$ , and conjugated faults occur with  $113.4^{\circ}/40^{\circ}$ , resulting in horsts- and grabens-like structures, which should have to accommodate the deformation introduced by the intrusive mechanism (**Figure 12c**). The strong relationship between these features is highlighted in the stereological representation, presented in **Figure 12c**.

At the northwest region of Cavinatto quarry, a high-angle fault oriented east-west and dipping  $85^{\circ}$ , displaces the sedimentary contact about 10-15 meters. A mafic dike with 6 meters thickness and 10 meters height fills in the fault plane and is interpreted as the main feeder zone of Limeira intrusion (**Figure 12d**). By comparing the dike and structures at this region, argued that the main stress-field were sub-orthogonal to the faults orientation during the early stages of the emplacement process. It can also indicate a change in local-stress induced by the

sedimentary discontinuity, capable to redirect the propagation direction of its feeder dike, resulting in the magma infilling within this horizontal structure.

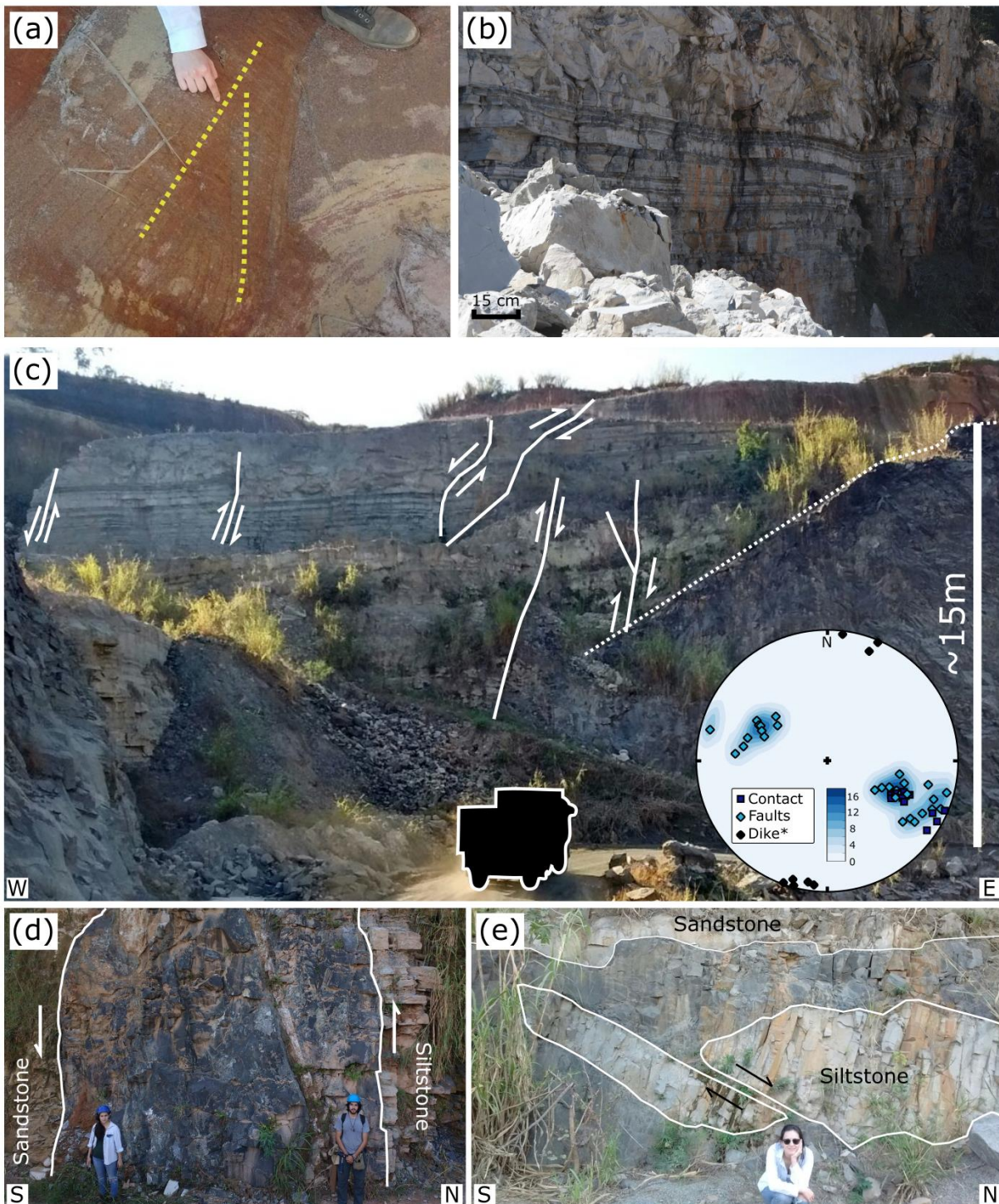


**Figure 12:** Geological and structural features of the Limeira Intrusion at the Cavinatto quarry. a) Overlying cross-bedding sandstone at the northern limit the intrusion. b) Laminar plan-parallel stratification in overlying rhythmic siltstone. c) Emplacement-related faults cutting across rhythmic siltstone at the northern upper contact (dotted line) and stereographic projections of the main mapped structures. d) Basic feeder-dike emplaced in subvertical fault, affecting sandstone and siltstone host-rocks. e) Siltstone xenoliths showing domino-fault displacement close to the upper contact, somewhat irregular but almost horizontal.

Xenoliths of host-rocks are a less frequent feature on the upper-most part of the intrusion and made mainly of siltstone varieties. These xenoliths have centimetric to metric dimensions and are tabular-shaped; occurring horizontally displayed and locally presenting displacement of domino-type faults, along with the N-S direction (**Figure 12e**). The geometry and orientation of the displaced xenoliths are suggestive of an engulfing process during magma installation, in a scenario of horizontal magma flux from north to south.

The heating process at the upper contact generated a ca. 1 m thick metamorphic halo and the development of hornfels rocks. Previous petrographic analysis of siltite-hornfels suggests that the metamorphic process does not efficiently affect the principal mineral phases. The interaction with H<sub>2</sub>O-bearing host rocks is responsible for micro-fracturing, and the generation of quartz- and chlorite-rich veins and fluid-inclusions traces in quartz grains (**Figure 13a**). It also apparently results in the crystallization of up to 0.1 mm sized andalusite pseudomorphs, occurring only within millimetric clay-rich layers as rectangular-shaped sericitic agglomerates (**Figure 13b**).

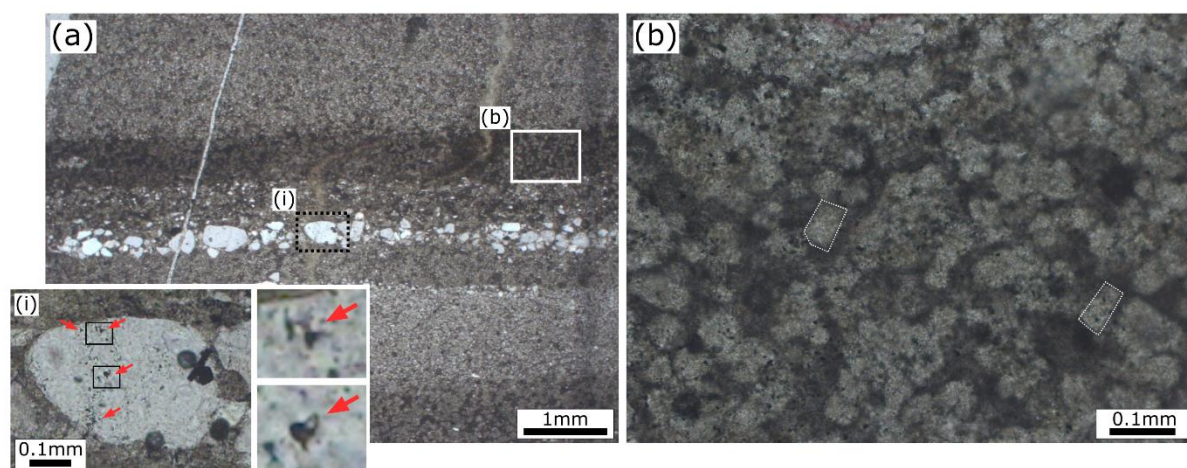


**Figure 13:** Thin section of rhythmic siltite hornfels, present in the northwest contact of Limeira intrusion. a) General view exhibiting layers of different granulation. It is possible to observe the presence of a fine-grained sand, and distinctive types of venulations filled by quartz and/or chlorite with the possible hydrothermal origin, perpendicular to sedimentary stratification. The detail depicts quartz grains that contain fluid inclusions related to one of these veins. b) The detail in an argillic layer, where it is possible to observe tabular features, probably resulting in andalusite micro-crystals substitution.

### IV.3.2. Petrographic facies

The mapped basic-intermediate rocks in the Limeira Intrusion were grouped according to petrographic facies (*e.g.*, Ulbrich *et al.*, 2001), characterized by their modal contents (**Figure 14**), textures and structures, as well as their stratigraphic position within the intrusion, as presented in the following. The distribution pattern of the different rock compositions results into three main groups. These groups represent rocks from the Upper Border Zone (UB), Intermediate zones – subdivided in an Upper Intermediate Zone (UIZ) and a Lower

Intermediate Zone (LIZ) - as well as the Central Zone (CZ), respectively (**Figure 14**). Accordingly, with rock structures and textures, five petrofacies were recognized from the intrusion borders towards the center. They include massive types, “jaguar-skin” types with medium- to coarse-granulation, layered types, layered-like types imprinted over a grid-like texture, and grid-like facies.

The UB comprehends micro-gabbro-types ( $An_{60-42}$ ), and for simplicity represent the massive facies, also including the basalts from the chilled margins and amygdaloidal/ocellar micro-gabbroic (diabase) rocks. Rocks from each internal zones were classified as follows: (1) clinopyroxene quartz-monzodiorites ( $An_{50-30}$ ) with high-silica content from UIZ; (2) clinopyroxene granodiorite-types ( $An_{40-33}$ ) from CZ; and (3) clinopyroxene quartz-monzodiorite ( $An_{45-27}$ ) with low-silica content and clinopyroxene quartz-diorite ( $An_{48-38}$ ), from LIZ. In general, the recorded modal variations are compatible with evolutionary trends common to the medium-K calcic-alkaline rocks (Lameyre & Bowden, 1982).

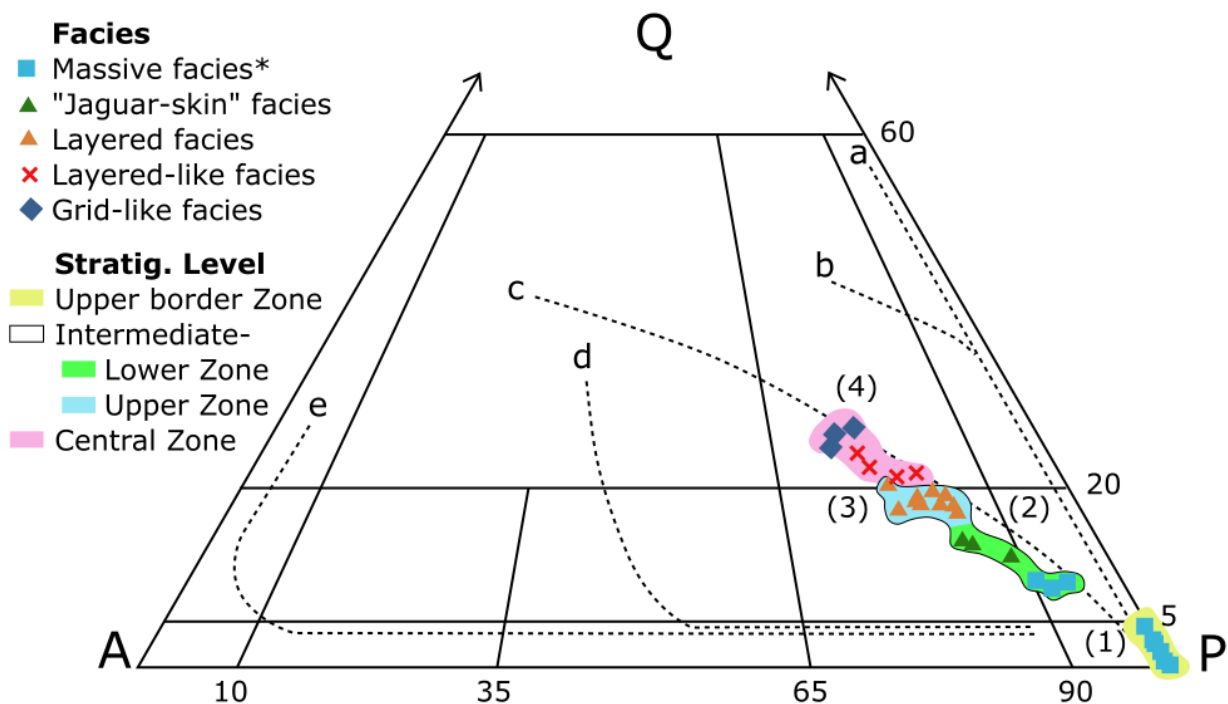


**Figure 14:** QAP modal diagram for the classification of igneous rocks (Strekeisen, 1976), showing the modal diversity within the Limeira Intrusion. Fields: (1): gabbro/diorite, (2) quartz gabbro/diorite, (3) quartz monzogabbro/monzodiorite, (4): granodiorite. Letters a, b, c, d, and e identify typical trends of the tholeiitic, calc-alkaline tonalitic/trondhjemite, calc-alkaline granodioritic, monzonitic and alkaline plutonic rock series, respectively, as defined by Lameyre & Bowden (1982). Note that basic-intermediate rocks of the Limeira Intrusion conform to the average trend of calc-alkaline granodioritic series. The marked increase in quartz and alkali-feldspar contents are compatible with variations in the stratigraphic level, as well as the distribution of the recognized petrographic facies.

Resultant modal compositions and associated errors are presented in **Table 3**, considering the final classification presented in **Figure 14**.

**Table 3:** Modal composition of the Limeira intrusion representative samples and estimated errors.

Sample	Gabbro-types						Quartz-Diorite		
	IC-09 (2)	IC-09 (9)	IC-08	IC-08b	IC-05	IC-07	TF-09	TF-05	IC-02a
<b>Plagioclase</b>	47.10 (2.47)	53.95 (2.60)	51.47 (2.89)	52.20 (1.95)	56.70 (2.73)	57.77 (2.77)	44.12 (2.13)	59.77 (2.82)	48.20 (2.56)
<b>Clinopyroxene</b>	20.20 (1.39)	23.57 (1.42)	20.19 (1.38)	23.08 (1.43)	19.75 (1.35)	16.14 (1.29)	18.74 (1.26)	15.59 (1.37)	24.70 (1.13)
<b>Opagues</b>	14.60 (1.19)	13.23 (0.83)	18.94 (0.77)	14.15 (0.79)	11.50 (0.97)	6.95 (0.73)	11.07 (0.94)	5.75 (0.74)	9.70 (1.07)
<b>Granophyre</b>	-	-	-	-	-	-	9.42 (1.11)	7.10 (0.66)	7.60 (0.89)
<b>Chlorite*</b>	12.90 (0.79)	7.13 (0.95)	6.90 (0.88)	6.46 (1.13)	10.45 (0.85)	12.79 (0.76)	13.16 (1.33)	6.05 (0.77)	5.00 (0.69)
<b>Apatite</b>	3.60 (1.16)	1.58 (0.94)	1.45 (1.04)	1.79 (0.45)	1.35 (0.33)	2.15 (0.46)	1.79 (0.68)	1.60 (0.43)	1.70 (0.36)
<b>Ampibole</b>	-	-	0.10 (0.10)	1.10 (0.55)	0.20 (0.15)	1.15 (0.26)	0.70 (0.51)	0.55 (0.39)	1.50 (0.44)
<b>Quartz</b>	1.60 (0.56)	0.54 (0.45)	0.95 (0.79)	1.24 (0.85)	0.05 (0.05)	3.05 (0.55)	1.00 (0.45)	3.60 (0.72)	1.60 (0.52)
<b>QAP</b>	48.70	54.49	52.42	53.44	56.75	60.82	54.54	70.47	57.40
<b>Q/(QAP)</b>	0.033	0.009	0.018	0.023	0.001	0.050	0.018	0.051	0.028
<b>M</b>	38.40	38.38	40.68	38.78	32.80	26.39	32.30	23.49	37.60

**Table 3 - Continuation:** Modal composition of the Limeira intrusion representative samples and estimated errors.

Sample	Granodiorite-types							Quartz-Monzodiorite		
	TF-36	TF-32	TF-30a	IC-06	IC-06b	IC-04a	IC-04c	TF-13	TF-19	TF-02
<b>Plagioclase</b>	40.10 (3.32)	37.29 (2.42)	37.50 (2.33)	39.98 (1.89)	33.88 (3.21)	37.03 (2.50)	38.91 (2.73)	43.13 (3.32)	42.99 (3.27)	54.03 (4.32)
<b>Clinopyroxene</b>	12.35 (1.13)	18.16 (1.54)	14.75 (1.42)	14.24 (1.07)	12.79 (2.11)	13.37 (2.16)	13.12 (1.55)	19.04 (1.79)	13.20 (2.12)	13.99 (2.24)
<b>Opagues</b>	5.87 (0.75)	6.09 (2.39)	7.55 (0.89)	7.85 (1.13)	6.85 (1.66)	4.99 (1.07)	9.13 (2.12)	7.15 (1.43)	7.32 (1.32)	9.02 (1.65)
<b>Granophyre</b>	23.24 (2.21)	17.91 (2.36)	21.40 (1.86)	16.24 (1.92)	23.69 (3.31)	26.25 (2.93)	23.38 (2.30)	13.49 (2.22)	15.05 (1.95)	12.16 (1.69)
<b>Chlorite*</b>	3.59 (1.34)	12.18 (1.97)	10.15 (0.94)	11.69 (1.80)	11.89 (2.05)	10.98 (1.79)	4.66 (1.96)	9.05 (2.34)	12.16 (2.57)	4.05 (1.19)
<b>Apatite</b>	2.89 (0.66)	2.08 (0.49)	2.65 (0.53)	2.35 (0.47)	2.35 (0.55)	1.80 (0.66)	2.66 (0.49)	2.10 (0.79)	5.05 (1.23)	2.13 (0.67)
<b>Ampibole</b>	3.24 (1.11)	1.93 (0.72)	1.85 (0.88)	1.80 (0.16)	3.15 (1.77)	0.80 (0.55)	2.66 (1.03)	4.20 (1.30)	2.58 (1.09)	1.52 (0.72)
<b>Quartz</b>	8.71 (1.12)	4.36 (1.74)	4.15 (1.15)	5.85 (0.83)	5.40 (1.06)	4.79 (1.45)	5.46 (1.02)	1.85 (0.76)	1.65 (0.53)	3.09 (0.84)
<b>QAP</b>	72.05	59.56	63.05	62.07	62.97	68.07	67.75	58.47	59.69	69.28
<b>Q/(QAP)</b>	0.121	0.073	0.066	0.094	0.086	0.070	0.080	0.031	0.027	0.044
<b>M</b>	24.35	28.26	26.80	26.24	25.14	20.96	27.57	32.49	28.15	26.66

**Table 3 - Continuation:** Modal composition of the Limeira intrusion representative samples and estimated errors.

Sample	Qtz-Monzodiorite									
	IC-07b	LIM-10	IC-04b	IC-01	IC-01b	TF-30b	TF-23	TF-17	TF-15	LIM-02
<b>Plagioclase</b>	44.36 (2.06)	43.67 (3.53)	42.33 (3.21)	45.33 (3.05)	40.70 (2.97)	40.60 (2.77)	41.01 (2.79)	40.22 (2.69)	41.16 (2.83)	40.95 (3.11)
<b>Clinopyroxene</b>	17.88 (2.45)	17.37 (2.32)	16.07 (2.47)	17.79 (1.98)	18.70 (2.65)	19.30 (2.73)	16.44 (1.79)	15.45 (2.44)	12.82 (2.11)	16.45 (1.89)
<b>Opaques</b>	10.49 (2.79)	6.15 (1.54)	10.40 (1.62)	6.30 (1.77)	8.20 (2.11)	7.70 (1.83)	5.63 (1.41)	7.87 (1.68)	9.73 (2.38)	8.10 (2.18)
<b>Granophyre</b>	14.99 (2.05)	16.08 (2.13)	16.13 (1.59)	14.59 (2.95)	13.20 (1.68)	18.20 (1.77)	19.18 (1.44)	20.66 (3.11)	21.05 (2.89)	17.55 (1.88)
<b>Chlorite*</b>	3.10 (1.56)	5.86 (2.34)	5.53 (1.67)	6.00 (1.84)	9.40 (2.75)	6.30 (1.86)	9.97 (2.43)	6.97 (1.81)	6.64 (1.74)	6.45 (1.65)
<b>Apatite</b>	1.40 (0.79)	1.64 (0.56)	2.13 (0.76)	1.35 (0.49)	1.40 (0.67)	2.90 (1.07)	2.14 (0.81)	4.06 (1.77)	2.34 (0.65)	1.35 (0.74)
<b>Ampibole</b>	2.20 (0.87)	3.67 (1.12)	3.67 (1.56)	4.20 (1.88)	3.80 (1.54)	1.75 (0.69)	2.64 (1.11)	0.95 (0.75)	4.58 (1.79)	5.25 (2.23)
<b>Quartz</b>	5.59 (1.53)	5.56 (1.24)	3.73 (1.38)	4.45 (1.27)	4.60 (2.08)	3.25 (1.05)	2.99 (1.35)	3.81 (1.66)	1.68 (0.77)	3.90 (2.11)
<b>QAP</b>	64.94	65.31	62.19	64.27	58.50	62.05	63.18	64.69	63.89	62.40
<b>Q/(QAP)</b>	0.086	0.085	0.054	0.069	0.078	0.052	0.047	0.058	0.026	0.062
<b>M</b>	31.97	28.83	32.27	29.64	32.10	31.65	26.85	28.43	29.47	31.15

### IV.3.3. Internal stratigraphy

Currently, the best exposures of Limeira intrusion occurs in Cavinatto quarry, where it exhibits a section of almost 110 meters at its southern portion and 90 meters at the northwest region. Its internal stratigraphy is marked by an inwards increase in rock granulation and silica content (principally marked by a granophyric mesostasis increasing), as well as diversification of textures and structures. The distribution of rock-types within Limeira intrusion occurs almost as concentric layers, and the variations within this intrusion are summarized in **Figure 15**.

The Upper Border Zone (UB) comprises micro-gabbroic rocks with a systematic inwards increase of plagioclase and opaque minerals, and a decrease of clinopyroxene, quartz and apatite content. The UB margins are made of massive rocks, constituted by aphanitic to very fine-grained diabase 1.0-1.5 meters thick, and its chilled margins probably occur along the entire outline of the intrusion. The uppermost contact of the diabase with the aphanitic rocks, down to 5m deep, is characterized by the occurrence of amygdaloidal and ocelli structures, the latter made up by rhyolitic/rhyodacitic fine-grained rocks. These gabbroic rocks crop out from ~1.5 to 20-23 meters deep, showing a progressive increase in rock granulation inwards.

The Intermediate Zone (IZ) comprehends medium- to coarse-grained clinopyroxene quartz-monzodiorite types, as well as medium-grained clinopyroxene quartz-diorite at the lower portion. Due to the observed stratigraphic distribution, the intermediate zone includes an Upper

(Upper Intermediate Zone - UIZ) and a Lower layer (Lower Intermediate Zone – LIZ, including the Feeder Zone – FZ, at the bottom). The contacts of rocks from IZ with surrounding UB and CZ are usually sharp and marked by the presence of plumose-like plagioclase crystal habits, they also present a remarkable increase in granophyre content and granulation, sometimes associated with the concentration of felsic or mafic minerals.

The UIZ comprises heterogeneous quartz monzodiorite-types, presenting a “jaguar-skin” aspect at its uppermost part, due to an irregular distribution of mafic minerals close to the contact, and occurring with heterogeneous distributions of felsic- and mafic-pods towards the central region. This zone extends from ca. 20 meters to ca. 60 meters deep and the main compositional variations inwards include: (1) the progressive decrease in plagioclase, clinopyroxene and opaque minerals content and (2) modal increase of granophyre mesostasis. At its bottom region, rocks are crosscut by aplitic-like veins with rhyolitic/rhyodacitic compositions, frequently in diffuse contacts with host-rocks. Close to its bottom contact, the frequency of plumose-like granophyre-type increases.

The Central Zone (CZ) is composed of clinopyroxene granodiorite varieties, in abrupt contact with the UIZ rocks. The uppermost region of granodiorite is constituted by very coarse-grained rocks, with typical “grid-like” structures, imprinted by long cm-sized prismatic crystals of clinopyroxene as well as acicular ilmenite and magnetite. They represent rock types with relatively minor amounts of plagioclase, clinopyroxene, and apatite contents, and contain K-feldspar-quartz granophyre intergrowths reaching up to ~23% in volume in their mesostasis. Radiating-fringe and cuneiform-types are most frequent granophyre-types in these rocks. Rocks that made up the lowermost part of the CZ, and the LIZ uppermost region, are characterized by typical “layered-like” and layered structures respectively, in a gradational contact to each other. Very heterogeneous granodiorites-types compose the CZ lowest layer, presenting horizontal lenticular-shaped pods with abundant mafic minerals, which results in the “layered-like” structure imprinted over the grid-like structure.

The LIZ rocks occur in a gradual contact with granodiorite rocks from CZ, and the main compositional variations downwards include: (1) progressive increase in plagioclase, clinopyroxene, apatite, and opaque minerals content and (2) decrease of granophyre volume. At the bottom of LIZ, the transition to the clinopyroxene quartz-diorite that compounds the FZ is apparently gradational, and both rock-types present the same “jaguar-skin” aspect. At this transition zone, the plumose granophyre type increases its frequency. A noticeable textural variation can be observed in **Figure 15**, which is represented by distinct increases in plumose granophyre-types on quartz-monzodiorite and quartz-diorite at the bottom of each rock-type

layer. At the Feeder Zone (FZ) of the intrusion, a remarkable magmatic flux structure is oriented almost vertically. These rocks-types represents a restricted area in the lowermost part of the outcrop, in a gradational structural and compositional contact with quartz-monzodiorites.

Important textural features are present at the contact between the main stratigraphic zones; these are represented by plumose plagioclase crystals habits, plumose- and radial-fringe granophyre-types are more frequent, and the presence of a “quenched” mesostasis. Acicular plagioclase-, clinopyroxene-, and opaque-crystals compose the very fine-grained mesostasis, which includes a probably second generation of fine-grained and well-formed plagioclase crystals. These regions are also marked by the presence of elongated clinopyroxene megacrysts and suggest a drastic change in cooling paths during the final stages of crystallization. Due to the hybridization of textures, characterized especially by plagioclase crystals with three different habits and formed under contrasted cooling-rates, these regions of interaction are classified as Hybrid Zones.

The crystallization final stages of the main rock-types also includes the formation of ocelli structures in the uppermost gabbro, as well as millimetric to centimetric-sized rhyolites and rhyodacites late veins and dikes. These late dikes are present since the LIZ, cutting all rocks on the intrusion until reaching the gabbro-types present at the UB. Apophyllite and interstitial low-temperature minerals (i.e. calcite, quartz, titanite, and zeolites) are evidence of a very important hydrothermal process, related to these late liquids and resulting in amygdaloidal structures. Post-magmatic substitution reactions are evidenced by chlorite associated with clay minerals, iron oxides, albite, and quartz, affecting all the primary mineral phases. The frequency of mineral substitution is greater in the regions of rock contacts, such as seen by the chlorite modal abundance in **Figure 15**.

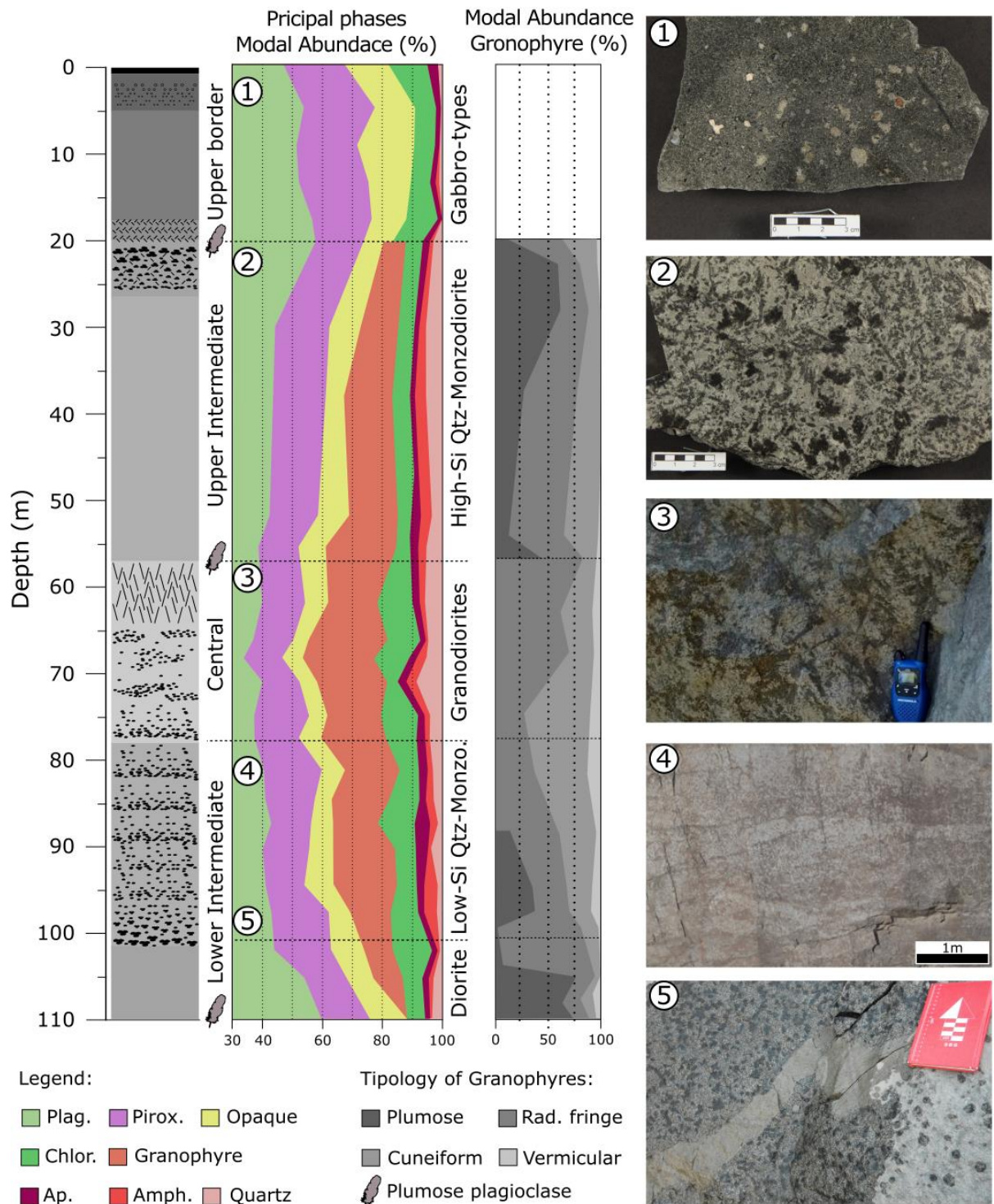


**Figure 15:** Schematic stratigraphic columns, illustrating the mapped textural, structural, and compositional variations within the Limeira Intrusion. Depth zero corresponds to the horizontal contact with sandstones at the upper contact. The main structural and textural features, the modal content of the main and accessory minerals and of granophyre types are highlighted in the first, second and third columns, respectively. Numbers in the second column identify the location of the rock slabs/outcrops whose digital images are shown in the right. (1) Amygdule- and ocelli-bearing diabase, close to the contact with the intrusion chilled border. (2) “Jaguar-skin”-type quartz-monzodiorite from Upper Intermediate Zone. (3) Grid-type granodiorite from the uppermost region of the Central Zone. (4) Layered series detail showing Cross-bedded modal layering marked by angular unconformities from the Bottom Intermediate Zone. (5) “Jaguar-skin”-type quartz-monzodiorite from Lower Intermediate Zone, intruded by an aplitic dike.

#### **IV.4. QUANTITATIVE TEXTURAL ANALYSIS**

Before proceeding with the quantitative textural analysis, we carried out statistical tests for examining crystal size measured distributions to (1) validate the logarithmic behavior of crystal sizes and (2) to detect mixing between contrasted plagioclase populations. Crystal shapes were determined to characterize their variability within the intrusion and to perform the needed stereological corrections. The obtained CSD files are listed in **Appendix C**.

##### **IV.4.1. Statistical analysis of crystal-size populations**

As suggested by our petrographic analysis, the petrographic facies from hybrid zones may contain more than one plagioclase crystal-size family. As predicted by the CSD theory, crystal sizes must present a lognormal distribution with a high frequency of small units, and if mixed populations do exist, the same grain-size distribution law should be valid for any population. The separation of different populations may be not a simple task however, and is detected only through significant inflections in CSD lines ([Higgins, 1996](#)). To test for population mixing hypothesis, statistical analyses were done considering plagioclase crystals major axis in all samples, supported by the expected logarithmic distribution.

Statistical analysis involved the representation of the crystal's long-axes values in histograms, coupled to its cumulative distribution function (CDF). Samples of the hybrid zones present small inflections in the probability curves and small discrepancies when compared to a lognormal model with the same mean and standard deviation. However, the results were not capable to distinguish different populations. As a graphical test, the histograms were plotted with x-axes on a logarithmic scale, which resulted in "normal-like" distributions, excepting in the hybrid zones (**Figure 16**).

The logarithmic scale of the x-axis was able to avoid the superposition of the small-sized crystals in the two families of grains. In addition, it allowed the determination of a "split-size" (grain size, L) between contrasting grain-size families. This step is extremely important to the calculation of CSD regression lines when different populations are present. Consequently, the statistical analysis can highlight the presence of different families - on cases with almost straight CSD resultant curves -, also revealing more complex cases, such as the TF-36 sample distribution (**Figure 16b**).

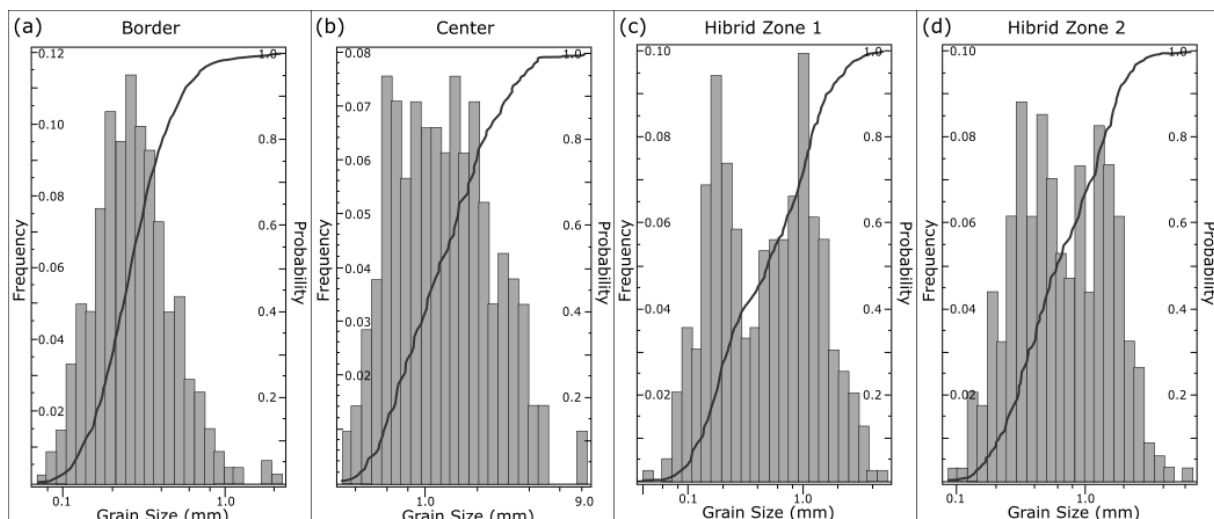


**Figure 16:** Histograms showing the plagioclase long-axis dimensions distributions and the corresponding cumulative density functions (CDF) for selected samples from the Limeira Intrusion. Grain size frequencies for samples collected in the UBZ (Sample IC-08) and CZ (Sample TF-36) homogeneous zones with close to log-normal distributions (a and b). Figures c and d are from the Hybrid zones 1 e 2 (samples IC-07a and IC-04c, respectively). Note the bimodal distribution and inflections on the CDF curves, best developed in the Hybrid zone 1, pointing out to two plagioclase crystal size families.

#### IV.4.2. Stratigraphic variations of plagioclase crystal-shape and modal abundance

The determination of crystal shape, in three-dimensional perspective, is very important for CSD stereological calculation, since it aims to transform a 2-D raw data into 3-D crystal size. Based on non-parametric calculations, [Higgins \(2000\)](#) developed a method to stereological conversion to transform 2D crystals sections into real 3D distributions. Crystal habit is also important to characterize textural variations, as well as the “Closure Limit” problem intrinsic to the CSD analysis (see next sections). In this study, plagioclase 3-D shapes were estimated using the CSDslice spreadsheet, developed by [Morgan & Jerram \(2006\)](#). In general, a unique crystal 3-D habit for samples with different crystal-size families does not affect substantially the stereological corrections in our samples. The tests of axes ratio (L/S) of raw data usually results in very close values for both size-families, with no significant variability.

Crystal habits are defined in terms of the Aspect Ratio (short: intermediate: long axes – S: I: L) and are represented in **Figure 17**, in diagram I/L versus S/L ([Zingg, 1935](#)). Generally, from the border to the central region, crystal shape varies roughly from bladed to tabular respectively. As expected, prolate-shaped crystals are typical in the grid-structured granodiorites from CZ. Crystal shape variations can be associated with the increase in residence time from the intrusion edges to its central region, reflecting the tendency of crystals to become tabular. On the other hand, on the grid-like rock types, a different tendency can be observed, as it can be a result of a more complex cooling-path and crystallization history. The great variety

of crystal shape and the rough tendency observed within the intrusion is suggestive of different paths of crystallization, and certainly results of the emplacement process and thermal evolution.

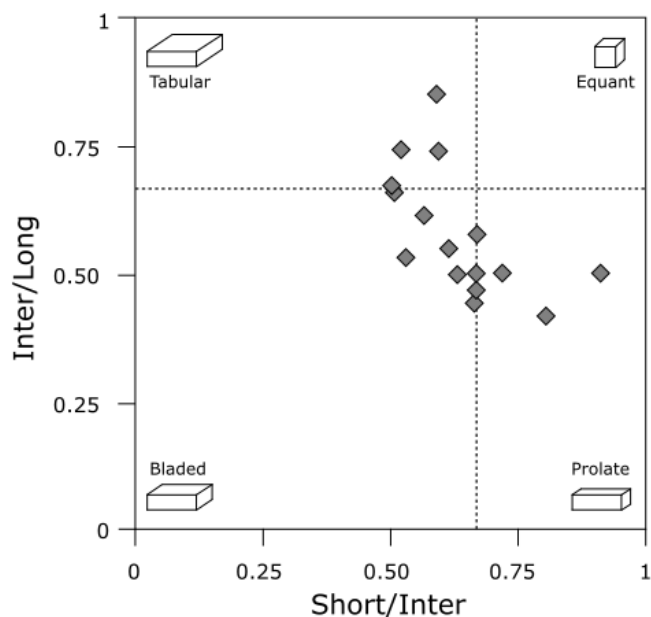


**Figure 17:** Plagioclase crystal morphologies within the Limeira Intrusion, as defined by their intermediate- to long-axis and short- to intermediate-axis relative ratios, according to Zingg (1935). See text for discussion.

The resultant aspect ratio, number of crystals, volumetric proportion of plagioclase, as well as the considered total area for each sample are present in **Table 4**. As observed, the resultant analyzed areas are very contrasting, reflecting the variability of rock-types granulation within Limeira intrusion. We also note that the number of analyzed crystals per volume is less frequent on coarse-grained rocks, probably due to an increase in grain-size and most probably as a consequence of the natural compositional variation.

From the obtained variations of plagioclase crystals habits and modal proportions, is not possible to observe a straight correlation of these parameters with its stratigraphic position. In a closed system, we should expect progressive and almost continuous changes in plagioclase crystal habit, due to a constant evolution of cooling-rates, and a decrease in plagioclase content due to the evolution through fractional crystallization. The observed dispersion, especially at the critical zones of rock contact, can suggest a more complex magmatic mechanism acting during the emplacement and crystallization of Limeira intrusion. In this sense, the resultant internal variability can be related with the magmatic differentiation process in association with perturbations of spatial distribution patterns (SPO), as demonstrated by Higgins (2002). The next sections are addressed to quantify the textural variations stratigraphically and to verify the spatial distribution patterns within this intrusion.

**Table 4:** Results of the analyzed area, number of crystals, volumetric proportions, and aspect ratio (calculated using CSDslice 5). \*Volumetric proportion obtained by point counting.

Sample	Area (mm <sup>2</sup> )	N° of crystals	CSD Vol. (%)	Vol. (%)*	Aspect ratio
IC-09 (2)	11.54	438	46.980	47.100	1:1.5:3.2
TF-05	55.78	484	60.095	59.770	1:1.5:3
IC-08	56.82	339	51.923	51.474	1:2:3
IC-01	158.42	394	44.219	45.237	1:1.8:2.9
IC-09 (7)	134.83	367	53.834	53.947	1:1.9:3.6
IC-07a	308.44	314	57.311	57.771	1:1.5:3.4
IC-07b	328.21	393	44.086	44.356	1:1.5:2.6
LIM-10	386.07	238	44.298	43.672	1:1.7:2
TF-17	615.53	250	40.235	40.221	1:1.6:3.2
IC-04	346.73	219	38.007	37.026	1:1.4:2.8
TF-24	503.66	210	40.405	41.006	1:1.9:2.6
IC-04b	287.60	298	41.589	42.333	1:1.7:2.3
IC-04c	374.31	341	38.558	38.907	1:1.9:3
IC-06	366.59	207	40.171	39.980	1:1.1:2.2
TF-30	773.67	213	36.897	37.500	1:1.3:3
LIM-02	612.23	370	40.730	40.950	1:1.5:3
TF-36	644.68	212	39.290	40.101	1:1.6:2.9

Note: The values of volumetric estimation based on point counting and CSD are very close. Maximum standard deviation results in errors of  $\pm 0.5\%$  (one sigma).

#### IV.4.3. Crystal size distribution

The layout of the different composition and petrographic facies are suggestive of an intensive fractional crystallization process and/or reinjections of successive magma pulses, during the formation of this intrusion. However, it is not simple to split up different magma batches using chemical variations or isotopic compositions. In a system under possible fractional crystallization or replenishment by same-origin melts and possible mixing, the quantitative textural analysis allows measuring some magmatic effects. According to compositional and textural variations, resultant CSD curves for samples of Limeira intrusion are depicted in **Figure 18** and were divided into three main levels: borders, central region, and hybrid zones. Consequently, it is possible to observe a systematic increase of crystal size inwards, with specific variations at rock-contact zones.

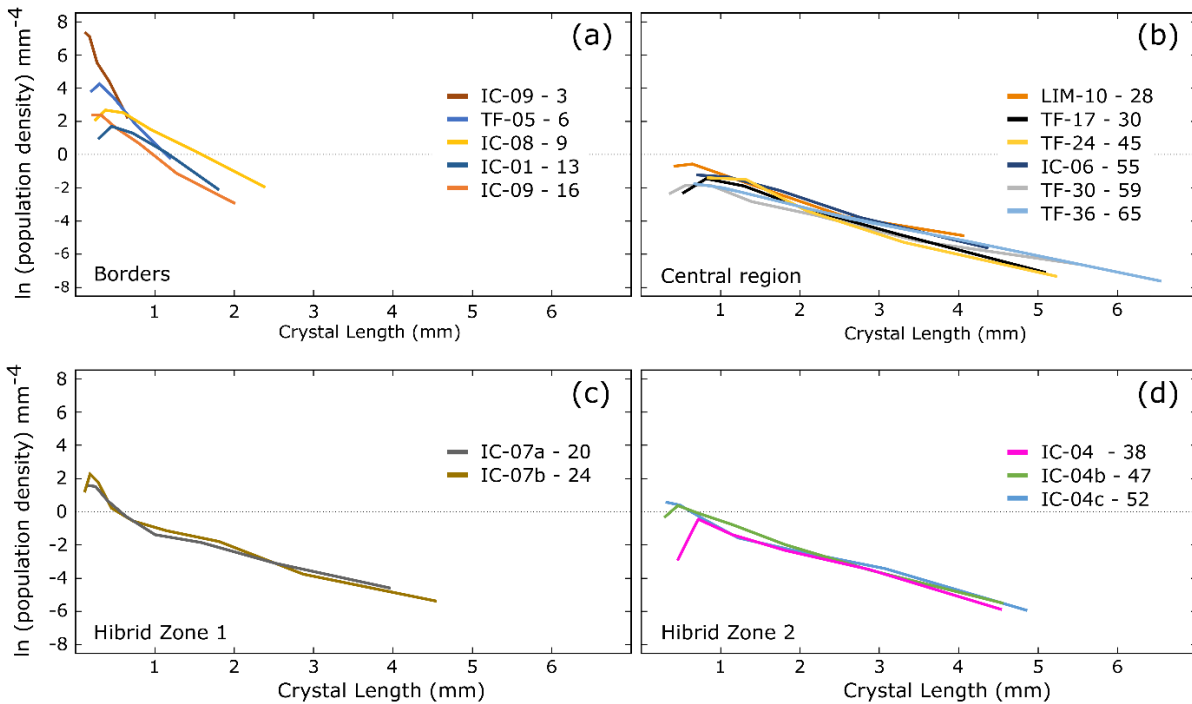


**Figure 18:** CSDs patterns for the analyzed samples from the main zones of the Limeira Intrusion, grouped accordingly with similar features and stratigraphic position. Note that the legend for each sample includes the distance in meters from the nearest contact. a) Lower (quartz diorites) and Upper (gabbros and microgabbros) Border zones showing both grain size and residence time increasing inwards. b) Lower Intermediate, Central and Upper Intermediate Zones (quartz-monzodiorites and granodiorites) CSD plots. Note grain size increasing towards the Central Zone, coupled with a minor residence time increase. c) Hybrid Zone 1, from the upper contact of the Upper Intermediate Zone, showing inflections in CSD curves for crystal sizes less than 1mm. d) Hybrid zone 2, from the lower contact of the Upper Intermediate Zone, showing minor relatively inflections patterns and accentuated convex-humps resulting from relatively smaller crystals in sample IC-04.

Notably, from samples distribution, it was possible to quantify the textural variations within Limeira intrusion. Gabbro-types at the UB and quartz-diorite at the BIZ essentially compose rocks at the borders of intrusion. In **Figure 18a** is possible to observe in almost straight CSD's lines, an increase in rock-granulation inwards as predicted for steady-state systems. Probably it results from a simple stage crystallization and increases in residence time inwards. CSD's of samples located at the borders exhibits a more expressive convex-upwards hump inwards, as a result of crystal "coarsening", a common feature that is probably associated with the decrease in the available melt at late stage crystallization.

Within Limeira intrusion, heterogeneous quartz-monzodiorites and granodiorite rocks constitute the intermediate and central region, respectively. The contact between these two rock-types is often marked by abrupt changes in texture, structure, and composition. However, the CSD's lines are almost coincident in slope and minimum values (**Figure 18b**). Main differences among these CSD's reside in its maximum crystal length values, which increases

into the intrusion's core. Despite less expressive, the process of "coarsening" was also observed in these rocks and associated with a normal plagioclase crystallization process.

The so-called hybrid-zones might represent regions resulted from the extensive filter-pressing process as well as the contact of non-instantaneous magma batches, and comprise two families of plagioclase grain-size at least. The first hybrid zone defines the contact of uppermost gabbro from UB with clinopyroxene quartz-monzodiorite from TIZ. In this zone, it is possible to recognize a huge variation in plagioclase grain-size, and a small inflection in the CSD curves (**Figure 18c**). In the Hybrid zone 1 (HZ1), the CSD's of second crystal population also exhibits a decrease in its slope values inwards, which may be the result of an increase in residence time.

The outcome CSD's of the second hybrid zone resulted in almost straight lines. Supported by statistical analysis, it was only possible to distinguish more than one plagioclase population in one sample (**Figure 18d**). At this region, the samples exhibit a noticeable humpback associated with a small proportion of very fine grain-sized crystals. In addition, the 'homogenization' of crystal families is an important process, due to the increase in residence time inwards. Heat accumulation at the centermost region of Limeira intrusion, as well as the possible time span between magma batches, represent significant processes to grain-size homogenization. The **Figure 18d** depicts the CSD's of HZ2, where it is possible to observe a small inflection close to 0.9-1.0 millimeter grain-size region that may correspond to the "split-size" in **Figure 16**.

The calculation of CSD's lines was performed through the best-regression aspect ratios obtained in CSDslice spreadsheet ([Morgan & Jerram, 2006](#)), and only crystal-size families with 10 or more crystals were considered to CSD curves. Resultant CSD's were then approximated to a regression line, enabling to estimate its final nucleation densities ( $n_0$ ), slope, characteristic length ( $C_i = -1/\text{slope}$ ), and linear regressions coefficients ( $R^2$  – very close to the maximum value), as summarized in **Table 5**. The calculation of regression lines was also performed in samples with evident two crystal-size families, and based on its respective "split-size" values.

**Table 5:** Crystal Size Distribution coefficients obtained on each regression lines. Values of  $n_0$  correspond to final nucleation density (Y-axis interceptions),  $C_i$  is the characteristic length ( $-1/\text{slope}$ ), slope corresponds to the inclination of lines.  $R^2$  is the coefficient of correlation of regression, and L (max) is the maximum crystal length for each sample.

Sample	$n_0$	$C_i$	Slope	$R^2$	L mm (max)
IC-09 (2)	8.3645	0.1037	-9.6420	0.9882	0.65
TF-05	5.7570	0.1973	-5.0667	0.9982	1.20
IC-08	3.7375	0.4218	-2.3708	0.9947	2.39
IC-01	2.7604	0.4217	-2.3714	0.9773	2.87
IC-09 (7)	2.6718	0.4530	-2.2071	0.9919	2.01
IC-07a*	-0.2244	0.9046	-1.1054	0.9958	0.63
IC-07a**	2.3599	0.2413	-4.1432	0.9749	3.97
IC-07b*	0.3094	0.7788	-1.2840	0.9805	0.45
IC-07b**	3.1449	0.1845	-5.4196	0.9420	4.55
LIM-10	4.0296	0.3612	-2.7687	0.9736	4.07
TF-17	-0.3573	0.7461	-1.3403	0.9965	5.08
IC-04	0.3578	0.7305	-1.3689	0.9944	4.54
TF-24	-0.1401	0.7031	-1.4221	0.9768	5.24
IC-04b	0.8523	0.6975	-1.4335	0.9927	4.56
IC-04c*	0.2683	0.7878	-1.2693	0.9862	0.77
IC-04c**	1.4361	0.4096	-2.4413	0.9886	4.86
IC-06	-0.1317	0.7937	-1.2599	0.9905	4.37
TF-30	-1.3159	0.9972	-1.0028	0.9807	5.52
LIM-02	-0.5172	1.1792	0.8480	0.9987	6.38
TF-36	1.6120	1.4108	-0.7088	0.9982	6.55

\*Principal and \*\*Secondary plagioclase crystal-size families present in each sample.

#### IV.4.4. Internal variability of crystal sizes and CSD closure limit

As predicted by CSD theory, in a steady state open system the slope of straight lines is a direct measure of growth rates and residence time, while the intercept represents its final nucleation density rates. In this sense, these parameters are able to measure the variability of crystal sizes and the final nucleation processes in Limeira intrusion rocks. CSD curves were calculated for all samples, and when required to respective second families of crystals, which resulted in twenty regressions as shown in **Figure 19**. Their principal characteristic is the exponential relationship between these parameters, which results in a decrease in the nucleation process coupled with an increase of crystal-sizes and consequently increase in residence time. Besides that, the variation of crystal-sizes is apparently very dependent on its stratigraphic position.

A different path constituted by the second population of crystals present on the hybrid-zones can be noticed. It results in relatively lesser intercept values than rocks at intrusion borders, with close values of characteristic length. This feature might be the result of different cooling-rates and may suggest a very contrasting process of heat loss between rocks from the edge and inner contacts. The formation of a second family of crystals within an intrusion made of holocrystalline rocks can result of magma mixing, and/or the increase in the nucleation

process due to reheating caused by new magma batches, details of this feature are discussed in the next sections.

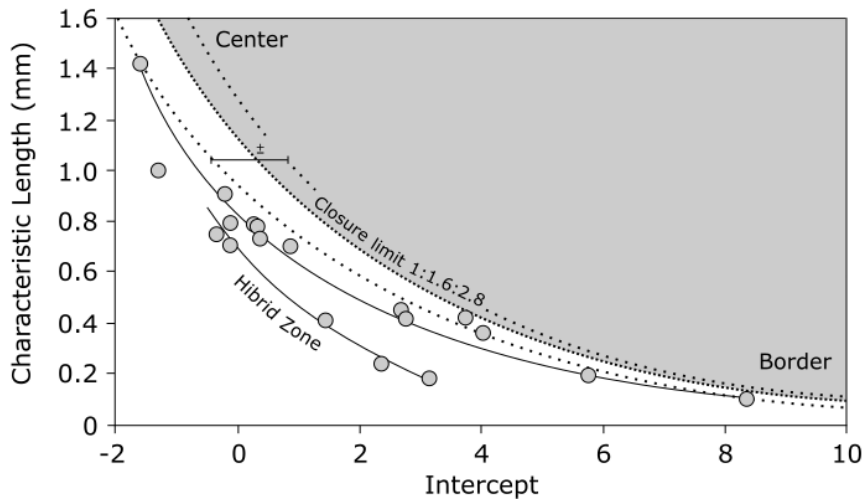


**Figure 19:** Plot of plagioclase characteristic length variations as a function of the CSD lines intercept (final nucleation density,  $n_0$ ) for the results of this study. Calculated closure limit for the average plagioclase aspect ratios (short-: medium-: long-axis = 1:1.6:2.8) considering 100 vol.% crystals (heavy dotted line), 50 vol.% and 150 vol.% (lower and upper light-dotted lines, respectively), following Higgins (2002). Note data distribution along the closure limit and their dependence of the intrusion stratigraphy (central vs. borders zones). The hybrid zones data describe a contrasted path, indicating a relatively lower plagioclase nucleation density. See text for discussion.

In some cases, the plagioclase crystals can constitute more than 50% of modal abundance in analyzed samples. Thence, even if it results in straight lines, CSD's must be verified if stereological conversions have been correctly effectuated. Conversion of two-dimensional into three-dimensional data can result in the closure problem, in which individual phases cannot exceed 100% of rock (Higgins, 2002). As consequence, this system can be verified by comparing the CSD's intercept and its resultant characteristic length ( $C_i = \bar{L}$ ), which is a constant for each CSD line ( $C_i = -1/\text{slope}$ ). Therefore, the closure limit is dependent on the assumed crystal shapes, and its volumetric proportion. It means that discrepancies in it can be the result of CSD calculations, and errors in the determination of crystals shapes and/or proportions. In our case, the closure limit was calculated for the following aspect ratio: 1:1.6:2.8, which represents the mean 3-D shape for plagioclase crystals in samples.

In **Figure 19** is shown the closure limit calculated to crystals with an aspect ratio of 1: 1.6: 2.8, roundness factor equals zero ( $RF = 0$ ), and three different volumetric proportions, 100%  $\pm$ 50% in accordance to Higgins (2002). The outcome validates the resultant CSD lines, plagioclase volumetric proportion, and shape. Variation of characteristic length and CSD intercept are directly related to sample stratigraphic position, which occurs parallel to the Closure Limit and close to the 50% line. An important effect observed in this model is the

inwards decrease of plagioclase modal abundance, compatible with real compositional variations.

#### IV.4.5. Spatial distribution patterns of crystals

Generally, the emplacement of igneous bodies compounds of a great diversity of physical mechanisms, which is also responsible to modify the spatial distribution of crystals (Mock *et al.*, 2003; Jerram *et al.*, 2003). The application of modal-proportion *versus* characteristic length diagram can provide important information about magmatic processes, as suggested by Higgins (2002). In this diagram, almost a systematic variation in modal abundance of plagioclase *versus* CSD's can be observed, principally in the textural coarsening to the centermost region of the intrusion, which is also coupled with the decrease in modal abundance (Figure 20). Variations in modal abundance of plagioclase are directly related to chemical variations of rock composition, and in a closed system, a strong correlation with crystal sizes may be expected. However, as shown by the shades in Figure 20 samples from the hybrid zones exhibits greater values of modal abundance than 'expected', based on our model, for the same crystal size, in this intrusion.

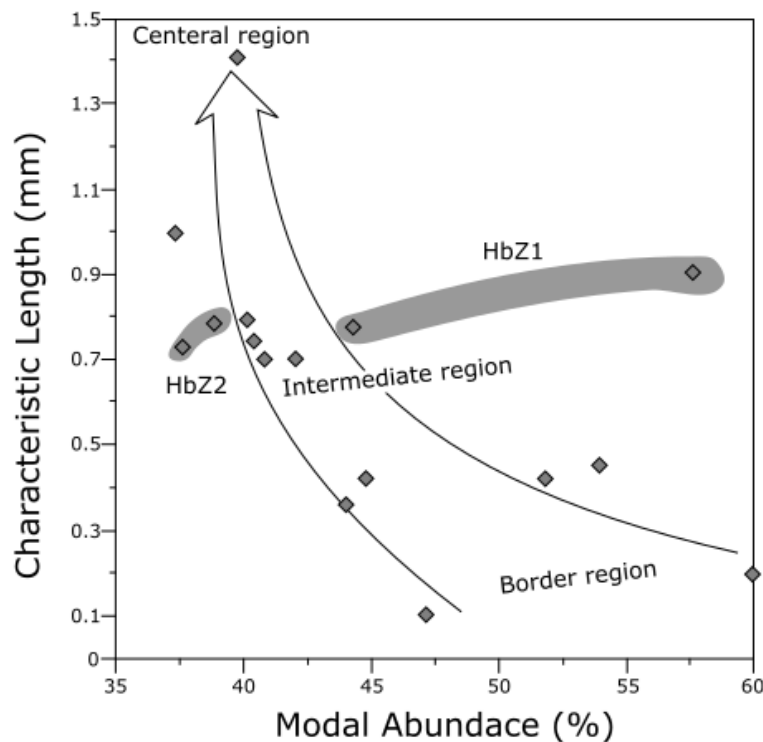


**Figure 20:** Plagioclase characteristic length variation as a function of modal abundance, parameters take as representative of growth-rate and growth-time, respectively (Higgins, 2002). The arrow indicates the approximated trend of textural coarsening within Limeira intrusion; shaded areas depict the dispersion of the Hybrid Zones in relation to the main expected trend. See text for discussion.

As well as in CSD's versus modal abundance diagram, the SDP analysis also shows a roughly systematic variation. In the diagram, R-value *versus* Matrix Volume (**Figure 21**) it is possible to note that our samples exhibit a touching framework in a clustered distribution, with an almost progressive inwards decrease in R-values. A practically direct variation can also be observed, in which the increase in R-values is coupled to the decrease in matrix volume, starting from the borders to the centermost region of the intrusion.

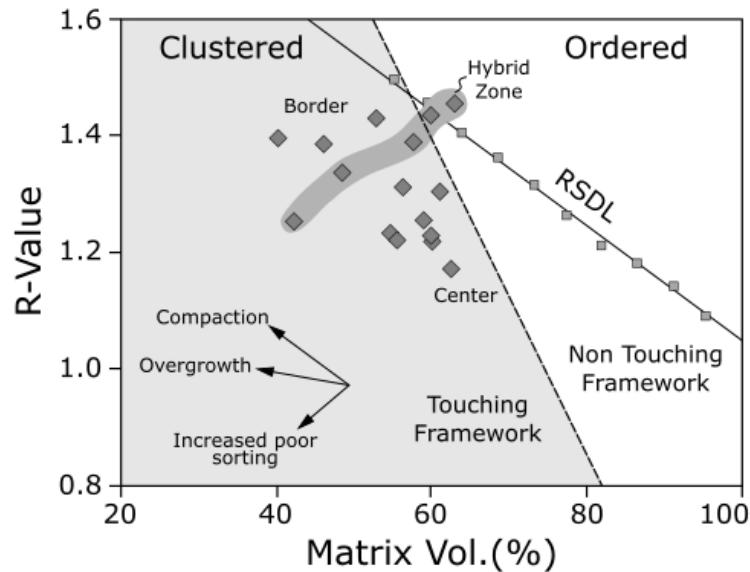


**Figure 21:** R-values versus the matrix abundance (= 100% - plagioclase% vol.) for the CSD results obtained in this study. The Random Sphere Distribution Line (RSDL), as calculated by Jerram et al. (1996), limits clustered from ordered crystal arrangements. Note an almost progressive increase in R-value, coupled to decrease in matrix proportion, from the center to border regions within Limeira intrusion. The shade highlights an observed dispersion, caused by rocks present on Hybrid Zones. See text for discussion.

This relationship is compatible with the compaction/overgrowth trends and presents a great dispersion on its intermediate zones. The dispersion on the evolutionary tendency is more evident in rocks from hybrid zones. As shown by the shade in **Figure 21**, this is the result of an increasingly poor sorting trend, where samples of uppermost hybrid zones presenting non-touching and even ordered frameworks. For tabular intrusions, the R-value method predicts an increase in crystal clustering (decrease in R-value) in regions close to its walls, or even between successive magma batches. In this way, the observed dispersion may be the result of a more complex emplacement process.

The variations of SPD parameters observed in this intrusion are not compatible with a simple stage emplacement, in which the most important dispersions are related to hybrid zones. In this sense, the representation of the R-value, as a function of the depth of the samples, can possibly provide more information about magmatic mechanisms. The results of SDP within Limeira intrusion as a function of each sample's depth are synthesized in **Table 6**.

**Table 6:** Spatial Distribution Patterns values for each analyzed sample and its stratigraphic position.

Sample	Depth*	R-value	Vector length	AF	$\bar{\theta}$ (°)
IC-09 (2)	3	1.429	0.6249	0.08	143
TF-05**	6	1.395	0.6187	0.06	179
IC-08	9	1.336	0.6283	0.03	17
IC-01**	97	1.232	0.6073	0.11	160
IC-09 (7)	16	1.386	0.6001	0.15	156
IC-07a	20	1.251	0.5434	0.26	11
IC-07b	24	1.219	0.5520	0.20	177
LIM-10	28	1.311	0.6616	0.09	73
TF-17**	88	1.221	0.5401	0.21	175
IC-04	38	1.454	0.5921	0.10	173
TF-24**	83	1.255	0.6191	0.09	25
IC-04b	47	1.387	0.6133	0.13	156
IC-04c	52	1.304	0.5983	0.22	28
IC-06	55	1.435	0.5741	0.16	12
TF-30**	74	1.170	0.6075	0.07	179
LIM-02**	110	1.134	0.8520	0.59	72
TF-36	65	1.226	0.7391	0.26	10

Note: In general, values of statistical analysis of crystal orientation exceed the threshold. Indicating a preferential orientation parallel to mean angles. \*Relative depth in meters of samples were made using Limeira intrusion's roof as a reference surface, located at zero. \*\*The depth does not represent the distance from the nearest border.

#### IV.4.6. Emplacement mechanisms and influence of magma flow to rock fabric

During the emplacement of igneous bodies, the magmatic flow and shear are capable to modify the SDP and orientation of crystals, in the chamber. Analogously to a laminar flow in a pipe, the magma flowing within tabular structures (i.e. dikes and sills) can transport large crystals towards its interior ([Mock et al., 2003](#)). The effect of sheet-like intrusions emplacement can result in characteristics R-values profiles, and consequently clustering increase to its borders ([Jerram et al., 1996](#)), as well as close to contacts between consecutive magma batches ([Mock et al., 2003](#)).

A profile of SDP parameters (R-value and Alignment Factor *versus* depth) is presented in **Figure 22a**. The stratigraphic variation of the clustering coincides the lowest R-values (i.e. increase in clustering) with the zones of contact between different rocks, and consequently, it is remarkably coincident with hybrid zones. On the other hand, the highest values of clustering roughly represent the transitional region between different lower-R zones. As seen in **Figure 22a**, the hybrid zones are highlighted by rectangular shades and coinciding with low R-values in three main zones, each one separated by the highest R-values.

Depending on the magma volume and replenishment rate, in a confined environment, the magma flow might align the minerals in the crystallization process. Consequently, the orientation of crystal long-axes in profiles may highlight distinct regions, where the layer

boundaries can be defined by the increase of crystals alignment. Considering this, we constructed a mean crystal orientation profile, which is based on sample stratigraphic position and the plagioclase Alignment Factors (AF) (**Figure 22b**).

Accordingly, the obtained results of AF from most of the tested samples are relatively low when compared to rocks with visible preferential crystal shape orientation. On a scale of 0 to 1, the general values of alignment vary from 0.03 to 0.26, reaching 0.59 in only one sample, representative of the feeder zone and not represented in this profile. Even resulting in small values, the variability of crystal alignment is apparently dependent on its stratigraphic position and related to the hybrid zones. As shown in **Figure 22b**, the highest values of crystal alignment correspond to the hybrid zones, while the lowest values coincide with regions farthest from those areas. Mean crystal long-axis orientation usually results in almost horizontal values at the hybrid zones and can be more dispersed at other positions, as evidenced in **Figure 22b**. The rose diagrams in **Figure 22c** exhibits the dispersion of crystal orientation, revealing the preferential crystal orientation horizontally displayed, roughly parallel to N-S general direction.

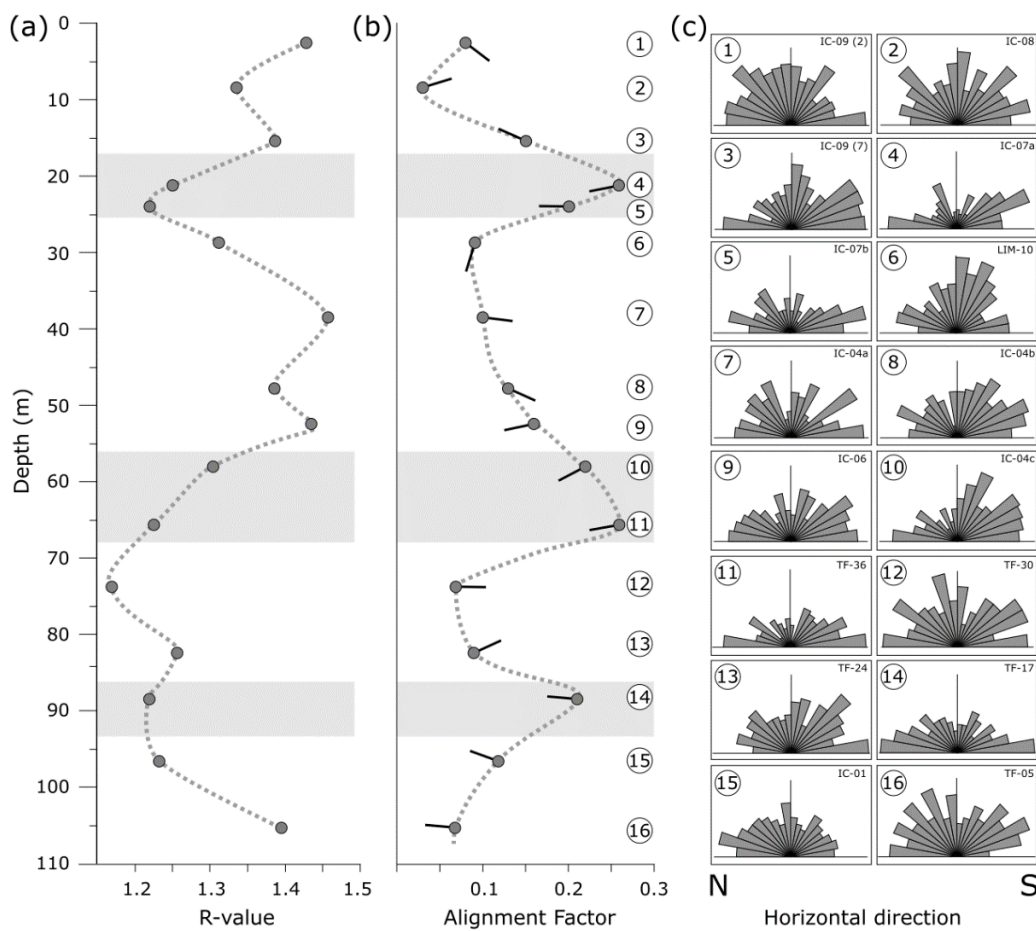


**Figure 22:** Plagioclase crystal clustering (R-Value, a) and alignment factor (AF, b) parameters variations as a function of depth within the Limeira Intrusion. Hybrid zones represented by shaded areas are critical zones defined by the contacts among the main rock-types. Note the correspondence with low R-values and high Alignment Factor values with the critical zones. c) The corresponding rose diagram to each sample, almost N-S oriented generally.

#### IV.4.7. Sr isotope constraints and ICSD plots

The initial  $^{87}\text{Sr}/^{86}\text{Sr}$  values as well as the analytical spots distances from plagioclase crystal cores - obtained for selected samples from the Hybrid zone 1 (HZ1), Central zone (CZ), and Feed zone (FZ) - are listed in **Table 7**, and represented in ICSD-type plots in **Figure 23**. As seen, sample IC-07a from HZ1 present a marked isotope ratio increase from plagioclase core to rims (**Figure 23a**), a pattern also observed for sample TF-36, from CZ (**Figure 23b**). Contrastingly, the opposite behavior can be observed at the FZ, where the Sr-isotopic and crystal-sizes exhibits a negative correlation, and the isotopic signature of the FZ-plagioclase rims are close to those observed in HZ1 and CZ plagioclase cores.

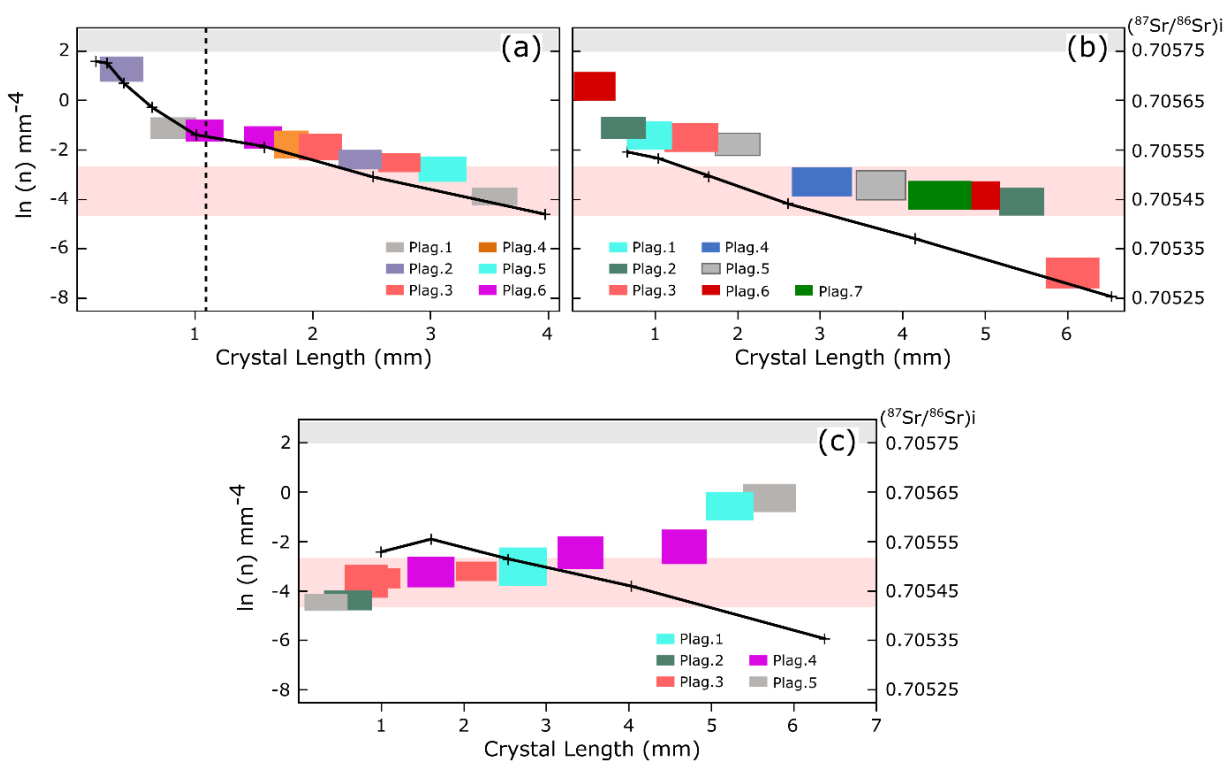


**Figure 23:** ICSD-type diagrams correlating plagioclase crystal size with  $(^{87}\text{Sr}/^{86}\text{Sr})_i$  isotopic initial ratios. a) Sample IC-07a, from the Hybrid-zone 1. Note the kink in the CSD curve coinciding with an abrupt change in isotopic ratios highlighted by the dotted line. b) ICSD plot for TF-36 sample, present in the central region of Limeira intrusion, and c) LIM-02 sample, present at the intrusion's feeder zone. Boxes were drawn with  $\pm 2\sigma$  of uncertainty on isotopic ratios. Initial ratios calculated for a 132 Ma age. The Upper horizontal gray bar represents a whole-rock isotopic initial ratio, from Oliveira & Dantas (2008), and the lower horizontal light-red bar represents the average baseline common for all samples.

Despite being preceded by an apparently gradual variation, the noticeable increase in the isotopic ratio of the sample present at HZ1 (**Figure 23a**) coincides with a significant slope increment in CSD curve. This relationship may be attributed to mixing between filtered-residual melt present in the first magma batch and the second magma injection during the crystallization process, which generate the fine-grained plagioclase family by changing the nucleation- and cooling rates. Variation in isotopic ratios for plagioclase crystals from HZ1 and CZ samples

exhibits similar trends, reaching similar isotopic ratios. Even not exhibiting a kink in CSD curve, histograms for centermost granodiorites frequently presented complex long-axis distributions (**Figure 16b**). Coupled with isotopic analysis, the results indicate a probable magma mixing, which results in plagioclase populations that may have crystallized at the same conditions, marked by the linear CSD results.

In general, isotope ratios vary from a minimum of  $\sim 0.7054$  to maximum values up to  $\sim 0.7057$ . From  $^{87}\text{Sr}/^{86}\text{Sr}$  variation ranges, it is possible to recognize an expressive average isotope ratio ( $\sim 0.705467 \pm 25$ ) as a baseline, represented as the horizontal light red bar in **Figure 23**, present principally in CZ and FZ samples. A more detailed analysis in ICSD plots can reveal the ubiquitous presence of inherited crystal-cores, occurring as antecrysts and representing the largest plagioclase crystals. As observed, inherited cores from HZ1 exhibits the same isotopic ratio than most of CZ plagioclase crystals. On the other hand, the isotopic ratio from CZ plagioclase inherited cores can reach values of  $\sim 0.7053$ , and crystals between  $\sim 6$  to 2 mm of size represent a plateau of isotopic ratios, probably sharing the same evolutionary history of antecrysts present in the sample HZ1, and crystal rims in FZ sample.

**Table 7:** Isotopic  $^{87}\text{Sr}/^{86}\text{Sr}_i$  ratio, uncertainty, and core distance for plagioclase crystals.

Sample	$^{87}\text{Sr}/^{86}\text{Sr}$	Rb/Sr	$^{87}\text{Sr}/^{86}\text{Sr}_i$	Uncertainty (2s)	Distance	Long axis (mm)
<b>IC-07 a</b>						
Plag. 1	0.7054653	0.0019	0.7054551	0.0000390	0.00	Core 3.62
Plag. 1	0.7056025	0.0020	0.7055911	0.0000467	0.85	Rim -
Plag. 2	0.7055505	0.0038	0.7055300	0.0000423	0.00	Core 2.33
Plag. 2	0.7057231	0.0013	0.7057158	0.0000543	0.92	Rim -
Plag. 3	0.7055346	0.0016	0.7055258	0.0000410	0.00	Core 2.80
Plag. 3	0.7055659	0.0018	0.7055564	0.0000564	0.65	Rim -
Plag. 4	0.7055680	0.0017	0.7055589	0.0000595	0.00	Core 1.84
Plag. 5	0.7055208	0.0015	0.7055124	0.0000545	0.00	Core 3.16
Plag. 6	0.7055851	0.0016	0.7055762	0.0000483	0.00	Core 1.78
Plag. 6	0.7055984	0.0018	0.7055887	0.0000472	0.55	Rim -
<b>TF-36</b>						
Plag. 1	0.7055912	0.0019	0.7055808	0.0000487	0.00	Core 0.96
Plag. 2	0.7054689	0.0019	0.7054588	0.0000280	0.00	Core 5.49
Plag. 2	0.7056221	0.0047	0.7055967	0.0000439	0.89	Rim -
Plag. 3	0.7055868	0.0017	0.7055775	0.0000503	0.00	Core 6.04
Plag. 3	0.7053137	0.0021	0.7053022	0.0000302	0.74	Rim -
Plag. 4	0.7054986	0.0023	0.7054861	0.0000303	0.00	Core 3.11
Plag. 5	0.7054900	0.0021	0.7054784	0.0000285	0.00	Core 3.87
Plag. 5	0.7055742	0.0022	0.7055622	0.0000458	0.55	Rim -
Plag. 6	0.7054696	0.0020	0.7054589	0.0000381	0.00	Core 4.96
Plag. 6	0.7056912	0.0015	0.7056830	0.0000580	0.97	Rim -
Plag. 7	0.7054773	0.0061	0.7054440	0.0000403	0.00	Core 4.57

**Table 7 - Continuation:** Isotopic  $^{87}\text{Sr}/^{86}\text{Sr}_i$  ratio, uncertainty, and core distance for plagioclase crystals.

Sample	$^{87}\text{Sr}/^{86}\text{Sr}$	Rb/Sr	$^{87}\text{Sr}/^{86}\text{Sr}_i$	Uncertainty (2s)	Distance	Long axis (mm)
<b>LIM-02</b>						
Plag. 1	0.7056280	0.0017	0.7056188	0.0000692	0.00	Core 5.11
Plag. 1	0.7055317	0.0080	0.7054884	0.0000396	0.55	Rim -
Plag. 2	0.7054406	0.0017	0.7054312	0.0000399	0.00	Core 0.71
Plag. 3	0.7055068	0.0016	0.7054979	0.0000787	0.00	Core 2.22
Plag. 3	0.7054947	0.0020	0.7054752	0.0000660	0.65	Rim -
Plag. 3	0.7054863	0.0046	0.7054699	0.0000408	0.52	Rim -
Plag. 4	0.7055543	0.0027	0.7055396	0.0000340	0.00	Core 4.83
Plag. 4	0.7055338	0.0012	0.7055273	0.0000671	0.73	Rim -
Plag. 4	0.7054964	0.0016	0.7054880	0.0000620	0.34	Rim -
Plag. 5	0.7056447	0.0015	0.7056364	0.0000696	0.00	Core 5.88
Plag. 5	0.7054380	0.0018	0.7054281	0.0000331	0.93	Rim -
Whole-rock			0.7057717	0.0000200	Oliveira & Dantas (2008)	
Siltite			0.7275888	0.0000200	Oliveira & Dantas (2008)	

#### IV.4.8. Residence time and thermal evolution

CSD measurements and sample stratigraphic positioning allow to estimate the residence time for plagioclase and to suggest a thermal evolutionary model for the intrusion. If the plagioclase growth rate (G) is constant, it can be calculated from the CSD's lines slopes when the residence time ( $\Delta t$ ) is known (Eq. 1); from growth rates and the CDS line intercepts, we can estimate the nucleation rate (J). Taking the shape of the Limeira Intrusion as tabular in a first approximation, residence time may be obtained according to [Zieg & Marsh \(2002\)](#) formulation, given by:

$$\tau = \Delta t = z^2 / kb^2 \quad (7)$$

where z, measured in centimeters, is the distance from borders to the central region of the intrusion, k is the constant of thermal diffusivity ( $k = 10^{-2}\text{cm}^2\text{s}^{-1}$ ), and b is the isotherm constant ( $b = 0.475$ ) ([Zieg & Marsh, 2002](#)).

The distances between samples and the intrusion top were measured directly, while the distances from the intrusion bottom and samples downwards the central region were estimated from available magnetometric modeling ([Lino et al., 2018](#)). The obtained values for the  $\tau$ , G, J, and cooling rates are summarized in **Table 8**. The cooling rates were computed considering *liquidus* and *solidus* temperatures about 1250°C and 850°C, respectively, as estimated with Rhyolite-MELTS ([Gualda & Ghiorso, 2014](#)), compatible volatile contents and crystallization close to the QFM (quartz-fayalite-magnetite) buffer. Residence time values vary from *ca.* 231

to 108.367 days from the intrusion upper border to its central region, which results in contrasting cooling rates ranging from 1.733°C/day to 0.004°C/day, respectively.

**Table 8:** Values of residence time, cooling rate, and the distances from Limeira intrusion's borders.

Sample	Z* (cm)	R. Time (s)	R. Time (days)	G (mm s <sup>-1</sup> )	J (n°/mm <sup>-3</sup> s)	(°C/day)
IC-09 (2)	300	1.99 x 10 <sup>7</sup>	231	5.20 x 10 <sup>-9</sup>	2.23 x 10 <sup>-5</sup>	1.7328
TF-05	600*	7.98 x 10 <sup>7</sup>	923	2.47 x 10 <sup>-9</sup>	7.83 x 10 <sup>-7</sup>	0.4332
IC-08	900	1.80 x 10 <sup>8</sup>	2078	2.35 x 10 <sup>-9</sup>	9.86 x 10 <sup>-8</sup>	0.1925
IC-01	1300*	3.75 x 10 <sup>8</sup>	4335	1.12 x 10 <sup>-9</sup>	1.78 x 10 <sup>-8</sup>	0.0923
IC-09 (7)	1600	5.67 x 10 <sup>8</sup>	6566	7.98 x 10 <sup>-10</sup>	1.15 x 10 <sup>-8</sup>	0.0609
IC-07a	2000	8.86 x 10 <sup>8</sup>	10260	1.02 x 10 <sup>-9</sup>	8.15 x 10 <sup>-10</sup>	0.0389
IC-07b	2400	1.28 x 10 <sup>9</sup>	14774	6.10 x 10 <sup>-10</sup>	8.31 x 10 <sup>-10</sup>	0.0270
LIM-10	2800	1.74 x 10 <sup>9</sup>	20109	2.08 x 10 <sup>-10</sup>	1.17 x 10 <sup>-8</sup>	0.0199
TF-17	3000*	1.99 x 10 <sup>9</sup>	23084	3.74 x 10 <sup>-10</sup>	2.61 x 10 <sup>-10</sup>	0.0173
IC-04	3800	3.20 x 10 <sup>9</sup>	37037	2.28 x 10 <sup>-10</sup>	3.26 x 10 <sup>-10</sup>	0.0108
TF-24	4500*	4.49 x 10 <sup>9</sup>	51939	1.56 x 10 <sup>-10</sup>	1.36 x 10 <sup>-10</sup>	0.0077
IC-04b	4700	4.90 x 10 <sup>9</sup>	56658	1.42 x 10 <sup>-10</sup>	3.34 x 10 <sup>-10</sup>	0.0070
IC-04c	5200	5.99 x 10 <sup>9</sup>	69355	1.31 x 10 <sup>-10</sup>	1.72 x 10 <sup>-10</sup>	0.0057
IC-06	5500	6.70 x 10 <sup>9</sup>	77579	1.18 x 10 <sup>-10</sup>	1.04 x 10 <sup>-10</sup>	0.0051
TF-30	5900*	7.71 x 10 <sup>9</sup>	89284	1.29 x 10 <sup>-10</sup>	3.46 x 10 <sup>-11</sup>	0.0044
LIM-02	6200*	8.52 x 10 <sup>9</sup>	98594	1.38 x 10 <sup>-10</sup>	8.25 x 10 <sup>-11</sup>	0.0040
TF-36	6500	9.36 x 10 <sup>9</sup>	108367	1.50 x 10 <sup>-10</sup>	3.00 x 10 <sup>-11</sup>	0.0037

\*Estimated values of edge distance, from geophysical modeling (Lino *et al.*, 2018).

Intrusions that evolves at fixed cooling rates present a typical intercept-slope relation on CSD patterns, given by a CSD line fan when representative samples are plotted altogether, and the relative position of a CSD pattern within that fan can be related to the respective sample position in the intrusion (Zieg & Marsh, 2002). A similar situation is observed in the Limeira patterns, and to check the hypothesis of steady-state crystallization the correlation between CSD intercept [ $\ln(n_0)$ ] and slope (S) values must satisfy the equation:

$$\ln(n_0) = 4 \ln(S) - \ln(C) \quad (8)$$

where C is the dimensionless constant. Results are depicted in **Figure 24a** and demonstrate that the Limeira Intrusion does not conform such a single model. Our patterns define two contrasted correlate sets with contrasted cooling paths, one including samples collected in the upper half of the intrusion and the other grouping samples from the lower half as well as the fine-grained plagioclase populations from the hybrid zones. This indicates different cooling rates, which may be caused by the emplacement of new magma batches at the intrusion's lower half.

The crystal size variations within tabular-like intrusions are directly resultant of the crystallization paths and helps to understand their thermal evolution. Zieg & Marsh (2002) add

a time constant  $t_c$  to the crystallization time  $\tau$  to account for intrusion thickness, as the parameter  $G\tau$  in Eq. 1 is related to the mean crystal sizes, to obtain:

$$\bar{L} = G(\tau + t_c) \quad (9)$$

where  $t_c$  is larger in the case of higher contact temperatures and intrusion thickness, as the cooling at intrusion's contacts demands more time to begin. In **Figure 24b** we plot sample depth ( $Z$ ), the distance from tothe p and bottom intrusion edges, vs. the mean grain-size ( $\bar{L}$ ) of the main plagioclase crystal populations to compare our data with those predicted by the steady-state model. In this diagram, we plot simulations for  $G$  and  $\tau$  values representative that best fits with the centermost and upper border samples, where the models must include growth ratios ranging from the maximum and minimum estimated values,  $3.0 \times 10^{-9} \text{ mm.s}^{-1}$  to  $1.20 \times 10^{-10} \text{ mm.s}^{-1}$ , respectively.

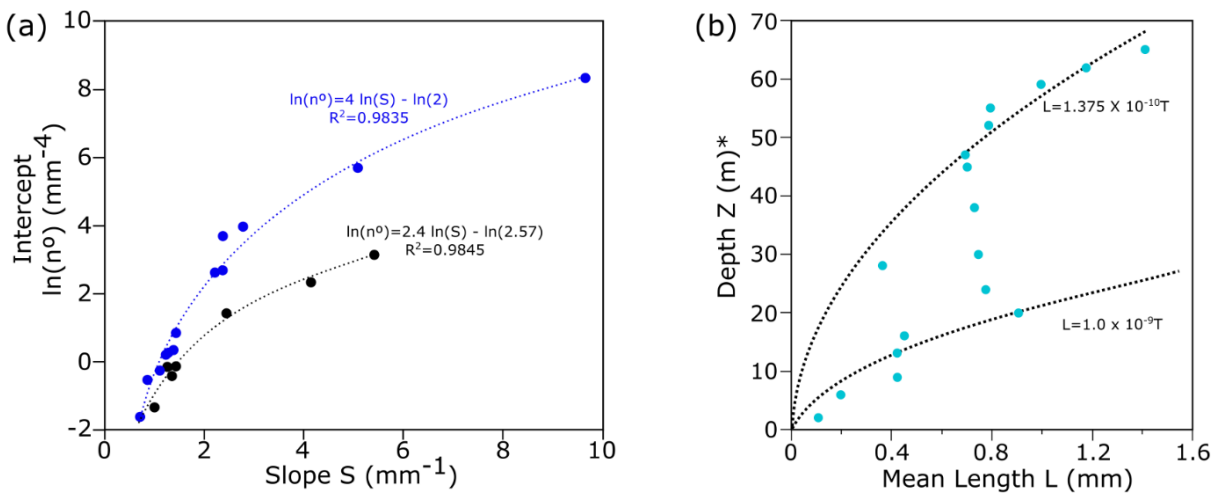


**Figure 24:** Diagrams illustrating the main variation patterns of plagioclase CSD parameters and depth within the Limeira Intrusion. The two model curves in each plot show the expected behavior in steady-state crystallizing systems. a) Intercept vs. slope plot: relatively homogeneous samples from several stratigraphic positions within the intrusion are represented in blue; samples from the hybrid zones and from the lowermost intrusion level in black. b) Depth (\*distance from the nearest contact) vs. crystal mean length plot. Both diagrams indicate significant departures from single models based on a steady-state magmatic evolution. Constant  $C=2$ .

As seen, the first model describe with a good fit the observed crystal-size variation of the central and bottom regions, while the second model accounts the grain-size coarsening from the uppermost region. On the other hand, the intermediate intrusion zone does not conform to any single model, which may instead point to a thermal re-equilibration between the adjacent upper and centermost zones that evolve along two different cooling paths with distinct heat transfer rates.

Considering that the observed crystal-size variation results from multiple injections of magma replenish the magma chamber, the time-span between consecutive pulses is an important issue. From the CSD data alone, it is not possible to constrain the time interval among them. Nevertheless, some information may be extracted from the analysis of the residence time of the second plagioclase crystals generation, which might represent the crystallization final stages, and compared to each other. In our case, we assumed an increase in the nucleation-rate that resulted in the second generation of crystals. In this sense, the residence time was estimated using samples present at the borders that exhibit similar CSD slopes, based on their nucleation-rate as a reference (i.e. TF-05 and IC-08,  $J = 7.82$  and  $98.68 \times 10^{-7}$ ). Moreover, the results of residence time, cooling-rate, reference nucleation-rates, and volumetric proportion of the second plagioclase families are presented in **Table 9**.

**Table 9:** Residence time and plagioclase volumetric proportion from hybrid zones.

Sample	Slope	$G^{\circ}(\text{mm s}^{-1})$	$J^{\circ*1} (\text{n}^{\circ}/\text{mm}^{-3} \text{s})$	$\tau$ (s)	( $^{\circ}\text{C}/\text{day}$ )	(%) Vol.*2
IC-07a (2)*4	-4.1432	$7.39 \times 10^{-8}$	$7.82 \times 10^{-7}$	$3.26 \times 10^7$ (37.79 days)	10.583	9.9168
IC-07b (2)*4	-5.4196	$3.37 \times 10^{-8}$	$7.82 \times 10^{-7}$	$5.47 \times 10^7$ (63.34 days)	6.314	1.8692
IC-04c (2)*4	-2.4413	$2.34 \times 10^{-7}$	$98.68 \times 10^{-7}$	$1.74 \times 10^7$ (201.99 days)	1.980	11.5292

\*1: TF-05 and IC-08 reference nucleation-rate; \*2: the Volumetric proportion of plagioclase second family. Values correspond to a percentage of the total; \*3: Time ratio, between residence time of principal and second plagioclase family; \*4: Second plagioclase family.

As noticed, the residence time for plagioclase crystals at the HZ1 (IC-07a) is less than a fifth of crystallization time for crystals at the HZ2 (IC-04c), and hence, suggests a more rapid cooling due to the thermal gradient. In addition, the residence time increases inwards (IC-07b), with increasing distance from rock contact. At the hybrid-zones, the volumetric proportion of fine-grained plagioclase is apparently constant, ranging from ~10% to 11.5%, despite the drastically inwards decrease. The volumetric variation can suggest a distancing from the zone of interaction between consecutive magma batches and is not observed in HZ2 due to the large time of crystallization taken, as well as the possible thermal re-equilibration

#### IV.5. DISCUSSION

The following sections are addressed to explain and purpose some mechanisms of emplacement that acted during Limeira intrusion formation. To accomplish it, we considered based several features, such as the magma physical properties, isotopic evidence of magmatic interaction, and the effects of time-span between consecutive magmas pulses. We also

discussed the bases of recent models of tabular intrusions formation, and the geological and geometric models for this intrusive occurrence (i.e. Lino *et al.*, 2018).

#### IV.5.1. Structural and compositional aspects

The layout of structures and contact between Limeira intrusion and host-rocks are compatible with some predicted mechanisms of intrusion formation. The sedimentary discontinuity is an important feature, responsible for the creation of an environment with considerable rheological contrast, which accommodates the first magma batch. The host rocks do not present a great rheological contrast, and the formation of a dike protrusion is compatible with the laboratory models of Kavanagh *et al.* (2017) (dike-sill hybrid geometry). The increase in local stress probably results in the horizontal magmatic spreading, responsible for initiate the emplacement of the intrusion.

In **Figure 25a** this process is synthesized based on our data, where the sedimentary contact is responsible for a lithological discontinuity and rheological contrast that acted as a trap. The lack of faults in the sandstone suggests that the first magma pulse might have increased the rheological contrast within the sedimentary rock discontinuity, and the evolutionary process of emplacement occurred by mid-accretion of new magma batches (**Figure 25b, c**).

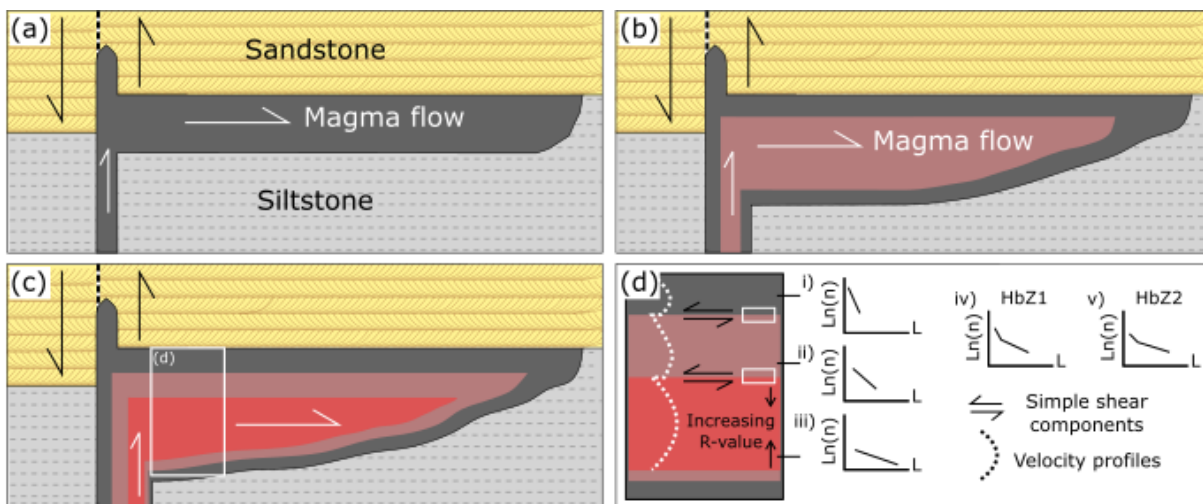


**Figure 25:** Charts illustrating the proposed emplacement model for the Limeira Intrusion. a) First magma pulse emplacement through the feeder dike along a sub-vertical discontinuity. Continuous flow and intrusion along the siltstone-sandstone horizontal contact acting as a “less-stress” structural plane, which results in faulting and upward moving of the sandstone layers over the flow. b) The first magma pulse increases the local rheological contrast, providing the emplacement of subsequent magma batches within the first intrusion, at the region with more ductile behavior. c) The installation of the latter magma pulse, resulting of mid-accretion and final estimated geometry of Limeira intrusion, results of the same acting emplacement mechanism. d) Expected CSD patterns within the constitute intrusion and hybrid zones, velocity profiles, deduced from R-value distributions, and simple shear components at the contacts between magmatic pulses.

Even comprising stratigraphic compositional variations that include some abrupt contacts between different rocks-types, the layout is still compatible with a ‘closed-system’ under fractional crystallization. The main compositional changes are associated with structural and textural variations, principally next to the contacts, where facies are distributed as concentric layers. In general, it is possible to distinguish three main layers with the same structural aspects in this intrusion. The first layer is comprised by gabbro-types; quartz-monzodiorite types with high silica content and the quartz-diorite types, due to the similar structural “jaguar-skin” aspect compose the second layer and finally; and the third layer is composed by granodiorite and quartz-monzodiorite types with low silica content, defining the layered series.

All these three layers are limited by textural variations associated with structural and compositional changes. In the second and third layers, rocks with similar structures and textures compose each one. In addition, it is possible to observe in both layers some common features, as the presence of silica-rich rocks in the uppermost region, and silica-poor rocks at the bottom. These compositional characteristics certainly result in almost independent evolutionary histories to each layer, as the response of fractional crystallization and/or other magmatic processes as crystal settling or immiscibility process due to the presence of layered rocks, for example.

#### **IV.5.2. The influence of magma emplacement dynamics on CSD and SDP**

The resultant CSD and SDP of plagioclase crystals are clearly stratigraphically dependents. Through CSD analysis, it was possible to recognize a systematic inwards increase of grain size, as well as to describe at least two zones of rock contact with more than one crystal-size family. Furthermore, the analysis of the crystals long-axis orientation revealed a strong correlation between the SPO and SDP parameters at the Hybrid Zones. From these results, and coupled with structural, geological, and available geophysical data, it was possible to conceive the evolutionary process of emplacement for the Limeira intrusion (**Figure 25**).

As expected during the emplacement of tabular intrusions, the velocity profiles of magma increase from its edges to the center, while the orientation of crystals increases at the boundaries. From SDP (R-values) and orientation tests, it is possible to distinguish at least three different zones within Limeira intrusion, which each one is limited by relatively great variations of these parameters (**Figure 25d**). Orientation tests resulted in a relatively low-values of Alignment Factors, probably due to the plastic behavior of the “conduct-walls” during magma

emplacement. However, the stratigraphic distribution of crystal orientation values and the mean orientation angle are still compatible with a multiple stage emplacement.

#### **IV.5.3. ICSD analysis and evolution of crystal populations**

The Sr-isotopic analysis of available whole-rock data revealed an inwards decrease in radiogenic strontium ratio in the Limeira intrusion, which ranges varied from 0.707250 at the chilled margins to 0.7057717 at the “central gabbro”, and reaching up to 0.7059697 in the rhyolite veins (Oliveira & Dantas, 2008). Coupled with the obtained *in situ* microanalyses of plagioclase crystals, these variations are compatible with the proposed mechanical model of emplacement. The  $^{87}\text{Sr}/^{86}\text{Sr}_i$  ratio decreases progressively inwards, and as evidenced by sample LIM-02 from the Feeder Zone, it also indicates a decreasing trend in the assimilation of host-rocks by fresh magma pulses. Consequently, it is compatible with a model with added progressive replenishment, in which successive magma pulses through the same conduit does not make contact with the host-rocks.

Close to Hybrid Zones, crystals rims exhibit more radiogenic Sr-ratios than in the cores, revealing that secondary plagioclase family could be the result of “magma mixing” associated with filtered residual melts migration. This process may be responsible for the crystallization during the reheating, and observed humpbacks in UB CSD’s might result from the extraction of residual liquids. The isotopic results, associated with textural and compositional features, corroborates with the mechanism of filter pressing, which may be caused by hyperbolic shear flow during the emplacement of fresh magma pulses. Analysis *In situ* also reveals an important contribution of antecrysts in rocks with medium- to coarse-grain sized, a product of the putative mixing between the two latest intrusions. Although indicating a more complex history, plagioclase crystals present at the central region of Limeira intrusion were submitted to a simple stage crystallization history, and their presence probably increases the estimated residence time due to its common large sizes.

#### **IV.5.4. Effects of time-span between magmatic pulses and thermal evolution**

The thermal evolution of any intrusion is the direct result of its volume, heat accumulation, and heat transfer. In this sense, the volume of successive magma batches and the time span between magmatic pulses exercises a fundamental role in cooling-rate in addition to the textural evolution. In the case of the Limeira intrusion, it is possible to recognize a systematic variation on its textures, principally those on the clinopyroxene and plagioclase shape, and granophyre-types, which are not compatible with the available thermal models. In a

steady state system, formed by one or a few magma pulses in a constant accretion-rate, the same textural variation is virtually not possible.

Considering the thermal models and the metamorphic process of host-rocks, our results enable us to suggest that a small but first pulse initiated the intrusion process, where it acted as a thermal insulation. Furthermore, at least three magma pulses formed the intrusion. Evidence of these three different cooling-paths events is based on the variation of mean grain-size, as seen in **Figure 24b**, and the inflection zones that connect the two different models of mean-length variation corresponds to rocks of HZ 1 e HZ 2.

A detailed structural and micro-textural analysis, coupled with isotopic microanalysis and stratigraphic distributions, allowed us to identify regions of magma interaction within the Limeira intrusion. The preservation of these structures and textures are the result of the time-span between consecutive magma batches. The time-span may seem long enough to cause a great difference in cooling-paths, and if magma composition of successive pulses is considered the same, then the great thermal gradient between these magma batches is a direct result of differences in crystallinity. Finally, based on the marked presence of two-plagioclase grain-size families, as well as the difference of residence time, we suggest that the time-span between the first and second pulses was greater than the interval between the second and third.

## IV.6. CONCLUSION

The integration of host-rock structural aspects, the compositional features of rock-types, textural distribution, quantitative textural analysis and in situ isotopic ratios of Sr in plagioclase crystals, allowed us to interpret and quantify the emplacement process and the thermal evolution of Limeira intrusion. Consequently, our results strongly support a multiple-stage igneous evolution, caused by non-instantaneous successive emplacement of different magma pulses during the assembly of this intrusion. The apparent alignment (SPO) and clustering (SPD) of crystals corroborate with the amalgamation process of successive sill-like magma batches, on the formation and growth of this intrusion. Moreover, the isotopic data suggested small amounts of country rocks assimilation and an important contribution of the filter-pressing mechanism during its emplacement and evolution, and probably contributing to the increase in silica content and great diversity of rock-types.

Internal compositional and structural heterogeneities of Limeira intrusion has long been related solely to the process of fractional crystallization in a closed-system, associated with filter pressing. However, the CSD's strongly suggest crystals had grown under the influence of changes in the cooling path. In addition, the inwards variation of grain-size also supports the three thermal-independent reinjections model, which resulted in a great internal accumulation of heat. Major cooling between batches provided an important rheological response, being capable to act as a trap for consecutive pulses. It was responsible for the generation of a rigid surface in a confined environment, where crystals have aligned and clustered. Additionally, the complex thermal evolution of Limeira intrusion might be a great influence for its structural, textural, and compositional heterogeneities, as well as its magmatic evolutionary process.

Even comprising layered rocks, crystal alignment is not compatible with the mechanism of crystal settling or flux-segregation, as observed in many analogous occurrences. Therefore, these results might open avenues for characterization and quantification of specific magmatic processes, which acted during the formation of Limeira intrusion. As a result, this study provides significant data, which can be tested and, perhaps, extrapolated to other layered intrusions, especially those related to heat maintenance and other specific magmatic mechanisms.

## CHAPTER V

### V.1. SYNTHESIS AND CONCLUSIONS

The integration of ground and aerial magnetic data, geological information and magnetic susceptibility measurements in rocks allowed set out an improved interpretation of the lateral distribution and the 2D geometry of the Limeira Intrusion. Additionally, host-rock structural aspects, the compositional features of rock-types, textural distribution, quantitative textural analysis and in situ Sr-isotopic ratios in plagioclase crystals, allowed interpret and quantify the emplacement process and its thermal evolution, respectively. The main conclusions of this dissertation may be highlighted as follows:

- (1) The Limeira intrusion has an elliptical-like shape from its top-view, occupying a top area of about 2.5 to 3.0 km<sup>2</sup> and its thickest zone corresponds to the Cavinatto quarry north portion;
- (2) The modeled two-dimensional magnetometric profiles support a lopolithic-like intrusion geometry, as previously suggested from geologic and petrologic evidence (e.g., [Lino, 2015](#));
- (3) The analysis of the two-dimensional profiles allows inferring that the intrusion evolved through progressively emplacement of fresh magmatic pulses in the central zone of the magmatic chamber, causing its growth by mechanisms of inner-accretion (e.g., [Menand, 2011](#));
- (4) The northern region coincides with the thicker zone of the intrusion, and supports the hypothesis that this may be the feeder area of the intrusion;
- (5) Compositional and textural data strongly supports a multiple-stage igneous evolution, caused by non-instantaneous successive emplacement of different magma pulses during the assembly of this intrusion, coherent with the results based on the obtained geophysical model;
- (6) The apparent alignment (SPO) and clustering (SPD) of plagioclase crystals corroborates with an amalgamation process made up by successive sheet-like magma batches;
- (7) The available and obtained Sr-isotopic results, coupled with textural analysis, are suggestive of small amounts of country rocks assimilation, especially from the rock-types present at Limeira intrusion borders, and evidenced by inherited-anticrystal cores (with high <sup>87</sup>Sr/<sup>86</sup>Sr ratios) in the feeder zone;

- (8) Additionally, an important contribution of the filter-pressing mechanism, during its emplacement and evolution, is evidenced by the high  $^{87}\text{Sr}/^{86}\text{Sr}$  ratios obtained in the plagioclase crystal rims and/or smallest crystals, formed during magmatic mixing at Hybrid Zones. Probably the filter-pressing has contributed to the increase in silica content inwards and the great diversity of rock-types;
- (9) The assembly process can be attributed to the amalgamation of at least three magma pulses, each one emplaced within the precursor. It results in a stepped-wise cooling process, in which each magmatic layer evolves separately and heat accumulation may be responsible for the extremely coarsening of the inner rock-types;
- (10) Finally, the results open new avenues for detailed thermal studies, based on the total size of the intrusion and the estimative of each magma pulse volume. Also can be used to reveal the influence of consecutive magma pulses in the heterogeneous distribution and variety of hydrothermal mineral phases;
- (11) The chemical stratigraphy and modeling of the magmatic evolution can also indicate the influence of continuous replenishments and heat accumulation within this magma chamber. Already obtained chemical results are compatible with the proposed emplacement model and reveal that each magma pulse might have evolved almost independent. In addition, layered structures recognized in the last injection may be associated with magma unmixing in the tholeiitic line of descent.

## REFERENCES

- Abramoff, M.D., Magalhães, P.J., Ram, S.J., (2004). Image processing with ImageJ. *Biophoton*, 11, 36–42.
- Annen, C. (2011). Implications of incremental emplacement of magma bodies for magma differentiation, thermal aureole dimensions and plutonism–volcanism relationships. *Tectonophysics*, 500(1-4), 3-10.
- Annen, C., & Sparks, R. S. J. (2002). Effects of repetitive emplacement of basaltic intrusions on thermal evolution and melt generation in the crust. *Earth and Planetary Science Letters*, 203(3-4), 937-955.
- Baranov, V. (1957). A new method for interpretation of aeromagnetic maps: pseudo-gravimetric anomalies. *Geophysics*, 22(2), 359-382.
- Barker, D. S. (1970). Compositions of granophyre, myrmekite, and graphic granite. *Geological Society of America Bulletin*, 81(11), 3339-3350.
- Bellieni, G., Comin-Chiaramonti, P., Marques, L. S., Melfi, A. J., Piccirillo, E. M., Nardy, A. J. R., & Roisenberg, A. (1984). High- and low-TiO<sub>2</sub> flood basalts from the Paraná plateau (Brazil): petrology and geochemical aspects bearing on their mantle origin. *Neues Jahrbuch für Mineralogie*, 150, 273-306.
- Bizzarro, M., Simonetti, A., Stevenson, R. K., & Kurszlaukis, S. (2003). In situ <sup>87</sup>Sr/<sup>86</sup>Sr investigation of igneous apatites and carbonates using laser-ablation MC-ICP-MS. *Geochimica et Cosmochimica Acta*, 67(2), 289-302.
- Bunger, A. P., & Cruden, A. R. (2011). Modeling the growth of laccoliths and large mafic sills: Role of magma body forces. *Journal of Geophysical Research: Solid Earth*, 116(B2).
- Burkhart, L., Hoyt, R. C., & Oolman, T. (1980). *Control of particle size distribution and agglomeration in continuous precipitators*. In: Kuczynski, G.C. (Ed.). *Sintering Processes*. Plenum, NY, pp. 23-38.
- Briggs, I. C. (1974). Machine contouring using minimum curvature. *Geophysics*, 39(1), 39-48.
- Brückmann, M., Hartmann, L. A., Tassinari, C. C. G., Sato, K., & Baggio, S. B. (2014). The duration of magmatism in the Serra Geral Group, Paraná volcanic province. *Metallogeny and Crustal Evolution of the Serra Geral Group*, 1, 507-518.
- Bryan, S. E., & Ernst, R. E. (2008). Revised definition of large igneous provinces (LIPs). *Earth-Science Reviews*, 86(1-4), 175-202.
- Capaccioni, B., Valentini, L., Rocchi, M. B., Nappi, G., & Sarocchi, D. (1997). Image analysis and circular statistics for shape-fabric analysis: applications to lithified ignimbrites. *Bulletin of Volcanology*, 58(7), 501-514.
- Cartwright, J., & Hansen, D. M. (2006). Magma transport through the crust via interconnected sill complexes. *Geology*, 34(11), 929-932.
- Cashman, K. V. (1993). Relationship between plagioclase crystallization and cooling rate in basaltic melts. *Contributions to Mineralogy and Petrology*, 113(1), 126-142.
- Cashman, K. V., & Marsh, B. D. (1988). Crystal size distribution (CSD) in rocks and the kinetics and dynamics of crystallization II: Makaopuhi Lava Lake. *Contributions to Mineralogy and Petrology*, 99(3), 292-305.
- Cavallaro, F. D. A. (2013). *Investigação Geofísica do Alto Estrutural de Anhembi-SP* (Doctoral dissertation, Universidade de São Paulo).
- Chayes, F. (1965). Reliability of point counting results; discussion. *American Journal of Science*, 263(8), 719-721.

- Coleman, D. S., Gray, W., & Glazner, A. F. (2004). Rethinking the emplacement and evolution of zoned plutons: Geochronologic evidence for incremental assembly of the Tuolumne Intrusive Suite, California. *Geology*, 32(5), 433-436.
- Comin-Chiaramonti, P., Bellieni, G., Piccirillo, E. M., & Melfi, A. J. (1988). Classification and petrography of continental stratoid volcanic and related intrusive from the Paraná Basin (Brasil). *The Mesozoic flood volcanism of the Paraná Basin: petrogenetic and geophysical aspects*. São Paulo, IAG-USP, 47-72.
- Cordani, R., & Shukowsky, W. (2009). Magnetização remanescente: um parâmetro crucial para a interpretação e modelamento de anomalias magnéticas em território brasileiro. *Revista Brasileira de Geofísica*, 27(4), 659-667.
- Cruden, A. R. (1998). On the emplacement of tabular granites. *Journal of the Geological Society-London*, 155(5), 853-862.
- Davis, J. (1986). *Statistics and data analysis in geology*. New York: John Willey & Sons, Inc.
- Ernesto, M., Marques, L. S., Piccirillo, E. M., Molina, E. C., Ussami, N., Comin-Chiaramonti, P., & Bellieni, G. (2002). Paraná Magmatic Province–Tristan da Cunha plume system: fixed versus mobile plume, petrogenetic considerations and alternative heat sources. *Journal of Volcanology and Geothermal Research*, 118(1-2), 15-36.
- Ernesto, M., Raposo, M. I. B., Marques, L. S., Renne, P. R., Diogo, L. A., & De Min, A. (1999). Paleomagnetism, geochemistry and  $^{40}\text{Ar}/^{39}\text{Ar}$  dating of the North-eastern Paraná magmatic province: tectonic implications. *Journal of Geodynamics*, 28(4), 321-340.
- Ernesto, M. and Pacca, I. G. 1988. Paleomagnetism of the Paraná Basin Flood volcancs, Southern Brasil In: Piccirillo, E. M. and Melfi, A. J. (eds.) *The Mesozoic Flood Volcanism of the Paraná Basin: Petrogenetic and Geophys. Aspects*. IAG-USP, São Paulo, .229-255.
- Faria, C. A. (2008). *Evolução magmática do sill de Limeira: Petrografia e Geoquímica* (Masters dissertation, University of São Paulo) 106p. <http://www.teses.usp.br/teses/disponiveis/44/44143/tde-04122008-152040/en.php>
- Ferreira, F. J., de Souza, J., de B. e S. Bongiolo, A., & de Castro, L. G. (2013). Enhancement of the total horizontal gradient of magnetic anomalies using the tilt angle. *Geophysics*, 78(3), J33-J41.
- Fialko, Y. A., & Rubin, A. M. (1999). Thermal and mechanical aspects of magma emplacement in giant dike swarms. *Journal of Geophysical Research: Solid Earth*, 104(B10), 23033-23049.
- Frank, H. T., Gomes, M. E. B., Formoso, M. L. L. (2009). Review of the areal extent and the volume of the Serra Geral Formation, Paraná Basin, South America. *Pesquisas em Geociências*, 36(1), 49-57.
- Franke, W. (1992). Phanerozoic structures and events in Central Europe. *Blundell D, Freeman R, Mueller S (eds) A continent revealed: the European Geotraverse*. Cambridge University Press, Cambridge, 164-179.
- Gallagher, K., & Hawkesworth, C. (1994). Mantle plumes, continental magmatism and asymmetry in the South Atlantic. *Earth and Planetary Science Letters*, 123(1-3), 105-117.
- Glazner, A. F., Bartley, J. M., Coleman, D. S., Gray, W., & Taylor, R. Z. (2004). Are plutons assembled over millions of years by amalgamation from small magma chambers?. *GSA today*, 14(4/5), 4-12.
- Gualda, G. A. (2006). Crystal size distributions derived from 3D datasets: Sample size versus uncertainties. *Journal of Petrology*, 47(6), 1245-1254.
- Gualda, G. A., & Ghiorso, M. S. (2014). Phase-equilibrium geobarometers for silicic rocks based on rhyolite-MELTS. Part 1: Principles, procedures, and evaluation of the method. *Contributions to Mineralogy and Petrology*, 168(1), 1033.

- Hartmann, G. A., & Pacca, I. G. (2009). Time evolution of the South Atlantic magnetic anomaly. *Anais da Academia Brasileira de Ciências*, 81(2), 243-255.
- Hartmann, L. A. (2014). Introduction to the natural history of the Serra Geral Group. In: Hartmann L.A. & Baggio S.B. (eds.), *Metallogeny and mineral exploration in the Serra Geral Group*. Rio Grande do Sul, UFRGS Academic Press. v. 1, p. 299-302.
- Hawkes, L., & Hawkes, H. K. (1933). The Sandfell laccolith and 'dome of elevation'. *Quarterly Journal of the Geological Society*, 89(1-4), 379-400.
- Hawkesworth, C. J., Gallagher, K., Kelley, S., Mantovani, M., Peate, D. W., Regelous, M., & Rogers, N. W. (1992). Paraná magmatism and the opening of the South Atlantic. *Geological Society, London, Special Publications*, 68(1), 221-240.
- Higgins, M. D. (1996). Magma dynamics beneath Kameni volcano, Thera, Greece, as revealed by crystal size and shape measurements. *Journal of Volcanology and Geothermal Research*, 70(1-2), 37-48.
- Higgins, M. D. (2000). Measurement of crystal size distributions. *American Mineralogist*, 85(9), 1105-1116.
- Higgins, M. D. (2002). A crystal size-distribution study of the Kiglapait layered mafic intrusion, Labrador, Canada: evidence for textural coarsening. *Contributions to mineralogy and petrology*, 144(3), 314-330.
- Higgins, M. D. (2006). *Quantitative textural measurements in igneous and metamorphic petrology*. Cambridge University Press.
- Horsman, E., Tikoff, B., & Morgan, S. (2005). Emplacement-related fabric and multiple sheets in the Maiden Creek sill, Henry Mountains, Utah, USA. *Journal of Structural Geology*, 27(8), 1426-1444.
- Iezzi, G., & Ventura, G. (2002). Crystal fabric evolution in lava flows: results from numerical simulations. *Earth and Planetary Science Letters*, 200(1-2), 33-46.
- Jerram, D. A., & Cheadle, M. J. (2000). On the cluster analysis of grains and crystals in rocks. *American Mineralogist*, 85(1), 47-67.
- Jerram, D. A., Cheadle, M. J., Hunter, R. H., Elliott, M. T. (1996). The spatial distribution of grains and crystals in rocks. *Contributions to Mineralogy and Petrology*, 125(1), 60-74.
- Jerram, D. A., Cheadle, M. J., & Philpotts, A. R. (2003). Quantifying the building blocks of igneous rocks: are clustered crystal frameworks the foundation?. *Journal of Petrology*, 44(11), 2033-2051.
- Kavanagh, J. L., Menand, T., & Sparks, R. S. J. (2006). An experimental investigation of sill formation and propagation in layered elastic media. *Earth and Planetary Science Letters*, 245(3-4), 799-813.
- Kavanagh, J. L., Rogers, B. D., Boutelier, D., & Cruden, A. R. (2017). Controls on sill and dyke-sill hybrid geometry and propagation in the crust: The role of fracture toughness. *Tectonophysics*, 698, 109-120.
- Kearey, P., Brooks, M. (2002). *An introduction to Geophysical exploration*. Blackwell Sci. Publ. Boston, 296 p.
- Lameyre, J., & Bowden, P. (1982). Plutonic rock types series: discrimination of various granitoid series and related rocks. *Journal of Volcanology and Geothermal Research*, 14(1-2), 169-186.
- Launeau, P., & Cruden, A. R. (1998). Magmatic fabric acquisition mechanisms in a syenite: results of a combined anisotropy of magnetic susceptibility and image analysis study. *Journal of Geophysical Research: Solid Earth*, 103(B3), 5067-5089.
- Li, X. (2006). Understanding 3D analytic signal amplitude. *Geophysics*, 71(2), L13-L16.
- Lino, L. M. (2015). *A intrusão toleítica de Limeira (SP) contribuição à geologia e estratigrafia de uma intrusão acamadada*. Monograph, Institute of Geoscience, University of São Paulo, São Paulo, 60 p.

- Lino, L. M., Cavallaro, F. A., Vlach, S. R. F., Coelho, D. C. (2018). 2D magnetometric modeling of a basic-intermediate intrusion geometry: geophysical and geological approaches applied to the Limeira intrusion, Paraná Magmatic Province (SP, Brazil). *Brazilian Journal of Geology*, 48(2), 305-315.
- Marques, L. S., & Ernesto, M. (2004). O magmatismo toleítico da Bacia do Paraná. *Mantesso Neto, V.; Bartorelli, A.; Carneiro, CR*, 245-263.
- Marques, L. S., Dupré, B., & Piccirillo, E. M. (1999). Mantle source compositions of the Paraná Magmatic Province (southern Brazil): evidence from trace element and Sr–Nd–Pb isotope geochemistry. *Journal of Geodynamics*, 28(4-5), 439-458.
- Marsh, B. D. (1988). Crystal size distribution (CSD) in rocks and the kinetics and dynamics of crystallization. *Contributions to Mineralogy and Petrology*, 99(3), 277-291.
- Marsh, B. D. (1998). On the interpretation of crystal size distributions in magmatic systems. *Journal of Petrology*, 39(4), 553-599.
- Matzel, J. E., Bowring, S. A., & Miller, R. B. (2006). Time scales of pluton construction at differing crustal levels: Examples from the Mount Stuart and Tenpeak intrusions, North Cascades, Washington. *Geological Society of America Bulletin*, 118(11-12), 1412-1430.
- Menand, T. (2008). The mechanics and dynamics of sills in layered elastic rocks and their implications for the growth of laccoliths and other igneous complexes. *Earth and Planetary Science Letters*, 267(1-2), 93-99.
- Menand, T., Daniels, K. A., & Benghiat, P. (2010). Dyke propagation and sill formation in a compressive tectonic environment. *Journal of Geophysical Research: Solid Earth*, 115(B8).
- Menand, T. (2011). Physical controls and depth of emplacement of igneous bodies: A review. *Tectonophysics*, 500(1-4), 11-19.
- Michaut, C., & Jaupart, C. (2006). Ultra-rapid formation of large volumes of evolved magma. *Earth and Planetary Science Letters*, 250(1-2), 38-52.
- Milani, E. J. (1992). Intraplate tectonics and the evolution of the Paraná basin, SE Brazil. *Inversion tectonics of the Cape fold belt, Karroo and Cretaceous basins of southern Africa: Rotterdam, Balkema*, 101-108.
- Milani, E. J. (2004). Comentários sobre a origem e evolução tectônica da Bacia do Paraná. *Mantesso-Neto, V.; Bartorelli, A.; Carneiro, CDR*, 265-291.
- Miller, C. F., Furbish, D. J., Walker, B. A., Claiborne, L. L., Koteas, G. C., Bleick, H. A., & Miller, J. S. (2011). Growth of plutons by incremental emplacement of sheets in crystal-rich host: Evidence from Miocene intrusions of the Colorado River region, Nevada, USA. *Tectonophysics*, 500(1-4), 65-77.
- Milsom, J. (2003). *Field geophysics*. London. John Wiley and Sons, 229p.
- Mock, A., & Jerram, D. A. (2005). Crystal size distributions (CSD) in three dimensions: insights from the 3D reconstruction of a highly porphyritic rhyolite. *Journal of Petrology*, 46(8), 1525-1541.
- Mock, A., Jerram, D. A., & Breitzkreuz, C. (2003). Using quantitative textural analysis to understand the emplacement of shallow-level rhyolitic laccoliths—a case study from the Halle Volcanic Complex, Germany. *Journal of Petrology*, 44(5), 833-849.
- Morgan, D. J., & Jerram, D. A. (2006). On estimating crystal shape for crystal size distribution analysis. *Journal of Volcanology and Geothermal Research*, 154(1-2), 1-7.
- Morgan, D. J., Jerram, D. A., Chertkoff, D. G., Davidson, J. P., Pearson, D. G., Kronz, A., & Nowell, G. M. (2007). Combining CSD and isotopic microanalysis: magma supply and mixing processes at Stromboli Volcano, Aeolian Islands, Italy. *Earth and Planetary Science Letters*, 260(3-4), 419-431.

- Nabighian, M. N. (1972). The analytic signal of two-dimensional magnetic bodies with polygonal cross-section: its properties and use for automated anomaly interpretation. *Geophysics*, 37(3), 507-517.
- Nabighian, M. N. (1984). Toward a three-dimensional automatic interpretation of potential field data via generalized Hilbert transforms: Fundamental relations. *Geophysics*, 49(6), 780-786.
- Nardy, A. J. R., oliveira, M., Betancourt, R., Verdugo, D., & Machado, F. (2002). Geologia e estratigrafia da Formação Serra Geral. *Geociências*, 21(2), 15-32.
- Nardy, A. J. R., oliveira, M., Betancourt, R., Verdugo, D., & Machado, F. (2003). Litoestratigrafia da Formação Serra Geral. *Geociências*, 21(2), 15-32.
- Oliveira, E. P., Sato, L., Gomes, L. C. C., & Martins, G. (1998). Large scale magmatic banding in mesozoic basic sill of the Paraná basin, Campinas, São Paulo State, Brazil. *Boletim IG-USP. Série Científica*, 29, 220-220.
- Oliveira, E. P. & Dantas, E. (2008). Closed-system differentiation in mesozoic high-Ti basic sill of Limeira, São Paulo State: implications for the origin of bimodal felsic-mafic volcanic rock in the Paraná Igneous Province. *IV Simpósio de Vulcanismo e Ambientes Associados*, Foz do Iguaçu: SBG.
- Paton, C., Woodhead, J. D., Hergt, J. M., Phillips, D., & Shee, S. (2007). Strontium isotope analysis of kimberlitic groundmass perovskite via LA-MC-ICP-MS. *Geostandards and Geoanalytical Research*, 31(4), 321-330.
- Peate, D. W., Hawkesworth, C. J., Mantovani, M. S., & Shukowsky, W. (1990). Mantle plumes and flood-basalt stratigraphy in the Parana, South America. *Geology*, 18(12), 1223-1226.
- Peate, D. W., Hawkesworth, C. J., & Mantovani, M. S. (1992). Chemical stratigraphy of the Paraná lavas (South America): classification of magma types and their spatial distribution. *Bulletin of Volcanology*, 55(1-2), 119-139.
- Peate, D. W., & Hawkesworth, C. J. (1996). Lithospheric to asthenospheric transition in low-Ti flood basalts from southern Parana, Brazil. *Chemical Geology*, 127(1-3), 1-24.
- Peate, D. W. (1997). The Paraná-Etendeka Province. In: Mahoney, J. J. and Coffin, M. F. (eds.). Large igneous provinces: Continental, oceanic, and planetary flood volcanism. Geophysical Monograph, Washington DC, American Geophysical Union, p. 217-245.
- Peate, D. W., Hawkesworth, C. J., Mantovani, M. M., Rogers, N. W., & Turner, S. P. (1999). Petrogenesis and stratigraphy of the high-Ti/Y Urubici magma type in the Paraná flood basalt province and implications for the nature of 'Dupal'-type mantle in the South Atlantic region. *Journal of Petrology*, 40(3), 451-473.
- Pedley, R. C., Busby, J. P., Dabek, Z. K. (1997). GRAVMAG User manual: interactive 2.5D gravity and magnetic modeling. *British Geological Survey, Technical Report*, 73 p.
- Perrota, M. M., Salvador, E. D. (2005). *Mapa geológico do Estado de São Paulo – Integração na escala 1:750.000*. São Paulo, Programa de levantamentos geológicos do Brasil, CPRM.
- Phillips, J. D. (2007). *Geosoft eXecutables (GX's) developed by the US Geological Survey, version 2.0, with notes on GX development from Fortran code* (p. 111). US Geological Survey.
- Piccirillo, E. M., Melfi, A. J., Comin-Chiaramonti, P., Bellieni, G., Ernesto, M., Marques, L. S., Nardy, A. J. R., Pacca, I. G., Roisenberg, A., Stolfa, D. (1988a). Continental flood volcanism from the Paraná Basin (Brazil). In *Continental Flood Basalts* (pp. 195-238). Springer, Dordrecht.
- Ramos, F. C., Wolff, J. A., & Tollstrup, D. L. (2004). Measuring <sup>87</sup>Sr/<sup>86</sup>Sr variations in minerals and groundmass from basalts using LA-MC-ICPMS. *Chemical Geology*, 211(1-2), 135-158.
- Randolph, A. D., & Larson, M. A. (1971). *Theory of Particle Process*. Academic Press, New York, 251p.
- Rudnick, R. L., & Fountain, D. M. (1995). Nature and composition of the continental crust: a lower crustal perspective. *Reviews of geophysics*, 33(3), 267-309.

- Seixas, A. R., Nardy, A. J. R., Moreira, C. A., & Pereira, A. M. (2015). Caracterização magnetométrica do Sill de Limeira-SP. *Geociências*, 169-184.
- Smith, J. V. (1974). *Feldspar Minerals. Tom 2. Chemical and Textural Properties*. Springer-Verlag.
- Soares, P. C. (1985). Informações sobre sills de diabásio da Bacia do Paraná. *Curitiba: DOCEGEO*.
- Streckeisen, A. (1976). To each plutonic rock its proper name. *Earth-science reviews*, 12(1), 1-33.
- Swan, A. R., & Sandilands, M. (1995). Introduction to geological data analysis. In *International Journal of Rock Mechanics and Mining Sciences and Geomechanics Abstracts*(Vol. 8, No. 32, p. 387A).
- Telford, W. M., Geldart, L. P., Sheriff, R. E., Keys, D. A. (1976). *Applied Geophysics*. Cambridge University Press, 860p.
- Thiede, D. S., & Vasconcelos, P. M. (2010). Paraná flood basalts: rapid extrusion hypothesis confirmed by new <sup>40</sup>Ar/<sup>39</sup>Ar results. *Geology*, 38(8), 747-750.
- Turcotte, D. L., Emerman, S. H., & Spence, D. A. (1987). Mechanics of dyke injection. In *Mafic Dyke Swarms* (Vol. 34, pp. 25-29). Spec. Publ. Geol. Ass. Canada.
- Turner, S., & Hawkesworth, C. (1995). The nature of the sub-continental mantle: constraints from the major-element composition of continental flood basalts. *Chemical Geology*, 120(3-4), 295-314.
- Turner, S., Regelous, M., Kelley, S., Hawkesworth, C., & Mantovani, M. (1994). Magmatism and continental break-up in the South Atlantic: high precision <sup>40</sup>Ar-<sup>39</sup>Ar geochronology. *Earth and Planetary Science Letters*, 121(3-4), 333-348.
- Ulbrich, H. H., Vlach, S. R., & Janasi, V. A. (2017). O mapeamento faciológico em rochas ígneas plutônicas. *Revista Brasileira de Geociências*, 31(2), 163-172.
- Vinet, N., & Higgins, M. D. (2010). Magma solidification processes beneath Kilauea volcano, Hawaii: A quantitative textural and geochemical study of the 1969–1974 Mauna Ulu Lavas. *Journal of Petrology*, 51(6), 1297-1332.
- Vinet, N., & Higgins, M. D. (2011). What can crystal size distributions and olivine compositions tell us about magma solidification processes inside Kilauea Iki lava lake, Hawaii?. *Journal of Volcanology and Geothermal Research*, 208(3), 136-162.
- Waichel, B. L., de Lima, E. F., Lubachesky, R., & Sommer, C. A. (2006). Pahoehoe flows from the central Paraná continental flood basalts. *Bulletin of Volcanology*, 68(7-8), 599-610.
- Zalán, P. V., Conceição, J. D. J., Wolff, S., Astolfi, M. A. M., Vieira, I. S., Appi, V. T., Neto, E. V. S., Cerqueira, J.R., Zanotto, O. A., Paumer, M. L., Marques, A. (1986). Análise da bacia do Paraná. *Relatório Interno Gt-Os-009/85, PETROBRÁS (Depex-Cenpes), Rio de Janeiro. 195p.*
- Zieg, M. J., & Marsh, B. D. (2002). Crystal size distributions and scaling laws in the quantification of igneous textures. *Journal of Petrology*, 43(1), 85-101.
- Zieg, M. J., & Marsh, B. D. (2012). Multiple reinjections and crystal-mush compaction in the Beacon Sill, McMurdo Dry Valleys, Antarctica. *Journal of Petrology*, 53(12), 2567-2591.
- Zingg, T. (1935). *Beitrag zur schotteranalyse* (Unpublished PhD Thesis, ETH Zurich, Switzerland, 1-140).

## APPENDIX A

Spatial localization of the main stations and the resultant magnetometric measurements.

	X (UTM)	Y (UTM)	Z (m)	nT		X (UTM)	Y (UTM)	Z (m)	nT
1	256833.00	7499982.00	577.00	22998.68	66	259010.00	7498489.00	582.00	22900.27
2	256832.00	7499982.00	577.00	23011.33	67	258959.00	7498462.00	579.00	22989.50
3	256832.00	7499982.00	577.00	23006.58	68	258929.00	7498449.00	580.00	22957.87
4	256833.00	7499981.00	578.00	23008.29	69	257856.00	7497643.00	546.00	23165.41
5	256832.00	7499981.00	578.00	23005.51	70	257858.00	7497643.00	548.00	23160.48
6	256832.00	7499981.00	578.00	23019.54	71	257862.00	7497649.00	553.00	23296.20
7	256823.00	7500010.00	585.00	23106.10	72	257898.00	7497678.00	547.00	23149.32
8	256823.00	7500010.00	585.00	23100.70	73	257936.00	7497707.00	542.00	23236.22
9	258605.00	7496885.00	550.00	22753.68	74	257984.00	7497744.00	528.00	23263.26
10	258635.00	7496852.00	554.00	22751.88	75	258028.00	7497782.00	540.00	23236.10
11	258670.00	7496814.00	557.00	22783.27	76	258089.00	7497780.00	538.00	23136.29
12	258720.00	7496774.00	560.00	22846.91	77	258134.00	7497813.00	538.00	23055.25
13	258764.00	7496769.00	561.00	22804.79	78	258158.00	7497858.00	542.00	23061.81
14	258793.00	7496811.00	562.00	22678.98	79	258195.00	7497903.00	543.00	23050.30
15	258825.00	7496859.00	561.00	22872.67	80	258228.00	7497933.00	552.00	23030.40
16	258854.00	7496903.00	561.00	22752.00	81	258271.00	7497964.00	554.00	23018.96
17	258876.00	7496946.00	562.00	22828.63	82	258314.00	7497996.00	556.00	23012.57
18	258890.00	7496992.00	563.00	22804.40	83	258359.00	7498028.00	556.00	22991.99
19	258900.00	7497043.00	565.00	22765.30	84	258402.00	7498061.00	559.00	22992.84
20	258932.00	7497086.00	565.00	22787.33	85	258443.00	7498094.00	559.00	23002.05
21	258978.00	7497117.00	568.00	22837.14	86	258483.00	7498124.00	560.00	23009.90
22	259027.00	7497133.00	569.00	22902.73	87	258520.00	7498154.00	561.00	22942.88
23	259078.00	7497149.00	568.00	22882.27	88	258519.00	7498185.00	561.00	23018.51
24	259135.00	7497177.00	568.00	22892.98	89	258516.00	7498234.00	559.00	23021.91
25	259182.00	7497198.00	568.00	22902.38	90	257837.00	7497626.00	551.00	23197.70
26	259227.00	7497221.00	569.00	22938.82	91	257784.00	7497654.00	544.00	22950.41
27	259255.00	7497264.00	570.00	23043.17	92	257660.00	7497720.00	542.00	24375.85
28	259264.00	7497322.00	572.00	22959.89	93	257620.00	7497744.00	543.00	23583.17
29	259284.00	7497378.00	573.00	22963.23	94	257568.00	7497776.00	542.00	23552.37
30	259323.00	7497418.00	573.00	22844.83	95	257527.00	7497798.00	543.00	23562.46
31	259363.00	7497460.00	573.00	22967.89	96	257485.00	7497823.00	544.00	23535.52
32	259399.00	7497501.00	573.00	22974.51	97	257445.00	7497853.00	544.00	23393.59
33	259437.00	7497541.00	573.00	22997.92	98	257404.00	7497887.00	545.00	23410.01
34	259472.00	7497577.00	574.00	22949.35	99	257368.00	7497925.00	546.00	23352.71
35	259510.00	7497613.00	576.00	22941.30	100	257337.00	7497966.00	545.00	23274.93
36	259543.00	7497646.00	581.00	23247.04	101	257309.00	7498006.00	545.00	23246.62
37	259578.00	7497678.00	586.00	22994.37	102	257292.00	7498042.00	543.00	23159.15
38	259612.00	7497703.00	592.00	22898.92	103	257275.00	7498075.00	545.00	23197.25
39	259643.00	7497739.00	594.00	22971.71	104	257260.00	7498117.00	548.00	23121.38
40	259653.00	7497799.00	595.00	23006.36	105	257247.00	7498158.00	550.00	23178.71
41	259656.00	7497854.00	595.00	23008.48	106	257230.00	7498201.00	552.00	23111.50
42	259655.00	7497910.00	597.00	23042.56	107	257214.00	7498242.00	553.00	23110.01
43	259638.00	7497955.00	599.00	23008.32	108	257197.00	7498288.00	553.00	23190.54
44	259618.00	7497998.00	597.00	22951.76	109	257177.00	7498333.00	554.00	22982.04
45	259573.00	7498055.00	599.00	22960.28	110	257159.00	7498383.00	556.00	22729.16
46	259577.00	7498107.00	599.00	23012.06	111	257144.00	7498439.00	553.00	22997.68
47	259578.00	7498156.00	601.00	22992.01	112	257129.00	7498483.00	553.00	23051.34
48	259569.00	7498212.00	606.00	22949.60	113	257111.00	7498528.00	552.00	22988.91
49	259561.00	7498265.00	609.00	22977.05	114	257091.00	7498569.00	552.00	22914.59
50	259527.00	7498310.00	609.00	23075.04	115	257073.00	7498617.00	552.00	23047.29
51	259481.00	7498337.00	607.00	23001.70	116	257058.00	7498663.00	550.00	23006.71
52	259453.00	7498355.00	607.00	22952.73	117	257040.00	7498707.00	558.00	22971.82
53	259405.00	7498384.00	609.00	23029.66	118	257017.00	7498756.00	563.00	23017.77
54	259355.00	7498414.00	607.00	23057.38	119	257003.00	7498798.00	565.00	22976.18
55	259311.00	7498458.00	606.00	22978.16	120	256987.00	7498845.00	569.00	22943.32
56	259280.00	7498527.00	605.00	23004.81	121	256973.00	7498895.00	562.00	22778.92
57	259276.00	7498582.00	605.00	23005.12	122	256954.00	7498937.00	565.00	22950.21
58	259274.00	7498637.00	605.00	22957.68	123	256934.00	7498982.00	569.00	22946.51
59	259273.00	7498690.00	606.00	22972.57	124	256919.00	7499028.00	569.00	22942.71
60	259237.00	7498677.00	603.00	22976.72	125	256903.00	7499074.00	570.00	22925.13
61	259200.00	7498655.00	599.00	22981.81	126	256885.00	7499118.00	569.00	23231.77
62	259155.00	7498629.00	594.00	22983.61	127	256863.00	7499181.00	567.00	22937.49
63	259110.00	7498597.00	590.00	22984.20	128	256843.00	7499228.00	566.00	22913.44
64	259068.00	7498569.00	589.00	22986.62	129	256829.00	7499276.00	568.00	22891.90
65	259028.00	7498540.00	585.00	22994.51	130	256913.00	7499109.00	573.00	22822.55

## Appendix A - Continuation

	X (UTM)	Y (UTM)	Z (m)	nT		X (UTM)	Y (UTM)	Z (m)	nT
131	256958.00	7499120.00	573.00	22872.27	196	259004.00	7499306.00	605.00	22333.50
132	257006.00	7499106.00	572.00	23072.50	197	259029.00	7499250.00	605.00	22934.56
133	257054.00	7499093.00	571.00	22884.62	198	259051.00	7499199.00	604.00	22929.08
134	257102.00	7499079.00	566.00	22937.41	199	259077.00	7499142.00	604.00	22952.83
135	257148.00	7499065.00	562.00	23010.34	200	259101.00	7499089.00	604.00	22958.59
136	257196.00	7499036.00	557.00	22020.71	201	259128.00	7499031.00	598.00	22964.01
137	257242.00	7499016.00	549.00	22837.30	202	259152.00	7498977.00	602.00	22974.54
138	257302.00	7499026.00	544.00	22953.75	203	259174.00	7498930.00	601.00	22987.72
139	257350.00	7499062.00	542.00	22972.88	204	259193.00	7498879.00	601.00	23036.45
140	257395.00	7499084.00	545.00	23000.18	205	259215.00	7498832.00	607.00	22996.13
141	257446.00	7499094.00	550.00	22988.81	206	259237.00	7498789.00	607.00	22992.54
142	257483.00	7499105.00	554.00	23009.45	207	259260.00	7498741.00	604.00	23010.01
143	257539.00	7499116.00	560.00	23015.06	208	259269.00	7498706.00	603.00	23016.31
144	257576.00	7499076.00	559.00	22977.02	209	258895.00	7498369.00	574.00	22987.50
145	257609.00	7499033.00	552.00	23015.41	210	258868.00	7498323.00	574.00	23014.54
146	257642.00	7498989.00	547.00	22990.92	211	258832.00	7498290.00	573.00	23015.36
147	257667.00	7498949.00	549.00	23012.92	212	258796.00	7498270.00	572.00	23013.89
148	257699.00	7498915.00	555.00	22909.79	213	258758.00	7498246.00	571.00	23013.69
149	257731.00	7498871.00	561.00	21837.78	214	258718.00	7498225.00	570.00	23014.21
150	257752.00	7498837.00	563.00	23095.56	215	258688.00	7498186.00	568.00	23014.96
151	257775.00	7498809.00	570.00	22924.37	216	257563.00	7497615.00	561.00	23075.63
152	257406.00	7499096.00	537.00	23044.40	217	257566.00	7497615.00	565.00	23081.58
153	257427.00	7499141.00	543.00	22929.42	218	257565.00	7497615.00	562.00	23076.91
154	257447.00	7499188.00	545.00	22956.52	219	257766.00	7497595.00	558.00	22990.84
155	257454.00	7499242.00	547.00	22856.78	220	257814.00	7497584.00	556.00	23202.03
156	257456.00	7499290.00	547.00	22927.80	221	257817.00	7497587.00	554.00	23213.90
157	257456.00	7499346.00	547.00	22878.48	222	257865.00	7497559.00	555.00	23258.63
158	257456.00	7499404.00	563.00	23198.99	223	257923.00	7497524.00	556.00	23417.44
159	257463.00	7499453.00	556.00	22735.69	224	257969.00	7497487.00	556.00	23581.12
160	257469.00	7499502.00	558.00	22972.54	225	258009.00	7497457.00	556.00	23562.90
161	257478.00	7499550.00	555.00	22923.39	226	258047.00	7497424.00	556.00	23535.09
162	257485.00	7499598.00	557.00	22940.57	227	258084.00	7497387.00	555.00	23420.99
163	257497.00	7499658.00	555.00	23048.33	228	258121.00	7497348.00	553.00	23378.66
164	257505.00	7499712.00	549.00	22975.75	229	258148.00	7497316.00	553.00	23677.82
165	257531.00	7499739.00	550.00	22932.41	230	258180.00	7497282.00	551.00	25259.22
166	257584.00	7499728.00	552.00	22911.10	231	258164.00	7497299.00	552.00	24135.79
167	257635.00	7499718.00	554.00	23014.34	232	258216.00	7497240.00	550.00	24341.91
168	257681.00	7499704.00	554.00	23027.40	233	258244.00	7497212.00	546.00	21985.82
169	257731.00	7499690.00	555.00	22912.83	234	258250.00	7497160.00	541.00	21809.18
170	257775.00	7499679.00	557.00	22946.83	235	258325.00	7497113.00	537.00	22349.47
171	257827.00	7499667.00	558.00	22934.74	236	258368.00	7497074.00	535.00	21765.18
172	257871.00	7499650.00	560.00	23013.65	237	258402.00	7497037.00	536.00	22433.83
173	257924.00	7499629.00	563.00	22911.80	238	258437.00	7496995.00	536.00	22509.85
174	257974.00	7499608.00	567.00	23027.91	239	258474.00	7496954.00	538.00	22645.69
175	258020.00	7499587.00	571.00	22966.32	240	258508.00	7496914.00	541.00	22653.88
176	258073.00	7499561.00	577.00	22973.23	241	258544.00	7496876.00	543.00	22637.87
177	258120.00	7499542.00	582.00	22977.55	242	258581.00	7496836.00	545.00	22728.10
178	258177.00	7499518.00	586.00	22979.02	243	258616.00	7496797.00	547.00	22716.43
179	258231.00	7499498.00	587.00	23006.42	244	258649.00	7496760.00	548.00	22752.55
180	258281.00	7499486.00	584.00	22934.79	245	258684.00	7496726.00	549.00	22843.19
181	258329.00	7499474.00	584.00	22956.30	246	258719.00	7496691.00	548.00	22864.08
182	258381.00	7499463.00	583.00	22970.51	247	258755.00	7496652.00	547.00	22886.32
183	258437.00	7499457.00	584.00	23016.62	248	258792.00	7496610.00	545.00	22906.17
184	258490.00	7499450.00	586.00	23181.78	249	258825.00	7496567.00	544.00	22842.74
185	258536.00	7499447.00	588.00	22885.11	250	258868.00	7496522.00	541.00	22723.54
186	258584.00	7499444.00	593.00	22872.72	251	258905.00	7496487.00	539.00	24821.29
187	258638.00	7499443.00	600.00	22967.34	252	258939.00	7496443.00	538.00	22971.21
188	258692.00	7499452.00	600.00	22813.99	253	258975.00	7496399.00	539.00	22942.87
189	258756.00	7499467.00	601.00	22929.23	254	259009.00	7496359.00	540.00	22947.96
191	258856.00	7499479.00	602.00	23074.87	255	259046.00	7496319.00	543.00	22939.90
192	258902.00	7499459.00	603.00	22941.57	256	259082.00	7496278.00	546.00	22920.57
193	258942.00	7499437.00	606.00	22922.79	257	259113.00	7496239.00	549.00	22940.57
194	258964.00	7499421.00	607.00	22907.24	258	259148.00	7496199.00	553.00	22716.63
195	258979.00	7499365.00	608.00	22919.45	259	259185.00	7496163.00	555.00	22805.66

## Appendix A - Continuation

	X (UTM)	Y (UTM)	Z (m)	nT		X (UTM)	Y (UTM)	Z (m)	nT
<b>260</b>	259223.00	7496121.00	559.00	22809.86	<b>324</b>	256570.00	7497926.00	527.00	23030.63
<b>261</b>	259288.00	7496051.00	564.00	22892.06	<b>325</b>	256550.00	7497955.00	527.00	23003.48
<b>262</b>	259320.00	7496015.00	567.00	22959.33	<b>326</b>	256512.00	7497984.00	527.00	23077.11
<b>263</b>	259355.00	7495977.00	570.00	22990.36	<b>327</b>	256611.00	7497940.00	527.00	23027.26
<b>264</b>	259396.00	7495930.00	574.00	22929.51	<b>328</b>	256664.00	7497917.00	532.00	23050.54
<b>265</b>	259434.00	7495889.00	577.00	22958.15	<b>329</b>	256708.00	7497877.00	535.00	23092.78
<b>266</b>	259469.00	7495850.00	579.00	22916.38	<b>330</b>	256757.00	7497875.00	540.00	23087.20
<b>267</b>	259505.00	7495808.00	581.00	22925.77	<b>331</b>	256797.00	7497924.00	548.00	23054.90
<b>268</b>	259541.00	7495768.00	583.00	22976.91	<b>332</b>	256791.00	7497973.00	550.00	23027.18
<b>269</b>	259576.00	7495729.00	584.00	22833.29	<b>333</b>	256783.00	7498025.00	552.00	22986.65
<b>270</b>	259605.00	7495689.00	585.00	23021.71	<b>334</b>	256821.00	7498056.00	554.00	23022.70
<b>271</b>	256422.00	7496924.00	532.00	22891.82	<b>335</b>	256876.00	7498063.00	559.00	23225.63
<b>272</b>	256474.00	7496907.00	538.00	22376.75	<b>336</b>	256941.00	7498075.00	563.00	23015.84
<b>273</b>	256522.00	7496896.00	556.00	23113.57	<b>337</b>	256998.00	7498085.00	564.00	23013.44
<b>274</b>	256658.00	7496965.00	547.00	22914.09	<b>338</b>	257082.00	7498100.00	559.00	23094.67
<b>275</b>	256867.00	7496931.00	544.00	22767.54	<b>339</b>	256425.00	7498841.00	557.00	22897.04
<b>276</b>	256937.00	7496911.00	547.00	21655.47	<b>340</b>	256446.00	7498890.00	560.00	22900.55
<b>277</b>	257009.00	7496882.00	540.00	22581.55	<b>341</b>	256461.00	7498936.00	565.00	22918.69
<b>278</b>	257058.00	7496871.00	543.00	22617.33	<b>342</b>	256534.00	7498924.00	570.00	22860.47
<b>279</b>	257146.00	7496851.00	538.00	22671.89	<b>343</b>	256593.00	7498900.00	572.00	22948.31
<b>280</b>	257204.00	7496827.00	545.00	22734.09	<b>344</b>	256650.00	7498857.00	578.00	22968.14
<b>281</b>	256985.00	7496646.00	555.00	22730.46	<b>345</b>	256704.00	7498821.00	580.00	22834.21
<b>282</b>	256929.00	7496613.00	554.00	22774.77	<b>346</b>	256746.00	7498795.00	572.00	22926.99
<b>283</b>	256876.00	7496577.00	563.00	22748.24	<b>347</b>	256745.00	7498744.00	567.00	22923.60
<b>284</b>	256802.00	7496535.00	560.00	22773.24	<b>348</b>	256746.00	7498691.00	566.00	22932.07
<b>285</b>	256740.00	7496497.00	559.00	22799.19	<b>349</b>	256785.00	7498685.00	566.00	22936.73
<b>286</b>	256685.00	7496459.00	563.00	22814.63	<b>350</b>	257133.00	7497901.00	558.00	23234.26
<b>287</b>	256664.00	7496412.00	566.00	22860.62	<b>351</b>	257121.00	7497909.00	555.00	23223.25
<b>288</b>	256688.00	7496338.00	571.00	22859.69	<b>352</b>	257121.00	7497907.00	554.00	23227.62
<b>289</b>	257434.00	7496534.00	528.00	23442.75	<b>353</b>	257108.00	7497865.00	557.00	23215.84
<b>290</b>	257448.00	7496457.00	528.00	23919.98	<b>354</b>	257107.00	7497865.00	557.00	23216.36
<b>291</b>	257435.00	7496391.00	528.00	23335.12	<b>355</b>	257084.00	7497803.00	556.00	23240.88
<b>292</b>	257396.00	7496327.00	533.00	22681.31	<b>356</b>	257059.00	7497774.00	558.00	23407.11
<b>293</b>	257343.00	7496281.00	529.00	22584.92	<b>357</b>	257043.00	7497717.00	558.00	23409.31
<b>294</b>	257295.00	7496243.00	528.00	22630.94	<b>358</b>	257008.00	7497702.00	557.00	23353.94
<b>295</b>	257266.00	7496188.00	530.00	22611.06	<b>359</b>	256969.00	7497721.00	554.00	23304.67
<b>296</b>	257227.00	7496131.00	532.00	22583.24	<b>360</b>	256934.00	7497747.00	554.00	23264.51
<b>297</b>	257170.00	7496136.00	537.00	22624.36	<b>361</b>	257011.00	7497670.00	559.00	23384.91
<b>298</b>	257101.00	7496168.00	532.00	22645.55	<b>362</b>	257013.00	7497612.00	555.00	23491.19
<b>299</b>	257065.00	7496229.00	553.00	22826.27	<b>363</b>	257021.00	7497546.00	552.00	23682.66
<b>300</b>	257089.00	7496294.00	554.00	22856.40	<b>364</b>	257006.00	7497518.00	550.00	23956.16
<b>301</b>	257101.00	7496361.00	560.00	22885.60	<b>365</b>	256976.00	7497513.00	549.00	23947.07
<b>302</b>	257112.00	7496423.00	556.00	22883.85	<b>366</b>	256946.00	7497513.00	545.00	23943.93
<b>303</b>	257058.00	7496393.00	556.00	22894.98	<b>367</b>	256906.00	7497509.00	539.00	24049.87
<b>304</b>	257004.00	7496354.00	563.00	22886.04	<b>368</b>	256877.00	7497502.00	537.00	24158.97
<b>305</b>	256941.00	7496314.00	561.00	22897.66	<b>369</b>	256849.00	7497510.00	538.00	24086.70
<b>306</b>	256878.00	7496275.00	563.00	22854.57	<b>370</b>	256940.00	7497501.00	542.00	24042.95
<b>307</b>	256801.00	7496227.00	567.00	22802.90	<b>371</b>	257020.00	7497501.00	554.00	24030.63
<b>308</b>	256745.00	7496199.00	576.00	22770.14	<b>372</b>	257048.00	7497440.00	547.00	25032.11
<b>309</b>	256717.00	7496265.00	573.00	22807.85	<b>373</b>	257102.00	7497414.00	549.00	24640.61
<b>310</b>	256690.00	7496333.00	568.00	22854.65	<b>374</b>	257202.00	7497348.00	535.00	23153.28
<b>311</b>	256669.00	7496397.00	564.00	22851.55	<b>375</b>	257202.00	7497306.00	530.00	22539.20
<b>312</b>	256603.00	7496466.00	560.00	22847.99	<b>376</b>	257171.00	7497263.00	525.00	21920.62
<b>313</b>	256581.00	7496516.00	558.00	22675.18	<b>377</b>	257112.00	7497204.00	523.00	21110.05
<b>314</b>	256560.00	7496564.00	557.00	22583.41	<b>378</b>	257061.00	7497160.00	522.00	23085.26
<b>315</b>	256538.00	7496613.00	553.00	22439.86	<b>379</b>	257077.00	7497168.00	516.00	20774.73
<b>316</b>	256783.00	7497540.00	548.00	23887.79	<b>380</b>	257074.00	7497169.00	515.00	21398.45
<b>317</b>	256730.00	7497568.00	536.00	23771.77	<b>381</b>	257039.00	7497153.00	518.00	23530.44
<b>318</b>	256697.00	7497610.00	535.00	23574.99	<b>382</b>	256988.00	7497124.00	509.00	23358.97
<b>319</b>	256678.00	7497667.00	531.00	23385.35	<b>383</b>	256945.00	7497111.00	508.00	22633.34
<b>320</b>	256641.00	7497714.00	529.00	23321.03	<b>384</b>	256911.00	7497125.00	498.00	23346.90
<b>321</b>	256637.00	7497775.00	528.00	23195.99	<b>385</b>	256902.00	7497170.00	508.00	22784.14
<b>322</b>	256621.00	7497832.00	530.00	23133.47	<b>386</b>	256886.00	7497222.00	507.00	23043.43
<b>323</b>	256599.00	7497889.00	527.00	23071.60	<b>387</b>	256876.00	7497258.00	507.00	21892.47

## Appendix A - Continuation

	X (UTM)	Y (UTM)	Z (m)	nT		X (UTM)	Y (UTM)	Z (m)	nT
<b>388</b>	256891.00	7497275.00	507.00	21845.29	<b>452</b>	256679.00	7497146.00	548.00	23149.57
<b>389</b>	256895.00	7497315.00	500.00	21799.01	<b>453</b>	256698.00	7497127.00	538.00	23146.47
<b>390</b>	256890.00	7497357.00	492.00	22091.32	<b>454</b>	256964.00	7495637.00	559.00	23015.82
<b>391</b>	256878.00	7497391.00	489.00	22809.82	<b>455</b>	257006.00	7495613.00	560.00	22977.15
<b>392</b>	256893.00	7497423.00	495.00	24065.53	<b>456</b>	257000.00	7495578.00	558.00	23023.79
<b>393</b>	256859.00	7497408.00	506.00	24787.73	<b>457</b>	257013.00	7495545.00	561.00	23013.47
<b>394</b>	256943.00	7497410.00	492.00	22835.28	<b>458</b>	258775.00	7493373.00	547.00	22509.47
<b>395</b>	257035.00	7497374.00	484.00	21158.71	<b>459</b>	258744.00	7493411.00	545.00	22500.10
<b>396</b>	257061.00	7497304.00	470.00	21535.00	<b>460</b>	258706.00	7493458.00	543.00	22553.05
<b>397</b>	257060.00	7497235.00	446.00	21495.91	<b>461</b>	258671.00	7493503.00	540.00	22648.57
<b>398</b>	257037.00	7497145.00	289.00	21942.77	<b>462</b>	258635.00	7493550.00	537.00	22751.04
<b>399</b>	256939.00	7497168.00	450.00	22472.04	<b>463</b>	258600.00	7493595.00	532.00	22784.26
<b>400</b>	256944.00	7497177.00	487.00	21482.55	<b>464</b>	258563.00	7493643.00	528.00	22765.92
<b>401</b>	257246.00	7496800.00	554.00	22787.72	<b>465</b>	258528.00	7493688.00	524.00	22734.78
<b>402</b>	257232.00	7496807.00	549.00	22772.08	<b>466</b>	258492.00	7493733.00	518.00	22654.28
<b>403</b>	257216.00	7496802.00	543.00	22768.89	<b>467</b>	258455.00	7493778.00	514.00	22508.82
<b>404</b>	257203.00	7496792.00	544.00	22769.14	<b>468</b>	258420.00	7493820.00	513.00	22530.86
<b>405</b>	257186.00	7496783.00	545.00	22770.78	<b>469</b>	258398.00	7493890.00	514.00	23012.53
<b>406</b>	257166.00	7496769.00	547.00	22780.66	<b>470</b>	258392.00	7493951.00	521.00	22860.16
<b>407</b>	257147.00	7496757.00	546.00	22780.94	<b>471</b>	258386.00	7494011.00	525.00	22526.90
<b>408</b>	257127.00	7496743.00	547.00	22767.20	<b>472</b>	258380.00	7494073.00	526.00	22269.79
<b>409</b>	257107.00	7496731.00	548.00	22757.69	<b>473</b>	258375.00	7494133.00	529.00	22505.10
<b>410</b>	257085.00	7496719.00	557.00	22747.57	<b>474</b>	258370.00	7494194.00	533.00	23759.15
<b>411</b>	257067.00	7496699.00	554.00	22752.16	<b>475</b>	258364.00	7494253.00	537.00	25799.62
<b>412</b>	257036.00	7496682.00	556.00	22748.40	<b>476</b>	258360.00	7494314.00	540.00	24257.82
<b>413</b>	256998.00	7496653.00	553.00	22747.02	<b>477</b>	258375.00	7494372.00	543.00	23317.67
<b>414</b>	256970.00	7496635.00	555.00	22750.63	<b>478</b>	258403.00	7494426.00	546.00	23114.72
<b>415</b>	256944.00	7496618.00	555.00	22763.63	<b>479</b>	258437.00	7494475.00	549.00	23202.35
<b>416</b>	256920.00	7496604.00	556.00	22784.63	<b>480</b>	258486.00	7494509.00	553.00	23297.71
<b>417</b>	256895.00	7496586.00	551.00	22773.32	<b>481</b>	258478.00	7494571.00	551.00	23465.29
<b>418</b>	256874.00	7496571.00	551.00	22769.30	<b>482</b>	258477.00	7494628.00	552.00	23244.00
<b>419</b>	256853.00	7496559.00	554.00	22777.04	<b>483</b>	258481.00	7494687.00	553.00	23088.17
<b>420</b>	256830.00	7496555.00	554.00	22732.48	<b>484</b>	258493.00	7494745.00	554.00	23068.43
<b>421</b>	257408.00	7496586.00	532.00	23140.73	<b>485</b>	258508.00	7494800.00	553.00	23029.44
<b>422</b>	257396.00	7496610.00	534.00	23099.24	<b>486</b>	258527.00	7494858.00	553.00	23001.21
<b>423</b>	257384.00	7496632.00	537.00	23013.59	<b>487</b>	258556.00	7494912.00	553.00	22980.55
<b>424</b>	257375.00	7496661.00	537.00	23071.50	<b>488</b>	258614.00	7494906.00	557.00	22975.07
<b>425</b>	257360.00	7496679.00	543.00	23019.02	<b>489</b>	258672.00	7494899.00	560.00	22970.58
<b>426</b>	257347.00	7496700.00	545.00	22963.73	<b>490</b>	258729.00	7494891.00	562.00	22965.73
<b>427</b>	257330.00	7496724.00	546.00	22894.68	<b>491</b>	258793.00	7494884.00	565.00	23000.55
<b>428</b>	257315.00	7496748.00	546.00	22862.22	<b>492</b>	258852.00	7494877.00	567.00	22932.71
<b>429</b>	257288.00	7496776.00	539.00	22879.82	<b>493</b>	258488.00	7494924.00	549.00	22979.04
<b>430</b>	257270.00	7496794.00	542.00	22790.17	<b>494</b>	258427.00	7494928.00	544.00	22972.61
<b>431</b>	257245.00	7496806.00	544.00	22754.94	<b>495</b>	258369.00	7494935.00	539.00	22981.63
<b>432</b>	257218.00	7496813.00	536.00	22726.44	<b>496</b>	258310.00	7494943.00	533.00	22992.86
<b>433</b>	257198.00	7496829.00	538.00	22717.96	<b>497</b>	258375.00	7494878.00	543.00	22991.88
<b>434</b>	257169.00	7496839.00	532.00	22633.60	<b>498</b>	258361.00	7494832.00	542.00	23009.39
<b>435</b>	257145.00	7496849.00	531.00	22686.02	<b>499</b>	259073.00	7495195.00	556.00	22941.04
<b>436</b>	257118.00	7496860.00	532.00	22713.47	<b>500</b>	259078.00	7495251.00	547.00	22940.34
<b>437</b>	257089.00	7496868.00	535.00	22644.06	<b>501</b>	259084.00	7495293.00	543.00	22939.66
<b>438</b>	257063.00	7496873.00	536.00	22617.14	<b>502</b>	259057.00	7495163.00	557.00	22922.43
<b>439</b>	257041.00	7496865.00	544.00	22662.03	<b>503</b>	258997.00	7495169.00	557.00	22936.71
<b>440</b>	256738.00	7496968.00	531.00	23357.19	<b>504</b>	259068.00	7495121.00	562.00	22932.95
<b>441</b>	256747.00	7496988.00	537.00	23131.56	<b>505</b>	259061.00	7495069.00	565.00	22929.39
<b>442</b>	256759.00	7497015.00	534.00	22632.33	<b>506</b>	259055.00	7495012.00	568.00	22929.11
<b>443</b>	256771.00	7497041.00	532.00	22777.57	<b>507</b>	259047.00	7494946.00	572.00	22927.74
<b>444</b>	256777.00	7497069.00	530.00	22766.29	<b>508</b>	259041.00	7494870.00	577.00	22933.16
<b>445</b>	256776.00	7497096.00	527.00	22870.81	<b>509</b>	256284.00	7497378.00	573.00	22926.86
<b>446</b>	256769.00	7497121.00	526.00	23024.38	<b>510</b>	256272.00	7497412.00	576.00	22937.13
<b>447</b>	256759.00	7497148.00	525.00	23174.50	<b>511</b>	256257.00	7497443.00	577.00	22929.79
<b>448</b>	256750.00	7497171.00	525.00	23306.49	<b>512</b>	256242.00	7497486.00	559.00	22921.47
<b>449</b>	256739.00	7497194.00	527.00	23360.94	<b>513</b>	256218.00	7497552.00	575.00	22916.35
<b>450</b>	256704.00	7497165.00	522.00	23182.09	<b>514</b>	256197.00	7497609.00	581.00	22926.19
<b>451</b>	256682.00	7497159.00	511.00	23104.33	<b>515</b>	256178.00	7497667.00	574.00	22909.03
					<b>516</b>	256154.00	7497714.00	579.00	22928.88

## APPENDIX B

List of analyzed samples and the main applied analysis.

AVAILABLE SAMPLES AND ANALYSIS						
Sample	X (UTM)	Y(UTM)	Z*(m)	Facies	Rock-type	Analysis*
IC-01	256978.66	7497227.96	97	Jaguar-skin	Qz-Monzd.	1, 2, 3, 4, 6
IC-01b	256938.13	7497271.39	97	Jaguar-skin	Qz-Monzd.	1, 3, 4
IC-02a	256933.08	7497362.28	96	Massive	Qz-Diorite	1, 3, 4
IC-02b	256968.44	7497358.39	95	Massive	Qz-Diorite	
IC-03	257005.55	7497306.55	85	Layered	Qz-Monzd.	1
IC-03b	257020.43	7497270.94	71	Layered	Qz-Monzd.	1
IC-03c	257014.96	7497227.63	63	Layered	Qz-Monzd.	1
IC-04a	256950.01	7497189.19	38	Grid-like	Granodiorite	1, 3, 4, 6
IC-04b	256898.80	7497205.98	47	Grid-like	Granodiorite	1, 3, 5, 6
IC-04c	256887.77	7497254.89	52	Jaguar-skin	Qz-Monzd.	1, 3, 4, 5, 6
IC-05	256913.67	7497399.21	22	Massive	Gabbro	1, 2, 3, 4
IC-06	256986.87	7497183.4	55	Grid-like	Granodiorite	1, 3, 4, 6
IC-06b	257040.63	7497212.89	57	Grid-like	Granodiorite	1, 3, 4
IC-07a	257023.73	7497365.43	20	Massive	Gabbro	1, 2, 3, 4, 5, 6, 7, 8
IC-07b	256987.47	7497394.28	24	Jaguar-skin	Qz-Monzd.	1, 3, 6
IC-08	256935.52	7497412.22	9	Massive	Gabbro	1, 3, 4, 5, 6
IC-08b	256855.82	7497374.52	10	Massive	Gabbro	1, 3
IC-09	256863.21	7497330.23	0.00	Chilled gab.	Gabbro	1, 2, 4
IC-09 40	256863.21	7497330.23	0.40	Massive	Gabbro	1, 2
IC-09 2	256863.21	7497330.23	3	Amygdaloidal	Gabbro	1, 2, 3, 6
IC-09 5	256863.21	7497330.23	11	Ocelli	Gabbro	1, 5
IC-09 7	256863.21	7497330.23	16	Massive	Gabbro	1
IC-09 9	256863.21	7497330.23	17	Massive	Gabbro	1, 2, 3, 4, 6
Lim-02	256943.11	7497209.24	110	Foliated	Qz-Monzd.	1, 2, 3, 4, 5, 6, 7, 8
Lim-03	256914.11	7497230.72	18	Massive	Gabbro	1, 2, 4
Lim-04	256990.59	7497332.65	86*	Applitic vein	Rhyolite	1, 4
Lim-06	256853.81	7497404.15	35	Massive	Gabbro	2
Lim-10	257016.64	7497380.34	28	Jaguar-skin	Qz-Monzd.	1, 2, 3, 4, 5, 6
TF-01	256932.15	7497335.57	102	Jaguar-skin	Qz-Monzd.	2
TF-02	256929.88	7497343.96	102	Jaguar-skin	Qz-Monzd.	1, 2, 3
TF-03	256924.60	7497352.52	100	Jaguar-skin	Qz-Monzd.	2
TF-04	256923.57	7497357.51	100	Jaguar-skin	Qz-Monzd.	2
TF-05	256923.50	7497364.97	99	Jaguar-skin	Qz-Monzd.	1, 2, 3, 6
TF-06	256929.24	7497368.55	97	Massive	Qz-Diorite	2
TF-07	256936.76	7497368.98	97	Massive	Qz-Diorite	2
TF-08	256944.48	7497368.60	97	Massive	Qz-Diorite	2
TF-09	256951.07	7497368.46	96	Massive	Qz-Diorite	1, 2, 3
TF-10	256954.63	7497365.00	96	Massive	Qz-Diorite	2
TF-11	256956.17	7497362.71	96	Massive	Qz-Diorite	2
TF-12	256959.96	7497359.24	95	Massive	Qz-Diorite	2
TF-13	256962.83	7497355.34	90	Jaguar-skin	Qz-Monzd.	1, 2, 3
TF-14	256966.13	7497350.30	90	Jaguar-skin	Qz-Monzd.	
TF-15	256971.51	7497346.57	89	Jaguar-skin	Qz-Monzd.	1, 2, 3
TF-16	256972.51	7497342.20	88	Jaguar-skin	Qz-Monzd.	2

\*1 – Petrography, 2 – Magnetic susceptibility measurements, 3 - Modal quantification, 4 – Whole-rock chemistry, 5 – Mineral chemistry, apatite melt-inclusions, ocelli/quenched matrix, 6 – Quantitative Textural analysis, 7 – In situ Isotopic analysis, 8 - In situ Trace elements.

## Appendix B - Continuation

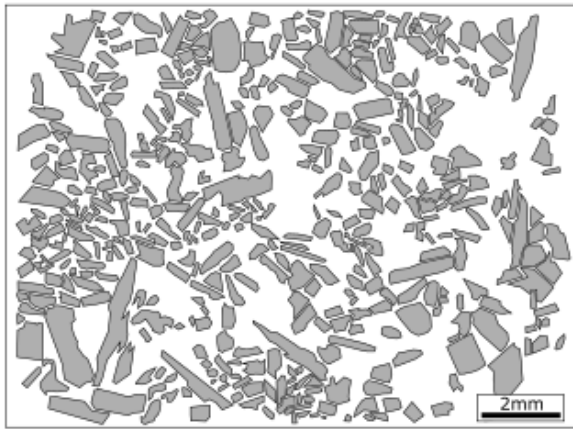
AVAILABLE SAMPLES AND ANALYSIS						
Sample	X (UTM)	Y(UTM)	Z*(m)	Facies	Rock-type	Analysis*
<b>TF-17</b>	256973.55	7497338.18	88	Jaguar-skin	Qz-Monzd.	1, 2, 3, 4, 5, 6
<b>TF-18</b>	256975.22	7497332.52	87	Jaguar-skin	Qz-Monzd.	2
<b>TF-19</b>	256979.18	7497328.87	86	Jaguar-skin	Qz-Monzd.	1, 2, 3, 5
<b>TF-20</b>	256983.00	7497324.00	86	Jaguar-skin	Qz-Monzd.	1, 2, 4
<b>TF-21</b>	256985.73	7497319.30	85	Layered	Qz-Monzd.	2
<b>TF-22</b>	256989.98	7497314.39	84	Layered	Qz-Monzd.	2
<b>TF-23</b>	256993.81	7497309.54	84	Layered	Qz-Monzd.	1, 2, 3
<b>TF-24</b>	256998.91	7497307.46	83	Layered	Qz-Monzd.	1, 4, 6
<b>TF-25</b>	257004.06	7497291.22	81	Layered	Qz-Monzd.	1, 2
<b>TF-26</b>	257013.27	7497273.41	80	Layered	Qz-Monzd.	1, 2
<b>TF-27</b>	257018.20	7497257.97	79	Layered	Qz-Monzd.	2
<b>TF-28</b>	257022.06	7497238.28	77	Layered	Qz-Monzd.	
<b>TF-29</b>	257009.50	7497219.44	76	Layered-like	Granodiorite	1, 4
<b>TF-30</b>	256994.12	7497205.48	74	Layered-like	Granodiorite	1, 2, 3, 6
<b>TF-31</b>	256976.77	7497195.71	73	Layered-like	Granodiorite	2
<b>TF-32</b>	256954.52	7497185.87	72	Layered-like	Granodiorite	1, 2, 3, 4, 5
<b>TF-33</b>	256968.20	7497188.8	69	Layered-like	Granodiorite	2
<b>TF-34</b>	256983.06	7497193.81	67	Layered-like	Granodiorite	1, 2
<b>TF-35</b>	256995.25	7497200.39	66	Grid-like	Granodiorite	2
<b>TF-36</b>	257004.10	7497204.51	65	Grid-like	Granodiorite	1, 2, 3, 4, 6, 7, 8
<b>Dike</b>	256798.61	7497446.56	-	Massive	Gabbro	1, 4, 5
<b>Vein 1</b>	256881.20	7497211.49	65	Applitic vein	Rhyolite	1, 4
<b>Vein 2</b>	256881.20	7497211.49	70	Applitic vein	Rhyolite	4
<b>IGN-1</b>	256874.88	7497348.43	60	-	-	2
<b>IGN-2</b>	256877.00	7497332.98	61	-	-	2
<b>IGN-3</b>	256879.00	7497311.77	62	-	-	2
<b>IGN-4</b>	256879.18	7497293.03	55	-	-	2
<b>IGN-5</b>	256879.52	7497278.13	50	-	-	2
<b>IGN-6</b>	256879.43	7497264.69	45	-	-	2
<b>IGN-7</b>	256877.54	7497254.20	47	-	-	2
<b>IGN-8</b>	256878.76	7497237.34	43	-	-	2

*\*1 – Petrography, 2 – Magnetic susceptibility measurements, 3 - Modal quantification, 4 – Whole-rock chemistry, 5 – Mineral chemistry, apatite melt-inclusions, ocelli/quenched matrix, 6 – Quantitative Textural analysis, 7 – In situ Isotopic analysis, 8 - In situ Trace elements.*

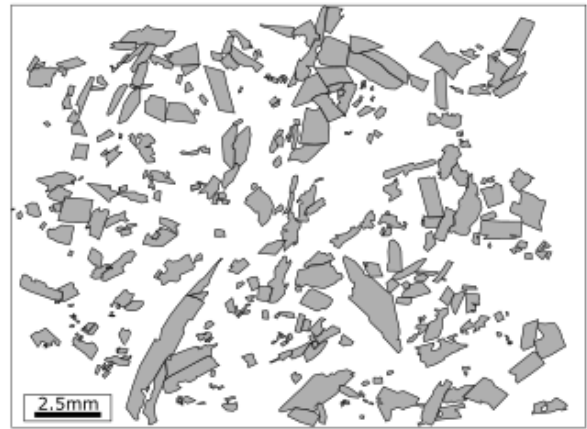
## APPENDIX C

CSD Files depicting the obtained plagioclase crystals contours for each analyzed sample.

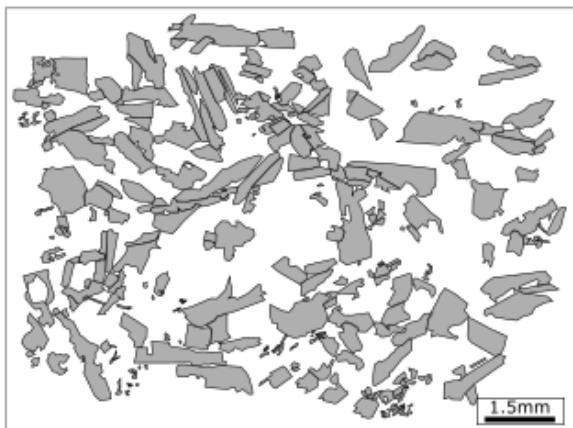
IC-01



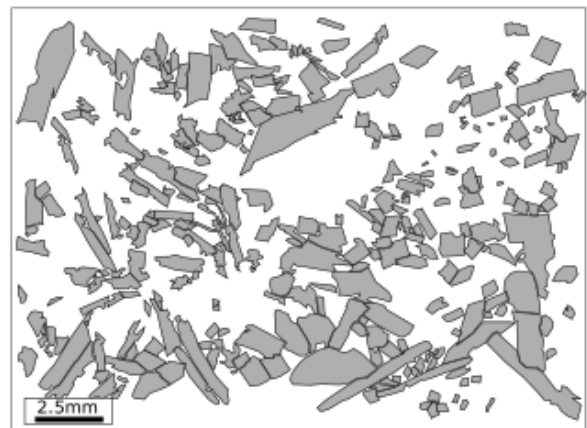
IC-04c



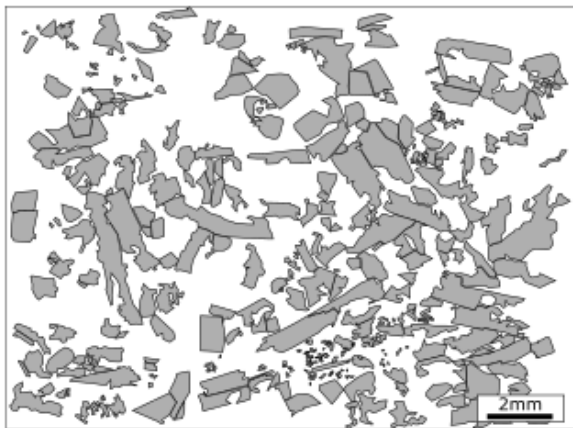
IC-07a



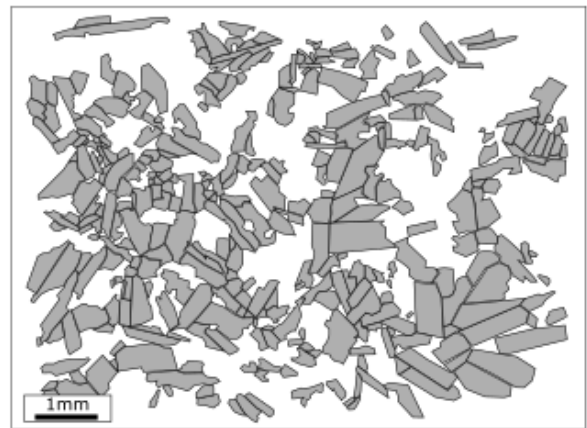
IC-04b



IC-07b

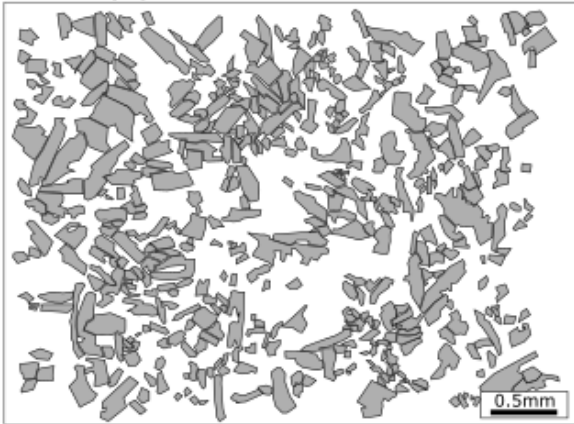


IC-08

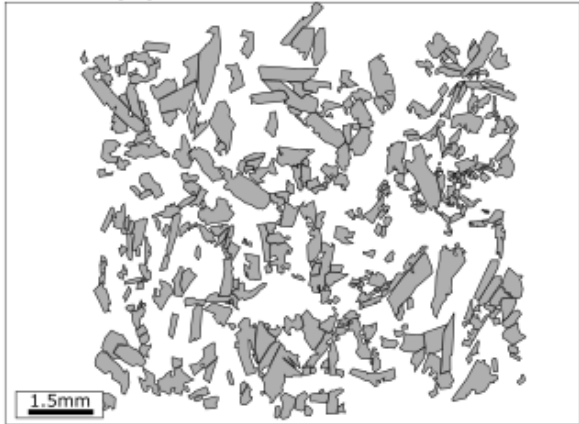


Appendix C - Continuation

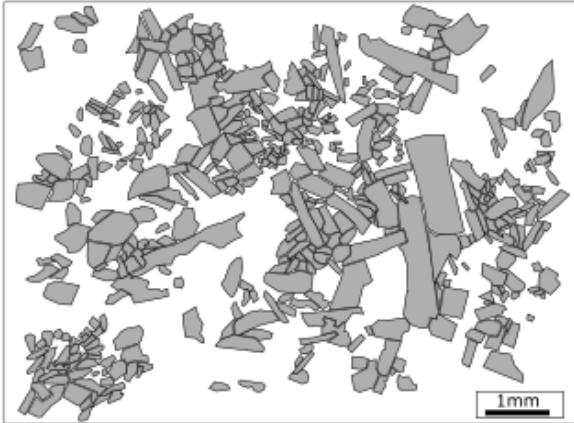
IC-09 (2)



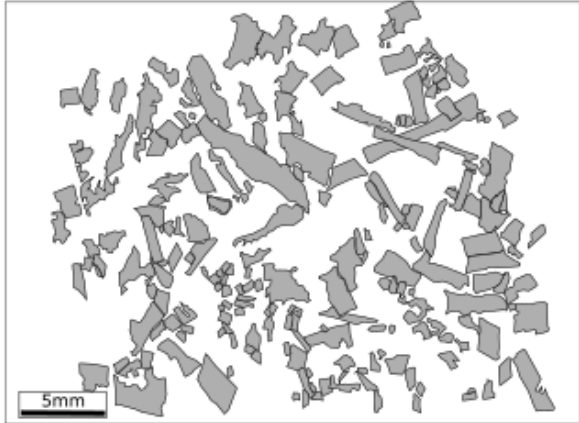
IC-09 (9)



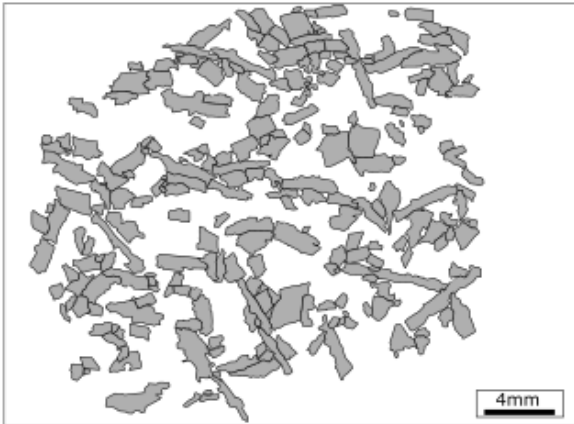
TF-05



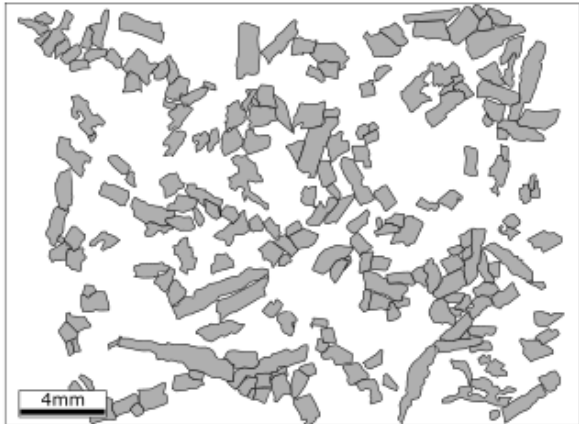
TF-36



TF-17

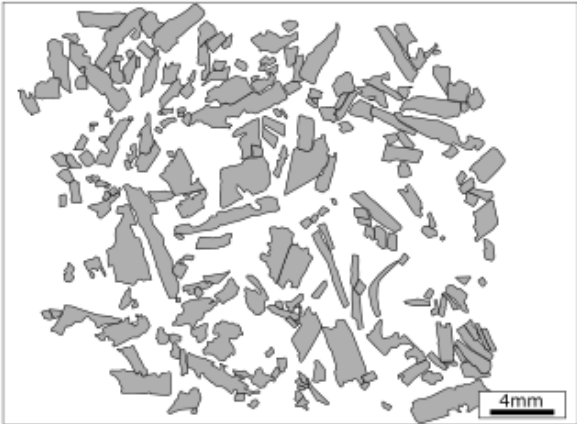


TF-24

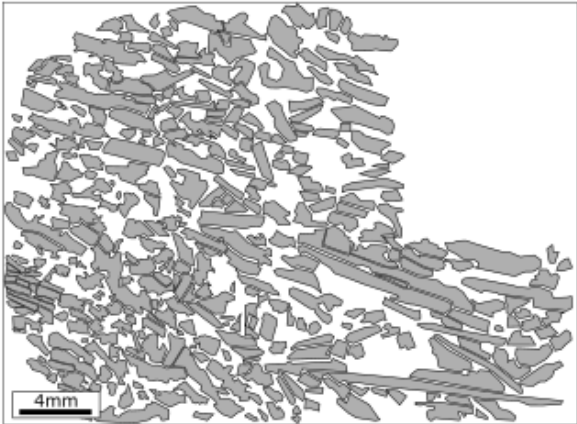


Appendix C - Continuation

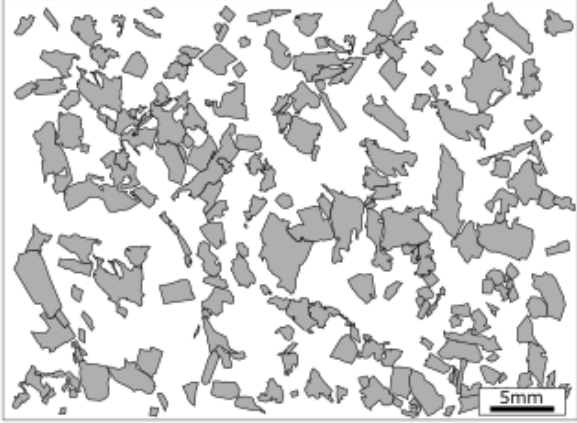
TF-30



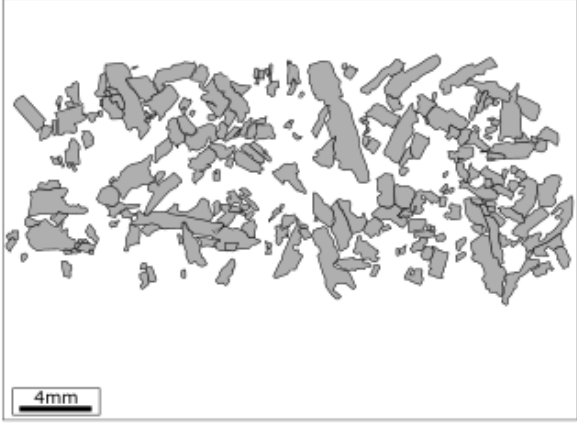
LIM-02



IC-06



LIM-10



IC-04

